Geology of the subduction thrust: insights from exhumed shear zones on Kyushu, SW Japan

Christopher James Tulley

submitted for the degree of

Doctor of Philosophy

at Cardiff University

Wales

28/06/2021

Abstract

Along plate interfaces in subduction zones, displacement occurs by a spectrum of slip styles, including ∼steady creep, slow-slip events, tectonic tremor, and earthquakes. However, the factors which determine where, and how, different slip styles occur, are not clear. In Japan, on Kyushu, three exposures of plate boundary shear zones, exhumed from different metamorphic conditions along a similar paleo-margin, within the temperature range 300-550 °C, represent a natural laboratory to understand processes which influence slip style along the subduction plate interface.

In exposures exhumed from conditions corresponding to localised metamorphic dehydration reactions, foliations and quartz veins are mutually overprinting, indicating episodic brittle behaviour within an otherwise viscous regime. Local fluid pressurisation, and amplified shear stresses along lithological contacts, are inferred to drive embrittlement. A quartz recrystallised grain size piezometer is applied to viscously deformed quartz veins, and used to constrain the level of differential stress within hydrated metabasalt. Results suggest that hydrated oceanic crust is far weaker than dry crust, and weak enough to control plate interface rheology. Microstructural observations of antigorite serpentinite deformed at $\sim$ 500 °C suggest that foliation development results in a reduction in viscosity. Geometric relationships within the shear zone deformed at $\sim$ 500 °C suggest that serpentinite may be more viscous than hydrated oceanic crust and subducted sediment, and therefore plate interface strain may be concentrated in the subducting plate, along the slab-mantle boundary.

Outcrop and microstructural observations suggest that, within the plate boundary shear zone, subducted sediments are slightly weaker than hydrated oceanic crust, and antigorite serpentinite is stronger than both subducted sediments and hydrated oceanic crust. Overall, brittle instabilities occur in all of the deformed lithologies due to a combination of metamorphic dehydration reactions locally reducing effective stresses, and local shear stress amplifications along lithological contacts.

Acknowledgements

Many people have helped with this project, in one way or another. Åke Fagereng took me on as a student, and provided superb advice, encouragement, and constructive criticism throughout. Kohtaro Ujiie hosted me in Tsukuba, introduced me to Japan and Japanese geology, and was also a great source of friendly advice and encouragement. Johann Diener introduced me to the world of phase equilibrium modelling and gave tireless help solving many apparently insurmountable problems. Funding for this project came from the European Research Council Horizon 2020 programme (grant agreement 715836 to Åke Fagereng), whose support is gratefully acknowledged.

To everyone who came on trips to Nobeoka, Nagasaki, and Hokkaido to look at rocks, thanks for help in the field, and for making it such an great experience. Afternoons fishing in rural Hokkaido, long dinners after days in the field, and going on a roller-coaster in Yokohama with Åke, were, among many others, memorable highlights. In Cardiff, Tony Oldroyd and Duncan Muir helped with sample preparation and electron microscope work, and were always around for a chat - thanks guys. Thanks also to all of the other students, post-docs, and staff in Cardiff who I've worked with, in particular Harry, Christian, Sophie, Jack, Adam, Sara and Lucy.

Outside of my own work, I was lucky to travel with Max, Sophie, and Christian on their fieldwork - thanks for having me along, those trips to Oman, Cyprus and the Outer Hebrides were amazing geological and cultural experiences. Outside of work, Eben, Barney, Hermione, Leo, Meg, Matt, to name a few, introduced me to South Wales climbing, and took me on many trips further afield - thanks all. A heartfelt thanks to my partner Sophie, for your support, and belief in me, especially over the final few weeks - it's meant the world. Thanks also to Casper the Corsa, who took us everywhere. Finally, thanks to my family. Visits to Neale and Sarah in Oxford provided welcome breaks from study, and the ever-present support from afar from my Mum, Dad, and sister, has been hugely appreciated.

Contents

List of Figures

Chapter 1

Introduction

Earths' outer layer, the lithosphere, is made up of tectonic plates that shift over the underlying asthenosphere at rates of centimetres per year. Stresses build up where plates with different relative motions meet, and are relieved by slip along plate-boundary shear zones. Subduction zones occur at plate boundaries where relatively dense oceanic lithosphere is pulled (subducted) beneath more buoyant continental or oceanic lithosphere. Along active subduction zones, seismic and geodetic observations indicate that plate boundary slip occurs by a spectrum of slip styles (Gomberg *et al.*, 2016; Ide *et al.*, 2007; Peng and Gomberg, 2010; Schwartz and Rokosky, 2007). In terms of characteristic duration, earthquakes (catastrophic, discontinuous slip at meters per second) and plate-rate creep (benign, continuous sliding at centimetres per year) represent the end-members of this spectrum. As outlined by Huntington and Klepeis (2018), understanding the factors that control the occurrence and distribution of different slip styles would be a major advance in understanding the seismic hazards posed by subduction zones. For example, it is unclear which components of subducting oceanic lithosphere and overriding continent deform within the plate boundary shear zone (e.g., oceanic crust, subducting sediments, continental crust, continental mantle), and what their likely seismic behaviour is. Direct geological observations of exhumed subduction plate boundaries will give constraints on the deformed lithologies, and their likely slip style. Incorporating this knowledge with observations of the input lithologies along active margins should contribute to a better understanding of the likely distribution of slip styles, and associated seismic hazard.

In this thesis I will investigate three exposures of plate boundary shear

zones which were active at ~ 330 °C, ~ 370 °C, and ~ 500 °C; plate boundary temperatures (T) that span the inferred thermally-controlled frictional-viscous transition (e.g., Brace and Kohlstedt, 1980; Hyndman *et al.*, 1997), and where a range of slip behaviours are thought to occur in active subduction zones. The overall aim is to understand the geological processes that influence where, and how different slip styles occur along the subduction plate boundary over this temperature range. In this chapter I will provide a short overview of the research topic, set out the main questions addressed by this study, and give a brief outline of each of the following chapters.

1.1 The subduction thrust

Movement along subduction-type plate boundaries is accommodated by shearing within a gently dipping tabular shear zone that defines the boundary between the subducting and overriding plates (Plafker, 1965; Shreve and Cloos, 1986). The location of the plate boundary along active subduction zones is delineated by the distribution of thrust-sense seismicity, and contrast in physical properties between the subducting slab and the overriding mantle.

The depth range where earthquakes nucleate along the plate boundary is referred to as the seismogenic zone. Down-dip of the seismogenic zone, a zone of transitional slip styles occurs, where slip phenomena including tectonic tremor and slow slip events nucleate (Figs. 1.1, 2.14). Tremor is defined as noisy seismic signals that persist for weeks to months, and is interpreted to contain low frequency earthquakes reflecting small-displacement shear slip along the plate boundary (e.g., Gomberg *et al.*, 2016; Shelly *et al.*, 2006). Slow slip events occur episodically, but slip occurs at a rate too slow to produce detectable seismic waves (e.g., Dragert *et al.*, 2001; Schwartz and Rokosky, 2007). Further down dip from the transitional zone, approximately steady aseismic sliding dominates, and occurs down to a depth of 70-80 km, where the subducting slab becomes kinematically coupled to the convecting mantle (Abers *et al.*, 2020; Wada and Wang, 2009).

The up-dip limit of the seismogenic zone is suggested to be controlled by the location of the $\sim 100-150$ °C isotherm, while the down-dip limit is thought to be controlled by the location of the ~ 350 °C isotherm or the intersection with the mantle wedge corner, whichever is shallower (Hyndman *et al.*, 1997). As

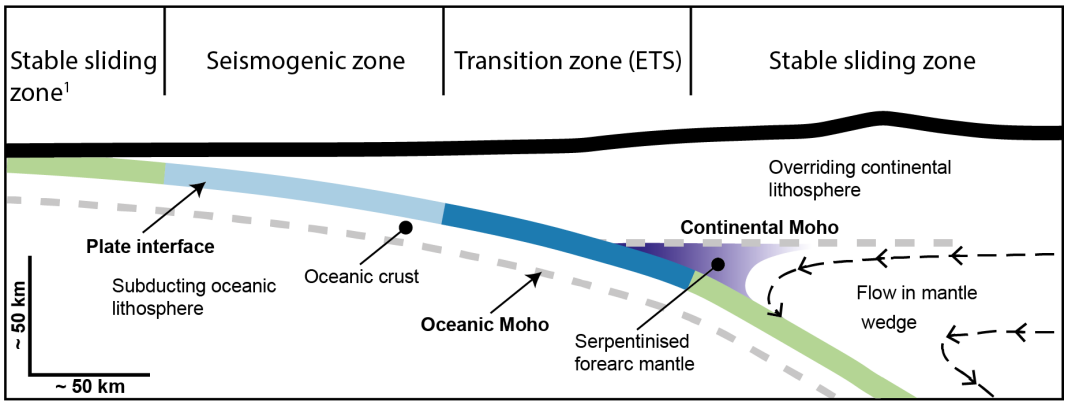

Figure 1.1: Schematic showing the geometry and mechanical behaviour of a subduction plate interface, highlighting the location of the seismogenic zone, transitional zone, and stably-sliding aseismic zone, along the plate boundary (inspired by Audet and Kim, 2016). [1] Updip of the seismogenic zone, aseismic sliding dominates, however along some margins slow slip events occur here (e.g., Hikurangi; Wallace *et al.*, 2016). Large thrust earthquakes may also propagate into this region (e.g., 2011 Tohoku-Oki earthquake; Ide *et al.*, 2011).

the plate boundary dips gently at upper to lower-crustal levels, the subduction plate boundary has a relatively broad thermally-controlled seismogenic zone. As the maximum moment magnitude of earthquakes is limited by the potential rupture area (Eqs. 2.23, 2.24; Aki, 1967; Hanks and Kanamori, 1979), broad seismogenic zones along subduction plate boundaries produce the largest earthquakes on Earth. This is consistent with that $> 85\%$ of global seismic moment release is estimated to relate to plate boundary slip in subduction zones (Pacheco *et al.*, 1993).

While observations of seismicity delineate the position of the plate boundary shear zone, depth constraints are too uncertain to provide information about the thickness of the actively deforming zone. As shear strain rate depends on the width of the actively deforming zone (section 2.2), and viscous deformation mechanisms are sensitive to strain rate (section 2.5), an assessment of the thickness of the deforming zone is critical for evaluating potential deformation mechanisms and likely slip styles. Using observations from drilling expeditions and exhumed plate boundaries, Rowe *et al.* (2013) estimated the thickness of a typical plate boundary shear zone up-dip of the base of the seismogenic zone to be approximately 100-350 m. Teleseismic observations show that a several km thick low seismic velocity layer exists at the top of subducting oceanic lithosphere, and extends down-dip to > 150 km depth; this layer is commonly interpreted to reflect a tabular fluid-rich shear zone (e.g., Abers,

2005; Audet and Schaeffer, 2018; Hansen *et al.*, 2012). However, the composition and deforming thickness of this zone lacks direct constraints, which may be obtained from a study of exhumed plate boundaries.

1.2 Main research questions

To understand the geological processes which influence the style of plate boundary slip, I will present the results of field, microstructural, and geochemical analysis of three exposures of exhumed plate boundary shear zones on Kyushu, SW Japan. The Makimine mélange contains subducted sediments and oceanic crust deformed within the upper prehnite-pumpellyite facies, and the greenschist facies. Coastal Makimine mélange exposures experienced a peak metamorphic T $\sim 328 \pm 30$ °C (Ujiie *et al.*, 2018), near the prehnite-pumpellyite - greenschist facies transtion, while inland Makimine mélange exposures experienced warmer conditions, with peak metamorphism at $\sim 370 \pm 30$ °C (Ujiie *et al.*, 2021), well within the greenschist facies. The amphibolite facies Nishisonogi Metamorphic Rocks (NMR) show oceanic crust, subducted sediments, and serpentinite, and record a peak metamorphic T $\sim 500 \pm 50$ °C (Ujiie *et al.*, 2021). As described in further detail in Section 3, these shear zone exposures preserve plate-boundary deformation at a range of conditions along a similar Late Cretaceous margin, and reflect a transect from the base of the thermally-defined seismogenic zone to the mantle-wedge corner. The main research questions I ask are:

Q1: What types of structural fabrics (i.e. fractures, foliations) are present, what are their orientations, and how are they distributed between lithologies and metamorphic grades?

Q2: What lithologies occur within the plate boundary shear zone, and how is strain distributed between these lithologies?

Q3: What is the state of stress within the plate boundary shear zone across the base of the seismogenic zone?

Q4: What are the dominant grain-scale deformation mechanisms within the plate boundary, what is the likely mechanical behaviour of the shear zone, and how does it vary with depth?

Q5: How do hydrous fluids influence deformation style?

Q6: How, and where, might frictional instabilities arise down-dip of the base of the seismogenic zone?

1.3 Thesis outline

Following this short introduction, this thesis comprises four parts: (1) A general introduction to concepts relating to stress and strain in the lithosphere, highlighting deformation mechanisms relevant to the subduction plate boundary. (2) The geological context of the studied exhumed shear zones, on the basis of a combination of original work and published literature. (3) Three chapters of original scientific work, using observations from the exhumed shear zones to investigate: grain-scale deformation mechanisms and metamorphic processes within the plate boundary, and controls on the distribution of brittle fracturing (Chapter 4); the strength of hydrated oceanic crust (Chapter 5), and the grain-scale deformation mechanisms in serpentinised fore-arc mantle, and controls on brittle fracturing in serpentinite (Chapter 6). Finally, (4) a final chapter integrating the findings of chapters 4, 5, and 6 in a general discussion addressing questions Q1 to Q5 above.

Among the three science chapters, Chapter 4 considers the geometry and distribution of brittlely and ductilely developed structures in each of the studied shear zone exposures, and uses thermodynamic modelling and oxygen isotope analyses to understand geological processes that control the distribution of brittle fracturing between the base of the thermally-defined seismogenic zone and the mantle wedge corner. Chapter 5 builds on Chapter 4 by quantitatively determining the magnitude of differential stress in two of the studied shear zone exposures, primarily with reference to differential stress levels in hydrated oceanic crust. This chapter is derived from a published paper (Tulley *et al.*, 2020). Chapter 6 focusses specifically on serpentinite exposed in the NMR, and uses outcrop and microstructural observations to determine the mechanisms responsible for deformation of antigorite serpentinite at mantle-wedge conditions.

Chapters 4, 5, and 6 are wholly or partly derived from published papers, or manuscripts prepared for submission to peer reviewed journals. Chapter 4 is derived from a manuscript prepared for submission to *Geochemistry, Geo-*

physics, Geosystems. Christopher Tulley is the lead author of the manuscript, and Åke Fagereng, Kohtaro Ujiie, Johann Diener, and Chris Harris are co-authors (in order of appearance). Christopher Tulley undertook the field work, microstructural analysis, thermodynamic calculations, and wrote the manuscript. Åke Fagereng helped with the field work, provided a derivation for an equation required to plot Fig. 4.10, and gave guidance and constructive comments during all stages of writing. Kohtato Ujjie also helped with the field work. Johann Diener assisted with setting up and troubleshooting thermodynamic calculations. Chris Harris performed the oxygen isotope analyses. Kohtato Ujiie, Johann Diener and Chris Harris gave constructive comments on an earlier draft of the manuscript.

Chapter 5 is derived from a paper published in *Science Advances* (Tulley *et al.*, 2020). Christopher Tulley is the lead author of the manuscript, and Åke Fagereng and Kohtaro Ujiie are co-authors (in order of appearance). Christopher Tulley and undertook the field work and microstructural analysis, and wrote the manuscript with input from Åke Fagereng and Kohtato Ujjie, who also helped with the field work. Two anonymous reviewers provided constructive reviews that improved the work.

Chapter 6 is derived from a manuscript prepared for submission to a peer reviewed journal. Christopher Tulley is the lead author of the manuscript, and Åke Fagereng, Kohtaro Ujiie and Matthew Tarling and are co-authors (in order of appearance). Christopher Tulley is the main author of this work, and wrote the manuscript with input from Åke Fagereng. Kohtaro Ujiie and Åke Fagereng helped with the field work. Christopher Tulley and Matthew Tarling jointly preformed the Raman spectra analysis.

Chapter 2

Stress, strain, and deformation mechanisms

2.1 Stress in the lithosphere

The stress state at any point in the crust is a tensor quantity, but can be represented by the magnitude and orientation of the mutually orthogonal greatest, intermediate, and least principal compressive stresses ($\sigma_1 \geq \sigma_2 \geq \sigma_3$). The magnitude of stress is defined as positive in compression. Where the principal compressive stresses are equal, the normal stresses that act on any surface are equal and no shear stresses exist in the material (Ramsay, 1967). This state of stress is termed hydrostatic. The anisotropic component of the stress tensor, known as the deviatroic stress σ_d, is the difference between the total stress tensor σ and hydrostatic stress $\bar{\sigma}$ (Ramsay, 1967):

$$\sigma_d = \sigma - \bar{\sigma} = \sigma - \frac{\sigma_1 + \sigma_2 + \sigma_3}{3} \tag{2.1}$$

In an isotropic material, hydrostatic stress states can only achieve isometric volume strains; non-zero deviatoric stresses are required to achieve non-isometric strains. Differential stress is the difference between the greatest and least principal compressive stresses ($\sigma_1 - \sigma_3$). In a rock with homogeneous porosity, compressive stresses are reduced by pore fluid pressure (P_f) so that the effective principal stresses ($\sigma^{'}$) are:

$$\sigma_1^{'} = (\sigma_1 - P_f) \geq \sigma_2^{'} = (\sigma_2 - P_f) \geq \sigma_3^{'} = (\sigma_3 - P_f) \tag{2.2}$$

Similarly, the effective vertical stress in a rock mass is defined as:

$$\sigma_v^{'} = \rho g z - P_f = \rho g z(1 - \lambda) \tag{2.3}$$

where ρ is the density of the overlying rock, g is acceleration due to gravity, z is depth of burial and λ is the pore fluid factor relating pore fluid pressure and vertical stress:

$$\lambda = P_f / \sigma_v \tag{2.4}$$

2.2 Descriptions of strain

Strain occurs in response to an applied stress, and is a measure of a change in shape. In this work, the term brittle describes discontinuous deformation (e.g. fractures), while the term ductile describes strains in a continuum at the specific scale of observation (Fig. 2.1). For example, discontinuous slip between many mm-sized grains at the scale of an outcrop is considered a ductile strain, but no mechanism of deformation is inferred. Ductile strains are commonly described by the strain ellipsoid, defined by the three mutually orthogonal principal strain axes $X \geq Y \geq Z$. The lengths of the principal strain axes are referred to as the principal stretches, defined as final over original length, and the length and orientation of the principal axes reflect the finite strain (Fig. 2.2). Strains that do not result in changes to the orientation of the principal strain axes (e.g. Fig. 2.2a) are coaxial strains. Non-coaxial strains occur where the principal strain axes rotate (e.g. Fig. 2.2b). Strains where $X \gg Y > Z$ result in stretching, and the formation of prolate (e.g. pencil) shapes from an initial sphere. Strains where $X > Y \gg Z$ result in flattening, and the formation of oblate (e.g. pancake) shapes from an initial sphere. Intermediate between stretching and flattening strains are plane strains, where the Y axis of the strain ellipsoid is constant, and strain only occurs in the XZ plane. Simple shear, shown in Figs. 2.1 and 2.2b, is a specific type of non-coaxial plane strain. This process is analogous to shearing a deck of cards, where each card slides past it's neighbour, resulting in extension of the pack, but the length of the short side of card pack does not change.

In a single dimension, shortening or extension are defined as an axial strain (ϵ), where l_i and l_f represent the initial and final lengths of a line:

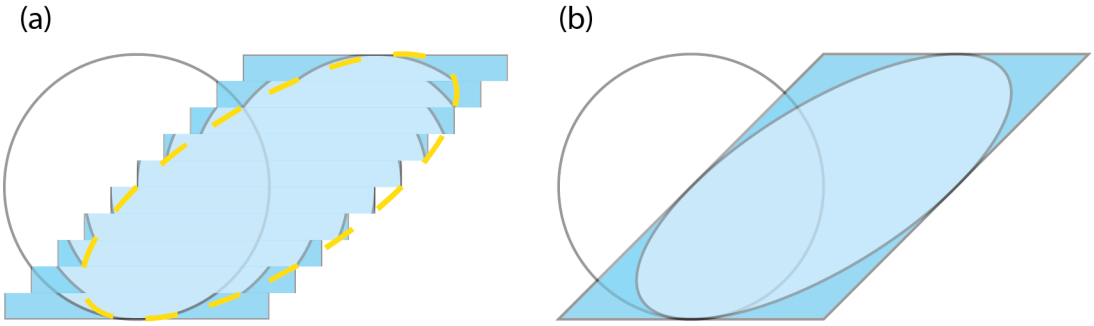

Figure 2.1: The term brittle refers to structures that are discontinuous (e.g. (a)), while the term ductile refers to structures that are continuous (e.g. (b)). However, structures that appear brittle at a small scale may appear ductile at a larger scale, so use of the term ductile depends on the scale of observation.

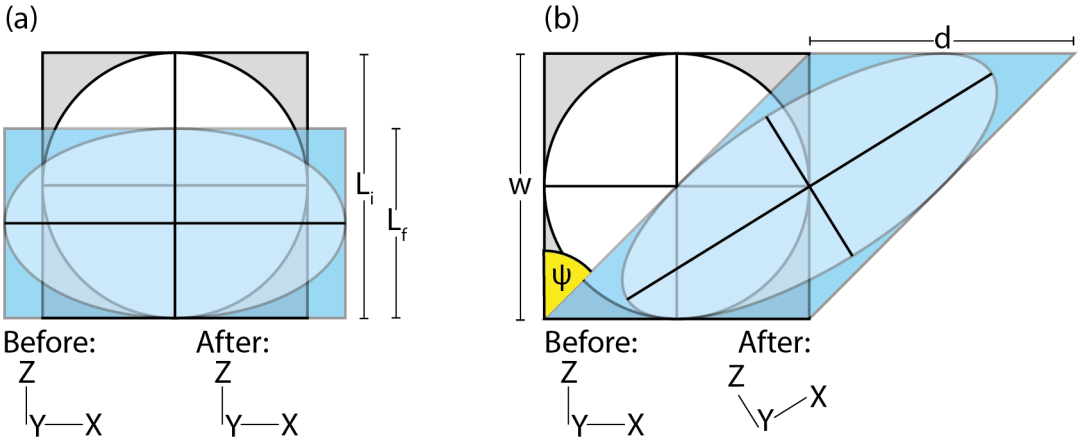

Figure 2.2: Geometry of a coaxial flattening strain (a) and a non-coaxial simple shear strain (b) in two dimensions, showing the evolution of the principal strain axes during strain. The grey square shows the initial shape, and the blue polygon is the final shape.

$$\epsilon = (l_f - l_i)/l_i \tag{2.5}$$

Shear strain is defined by the change in angle between two originally orthogonal lines within a plane, and is defined as the tangent of the angular shear ψ:

$$\gamma = tan\,\psi \tag{2.6}$$

Re-casting equation 2.6 to reflect displacement (d) on a shear zone of thickness (w), as shown in Fig. 2.2b, gives:

$$\gamma = \frac{d}{w} \tag{2.7}$$

The magnitude of a strain divided by the time of which the strain occurred gives the strain rate, typically expressed in the unit s^{-1}.

2.3 Brittle failure criteria

Macroscopic brittle failure investigated in this thesis can be described by a series of failure criteria based on macroscopic observations. Strength envelopes for planes within homogeneous rock under tension and compression can be plotted in shear stress (τ) - effective normal stress ($\sigma_n^{'}$) space on a Mohr diagram, e.g., Fig. 2.3. The Mohr circle has a diameter ($\sigma_1 - \sigma_3$), representing the stress field in the $\sigma_1 - \sigma_3$ plane, and failure is predicted to occur when the Mohr circle intersects the failure envelope.

Shear failure under compression is described by the Coulomb criterion, which states that failure occurs when the shear stress resolved on a plane exceeds the critical shear stress τ_f (Amontons, 1699; Coulomb, 1821; Jager *et al.*, 2007):

$$\tau_f = C + \mu(\sigma_n - P_f) \tag{2.8}$$

Where μ is a friction coefficient and C is cohesive strength. If the rock is intact, μ will be the angle of internal friction (μ_i), which may differ from the angle of sliding friction (μ_f) which is applied when considering sliding along a pre-existing fault. However, Savage *et al.* (1996) argue that μ_i may be considered

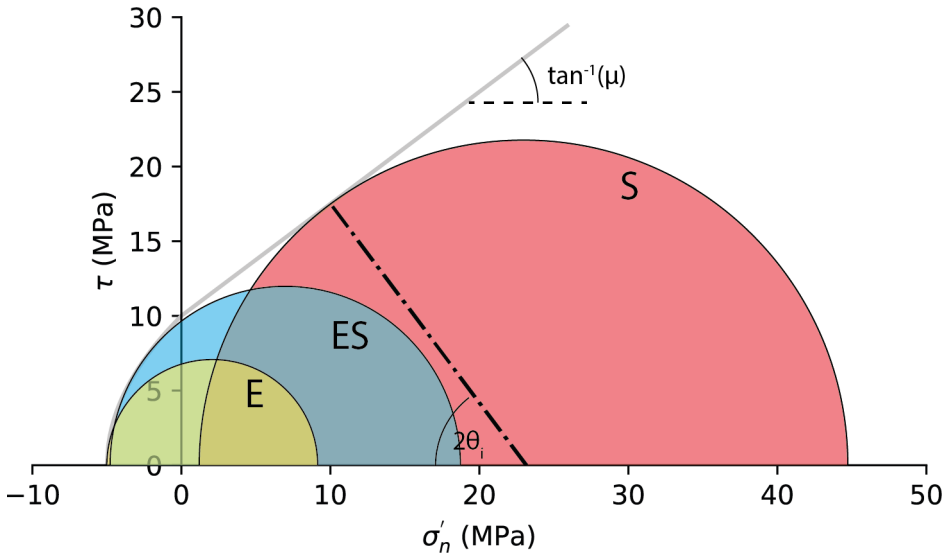

Figure 2.3: Mohr diagram showing the Coulomb-Griffith failure envelope for intact rock, assuming $T_0 = 5$ MPa and $\mu = 0.75$. Circles labelled E and ES represent differential stress conditions under which extension and extension-shear failure will occur, respectively. The circle labelled S represents greater differential stresses conditions than the other circles, and will produce shear failure. The dashed line within circle S indicates the ideal orientation of new fractures containing σ_2 at an angle 2θ to σ_1; other orientations relative to σ_1 will require larger differential stresses before failure occurs.

equal to μ_f, as incipient slip prior to rupture occurs along pre-existing micro-cracks. μ reflects the resistance to sliding along a plane under a given normal stress, and is calculated as the ratio of shear stress to normal stress.

In an isotropic rock, faults form at an angle θ_i to σ_1, where θ_i depends on the slope of the Coulomb failure envelope, $\tan^{-1}(\mu_i)$ (Fig. 2.3), (Anderson, 1951):

$$\theta_i = 0.5 \tan^{-1}\left(\frac{1}{\mu_i}\right) \tag{2.9}$$

Experimentally determined values for μ_i typically lie in the range $0.5 < \mu_i < 1$ (Jager *et al.*, 2007), so for a representative case where $\mu_i = 0.75$, θ_i is approximately 27 °. Critical shear stresses for failure along planes under tension (i.e. negative σ_n') is described by the Griffith criterion, where T_0 is the tensile strength (Griffith, 1924):

$$\tau_f = \sqrt{4\sigma_n' T + 4T^2} \tag{2.10}$$

Extension failure without a component of shear requires zero resolved shear

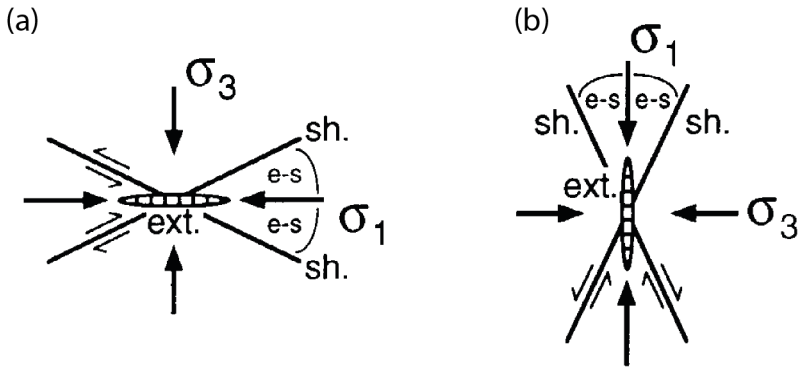

Figure 2.4: Schematic showing the geometric relationship between fracture type and stress orientations, for newly formed shear (sh), extension-shear (e-s) and extension (ext.) fractures. (a) Fractures formed under principal stress orientations favouring extensional tectonic regimes. (b) Fractures formed under principal stress orientations favouring compressional tectonic regimes. σ_2 is the normal to the page. From Sibson (1998).

stress in the $\sigma_1\sigma_3$ plane, meaning that this mode of fracture occurs on a Mohr diagram at the intersection of the Griffith criterion and the normal stress axis in the tensile part of the diagram. This failure criteria can only be met when $\theta_i = 0$ (Fig. 2.3), and tensile fractures therefore occur on planes that contain σ_1, and are perpendicular to σ_3 (Fig. 2.4), where the condition $\sigma_3^{'} = -T_0$ is met. End-member extension fracturing is restricted to stress conditions where $\sigma_1 - \sigma_3 < 4T_0$, as at higher differential stresses the fracture would contain a component of shear (Etheridge, 1983, Fig. 2.3;). Hybrid-extension shear fractures form at slightly higher differential stresses than extension fractures, with the maximum differential stress dependent on T_0 (Fig. 2.3, Eq. 2.10). These type of fractures occur where differential stresses are too large for extension fractures, but small enough so that the perimeter of the Mohr circle can enter the tensional side of the diagram without shear fractures forming. Extension-shear fractures are expected to form at angles to σ_1 that are intermediate between those of shear and extension fractures (Fig. 2.4).

While Mohr diagrams have been used extensively in investigating stress conditions for rock failure, one of the shortcomings of the Mohr construction is the difficulty to visualise the effect of different stress regimes. Sibson (1998) introduced a method for plotting the stress conditions where different modes of brittle failure occur, in both compressional and extensional tectonic regimes. Brittle failure mode plots (e.g., Fig. 2.5a) assume Andersonian principal stress regimes, and show failure envelopes rooted in Equations 2.8 and 2.10, and the

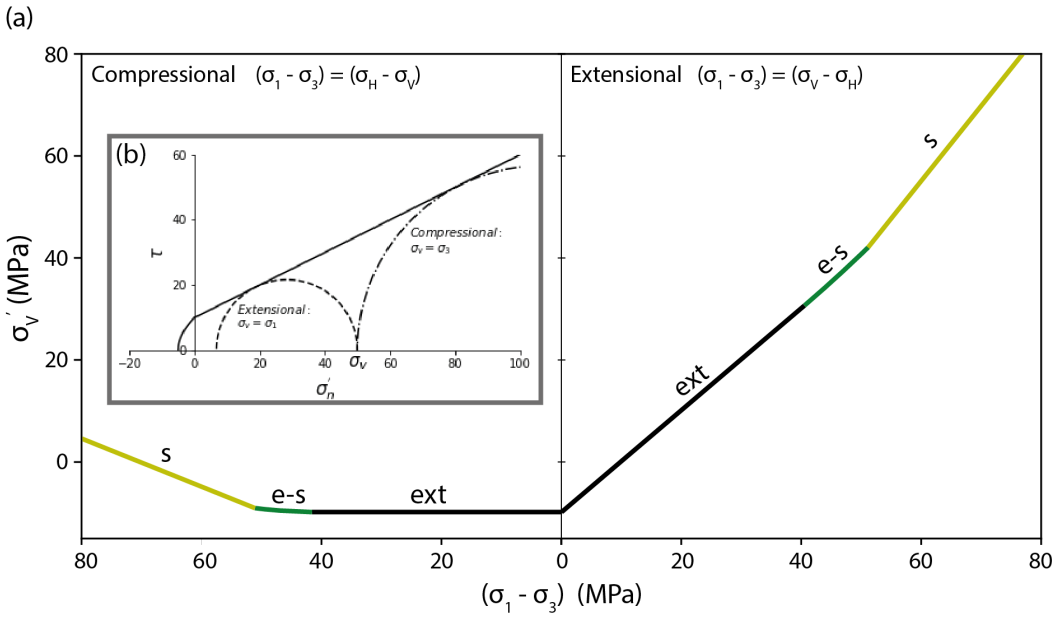

Figure 2.5: Brittle failure under Andersonian compressional and extensional stress regimes. (a) Brittle failure mode plot showing a failure envelope for intact rock (tensile strength 5 MPa, μ_i=0.6), showing the position of different failure modes, indicated as shear (sh), extension-shear (e-s) and extension (ext.) (b) Mohr diagram showing that for a given value of effective vertical stress, greater differential stresses are possible in compressional tectonic regimes.

extension failure criterion $\sigma_3^{'} = -T_0$.

The effect of different tectonic regimes is easily visualised on a brittle failure mode plot: Fig. 2.5a shows that failure occurs at greater ratios of effective vertical stress to differential stress in extensional tectonic regimes, than in compressional tectonic regimes. In other words, for a given effective vertical stress, failure occurs at greater differential stresses in compressional tectonic regimes than in extensional regimes. Fig. 2.5b shows this effect in Mohr space; with the value of σ_v fixed, Mohr circle diameters (corresponding to differential stress) to intersect the failure envelope are much greater when $\sigma_v = \sigma 3$ (i.e., a compressional regime), than $\sigma_v = \sigma 1$ (i.e., an extensional regime).

2.4 Fractures and mineral veins

The orientation and internal structure of veins should reflect the mode of fracture formation, as well as stress conditions at the time of fracture opening, as long as later deformation has not overprinted these features. As described in Section 2.3, fractures can be classified into shear, extension-shear, and extension modes, each which preserve distinct geological structures. End-member shear fractures, at least in an isotropic medium, do not generate open space for mineral precipitation, and therefore tend to not to host veins. However, most rocks contain some anisotropy, and fracture planes are rarely perfectly planar. Slip along an irregular surface creates local dilation along the fracture plane, and space for the precipitation of minerals (Fig 2.6). Irregularities in the shear surface are preserved as lineations on the mineralised fracture plane, and record the shear direction. Over cycles of slip and precipitation, multiple generations of precipitated material build up, typically separated by secondary minerals, fluid inclusion planes, or wall-rock particles (Fig 2.6b). The orientation of these layers records the sense of shear. In Fig. 2.6a, an extension vein, identified by a partially filled opening parallel to the vein walls, occurs perpendicular to the slickenfibres on the shear vein surface. In this work, extension veins are identified by partially filled openings parallel to vein walls, and the absence of slickenfibers on vein surfaces and the absence of dilatational jogs.

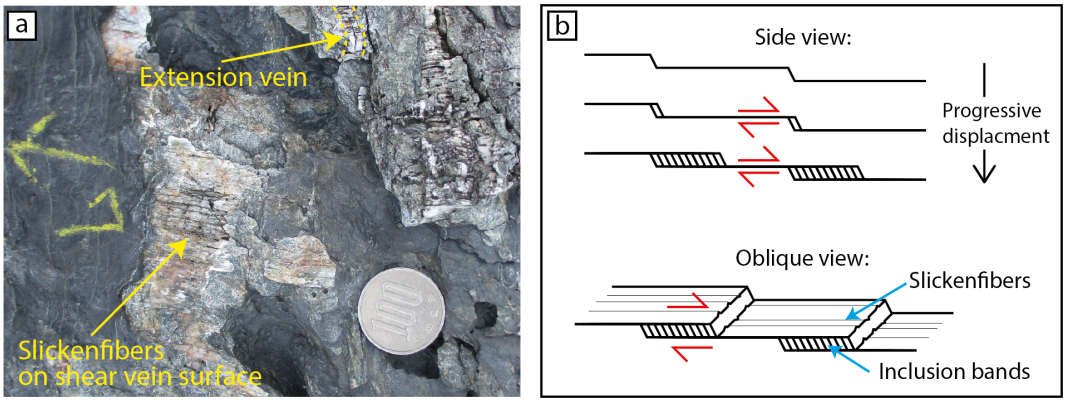

Figure 2.6: Geometry of shear and extension veins. (a) Slickenfibres on the surface of a shear vein from coastal Makimine mélange, adjacent to a partially sealed extension vein. L chalked onto the rock marks the direction of the regional lineation. (b) Schematic showing the formation of slickenfibres in the direction of shear, and inclusion bands developed within dilatational jogs along a shear fracture.

2.5 Deformation mechanisms

Rocks deform, in response to an applied stress, by a variety of mechanisms. A first-order distinction can be made between frictional mechanisms (e.g. fracture or sliding along a discontinuity) and viscous mechanisms, where the term viscous is used to describe mechanisms that produce strengths dependent on strain rate (e.g., pressure solution creep and dislocation creep). In the upper few kilometres of the crust, low pressures and temperatures favour fracturing or frictional sliding. With increasing depth, temperature and confining pressure increase, suppressing frictional slip and favouring temperature-dependent viscous mechanisms (Brace and Kohlstedt, 1980; Bürgmann and Dresen, 2008), (Fig. 2.7b). The mechanisms by which rocks deform at the grain scale are commonly divided into three categories (1) fracturing and frictional sliding, (2) dislocation motion, and (3) diffusion processes. Although rocks can deform by either solely frictional or solely viscous mechanisms, mechanisms often occur in combination, and the transition between frictional and viscous regimes is gradual (Sibson, 1984). Slip styles resulting from different dominant deformation mechanisms along the subduction thrust are discussed in detail in Section 2.8.

2.5.1 Fracturing and frictional sliding

Fracturing or frictional sliding occurs where stress conditions within a rock intersect the brittle failure envelope (Fig. 2.3). Most earthquakes or aseismic frictional slip events occur along existing faults, where the strength of the rock is controlled by cohesion (neglectable for a pre-existing fault) and the coefficient of sliding friction of the fault rock.

Byerlee (1978) showed that most rocks have μ_f between 0.6 and 0.85 (defined as the ratio of shear to normal stress at the initiation of sliding), and that shear stress increases nearly linearly with normal stress. Exceptions are clays and phyllosilicates, which have substantially lower friction coefficients ($\mu \sim 0.25$; e.g.Byerlee (1978); Collettini *et al.* (2019); Ikari *et al.* (2011)). Collettini *et al.* (2009) demonstrated that micro-scale fabrics within fault rocks exert a strong control on fault rock strength; rocks of the same mineralogy were dramatically weaker than powdered equivalents lacking a fabric.

The mathematical framework of rate-and-state friction gives an empirical

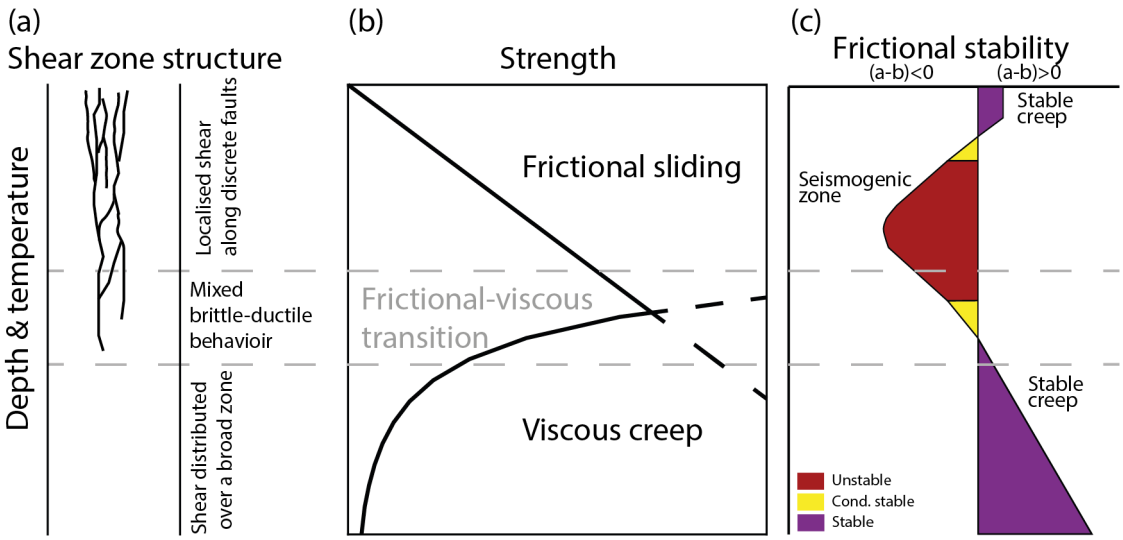

Figure 2.7: Schematic of generalised structure, strength and frictional stability through the lithosphere, extending from the surface into the stably sliding aseismic regime, inspired by Fagereng and Beall (2021). (a, b) At shallow depths an array of faults accommodates slip along discrete planes; with increasing depth the strength of the fault increases until the thermally-activated viscous creep becomes more efficient, and a gradual transition occurs towards distributed viscous shearing (Sibson, 1977). (c) A transition with increasing depth from frictional sliding along discrete planes to distributed viscous creep is also suggested by changes in frictional stability (Scholz, 1998).

relationship between the friction coefficient, rate of deformation, and a "state" parameter. The most commonly applied form, known as the Dieterich-Ruina law (Dieterich, 1979; Ruina, 1983) is given as (Scholz, 1998):

$$\tau = \left[\mu_0 + a \ln\left(\frac{V}{V_0}\right) + b \ln\left(\frac{V_0\theta}{D_c}\right)\right] \sigma_n^{'} \tag{2.11}$$

where V is slip velocity, V_0 is a reference velocity, μ_0 is the steady-state friction (when $V = V_0$), a and b are material parameters, and D_c is the critical slip distance. The state variable θ evolves according to:

$$\frac{\partial\theta}{\partial t} = 1 - \frac{\sigma V}{D_c} \tag{2.12}$$

were time is t, and D_c is the critical slip distance over which μ evolves before reaching a steady-state. The parameter (a-b), which determines frictional stability, can be expressed as:

$$(a - b) = \frac{\partial\mu}{\partial \ln(V)} \tag{2.13}$$

It follows that if (a-b) is positive, then friction increases with increasing slip velocity, and the rock is inherently stable and is said to be velocity-strengthening. If (a-b) is negative, then the friction decreases with increasing slip velocity, and the material is said to be velocity-weakening. If a velocity-weakening material is subject to effective normal stresses greater than a critical value σ_c then the material is unstable (Scholz, 1998):

$$\sigma_c = \frac{kD_c}{-(a - b)} \tag{2.14}$$

where k is the system stiffness, equivalent to the shear zone wall-rock stiffness in a natural fault. It is inferred that earthquakes nucleate in velocity-weakening materials, but cannot nucleate in velocity-strengthening materials. Earthquakes may propagate into velocity-strengthening materials providing slip velocity is sufficiently high, but will terminate rapidly due to the predicted negative stress drop (Scholz, 1998).

2.5.2 Dissolution - precipitation creep

Dissolution-precipitation creep produces deformation by the dissolution of material at one location, transport in a fluid phase, and precipitation at a new

location. To prevent the generation of voids between grain boundaries during dissolution-precipitation creep, grains are required to slide past each other, a process know as grain-boundary sliding. In order to achieve deformation by dissolution and precipitation a mechanism is required which changes the solubility of material between two different locations. Pressure solution is a mechanism that is often attribute as the driver of dissolution-precipitation creep (Gratier *et al.*, 2013); the driving force for pressure solution is a difference in chemical potential (Δp) associated with a normal stress gradient (Paterson, 1973):

$$\Delta p = \Delta f + v\Delta\sigma_n + \Delta E_s \tag{2.15}$$

where v is the molar volume of the stressed solid, $\Delta\sigma_n$ is the normal stress gradient, Δf is the gradient in molar Helmholtz free energy (combining contributions of strain energy relating to dislocations and elastic strain (Gratier *et al.*, 2009; Paterson, 1973), and ΔE_s is the gradient in surface energy, related to the grain boundary geometry. To achieve deformation, material dissolved under a high normal stress is transported some distance, and precipitated where normal stresses are lower. As dissolution, transportation, and precipitation occur in series, the mechanism that is slowest will control the rate of deformation. This effect has given rise to several different pressure solution laws, each with assumptions about which particular step is rate-limiting (Raj, 1982). A stress-strain rate relation for pressure solution has a basic form (Gratier *et al.*, 1999; Raj and Ashby, 1971):

$$\dot{\epsilon} = \Delta\sigma_n/\eta \tag{2.16}$$

Where $\dot{\epsilon}$ is the strain rate and η is a viscosity term. A more descriptive model for pressure solution in the case where diffusion through a fluid phase is the rate limiting step has the form (e.g., Rutter, 1976):

$$\dot{\epsilon} = \frac{I(\Delta\sigma_n)^n v C_o D_b w_f}{RTd^3} \tag{2.17}$$

Or, where dissolution or precipitation kinetics is the rate-limiting step (Raj, 1982):

$$\dot{\epsilon} = \frac{I(\Delta\sigma_n)^n v C_o K}{RTd} \tag{2.18}$$

Where I is constant relating to grain boundary geometry, $\Delta\sigma$ is the difference in normal stress between the site of dissolution and precipitation (which may be taken as the differential stress $(\sigma_1 - \sigma_3)$), n is the stress exponent, v is the molar volume of the solute, C_o is the concentration of a saturated solution in equilibrium with the solid in an unstressed state, D_b is the diffusion coefficient of the solute in the grain boundary fluid, w_f is the width of the fluid layer along the grain boundary, R is the gas constant, T is the absolute temperature, d is the grain diameter, and K is either the dissolution or precipitation rate, whichever is rate-limiting. An alternative approach to deciding which step is rate-limiting is provided by models that determine the limiting step depending on the initial values of kinetic and thermodynamic parameters, and consider, for example, the effects of grain deformation (e.g., Niemeijer *et al.*, 2002) or fluid advection (e.g., Gundersen *et al.*, 2002).

The stress exponent (n), which is calculated as the slope of a plot of stress against strain rate in log-log space, is typically assumed to be 1, although this is an approximation (Gratier *et al.*, 2013). Given that equilibrium solubility, reaction rates, and the rate of ionic diffusion within a fluid are typically material and temperature-dependent, what is apparent from Eqs. 2.16, 2.17, and 2.18 is that d, T and the chemical properties of minerals and the fluid phase, are the principal factors that control the rate of pressure solution creep. It follows that under fluid-present conditions, small grain sizes and warm temperatures, pressure solution creep is likely to be an important deformation mechanism.

2.5.3 Dislocation creep

Dislocations are a type of defect in a crystal structure (Fig. 2.9) which result from the appearance of an extra half lattice plane in the crystal structure. At the end of a half-plane, atomic bonds are stretched to accommodate the dislocation, and pass the half lattice plane along witin the crystal in a specific direction, known as the Burgers vector. Dislocations move in response to external, applied stresses, and elastic stresses generated by other dislocations. In most materials the magnitude of the Burgers vector corresponds to the interatomic spacing (Poirier, 1985). Dislocations may be introduced into a crystal by either breaking of atomic bonds in a line (Frank and Read, 1950), or by irregularities at grain boundaries which migrate into the grain (Murr,

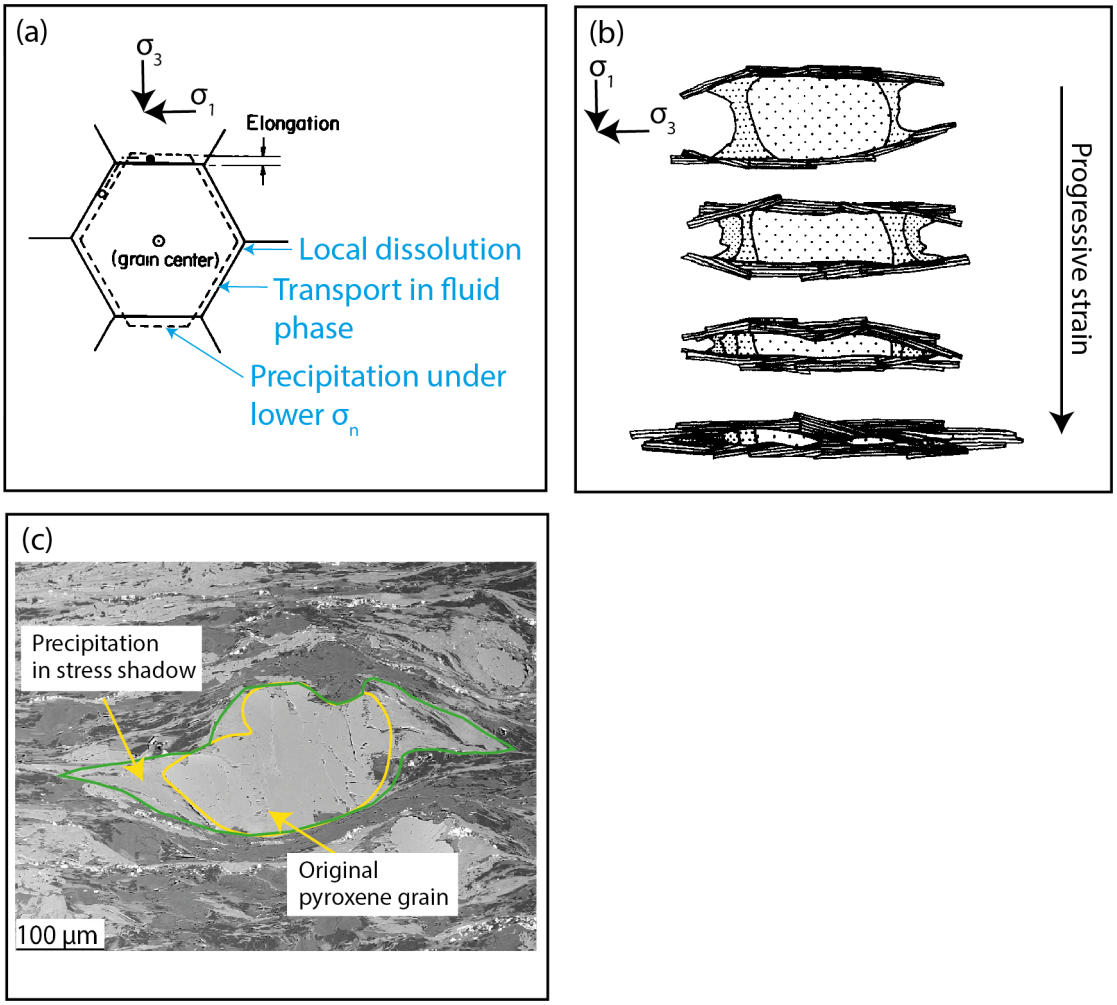

Figure 2.8: Schematic diagrams showing strain by pressure solution creep. (a) Atoms diffuse following a chemical potential gradient related to a gradient in grain boundary normal stress (Eq. 2.15). Sliding between grains is required to prevent dilation. Modified from Raj (1982). (b) Progressive flattening by pressure solution of a grain within a two-phase rock containing a relatively insoluble phyllosilicate phase, leading to the development of a thickened phyllosilicate cleavage. Modified from Schwarz and Stöckhert (1996). (c) Example of a pressure-solution - related microstructure in a naturally deformed metabasalt from inland Makimine mélange.

1975). The motion of dislocations along a particular slip system requires a critical shear stress to be imparted on the slip system in order to achieve substantial deformation (Schmid, 1928; Schmid and Boas, 1935; Wenk and Christie, 1991). The critical resolved shear stress is usually associated with a yield point in a stress-strain curve, representing the stress needed to cause large numbers of dislocations to move such that macroscopic slip is achieved (e.g., De Bresser and Spiers, 1997). The critical resolved shear stress for a particular slip system in a crystal contains effects relating to the density and nature of crystal defects, and the lattice resistance to slip (defined at $0°K$ as the Peierls stress, τ_p (Nabarro, 1997)):

$$\tau_p = \frac{1}{1-\nu} \exp\left(-\frac{2\pi\left(\frac{h}{2(1-\nu)}\right)}{s}\right) \tag{2.19}$$

Where ν is the Poissons ratio of the material, h is the distance between glide planes, and s is the spacing between atoms along the glide plane.

Defects within the crustal lattice such as secondary phases, interstitial or vacant atomic sites, or other dislocations hamper glide, but are able to be passed by two thermally-activated mechanisms; cross-slip and climb. To minimise lattice stresses, dislocations tend to arrange in a configuration with lowest possible energy (Li, 1962), a process termed recovery. Recovery can be achieved by the meeting of dislocations with opposite signs (i.e. two half planes meet and form a whole plane), the stacking of dislocations to form a subgrain boundary, or by dislocations intersecting a grain boundary. At higher strain rates, increased numbers of dislocations are required to facilitate dislocation creep, as expressed in Orowan's equation (Orowan, 1940):

$$\dot{\epsilon} = \rho_d \, \bar{b} \, v_d \tag{2.20}$$

where $\dot{\epsilon}$ is strain rate, ρ_d is the spatial density of mobile dislocations, $\bar{b}$ the length of the burgers vector and v_d the average velocity of dislocation movement. In general, dislocation creep is a competition between hardening (the result of defects and dislocation tangles), and recovery, and a steady strain rate is achieved when the effects of hardening and recovery balance. At strain rates of $10^{-14} - 10^{-11}$ s^{-1}, comparable to natural creep strain rates (Fagereng and Biggs, 2019) recovery facilitates steady rate dislocation creep in quartz at T > 300 °C (Stipp *et al.*, 2002). Below these temperatures dislocation motion

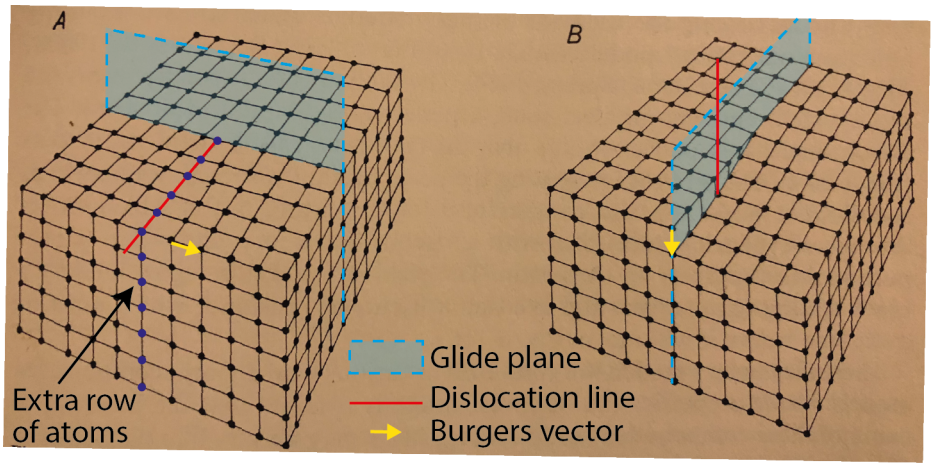

Figure 2.9: End-member types of dislocations in a crystal lattice. (a) Edge dislocations move orthogonal the dislocation line, in the direction of the Burgers vector. (b) Screw dislocations move parallel to the dislocation line and the Burgers vector. In reality, dislocations commonly have a combination of edge and screw kinematics. Modified from Ramsay (1967).

results in strain-hardening and, as a result, fracturing becomes the dominant deformation mechanism. von Mises criteron (von Mises, 1928) states that five independent slip system are required to operate in order to achieve homogeneous deformation by dislocation creep. Deformation experiments and theoretical considerations indicate that in phyllosilicate minerals, common in the shear zones investigated in this work, glide is restricted to the (001) plane (Kronenberg *et al.*, 1990) or in the case of antigorite along conjugate (101) and $(1\bar{0}1)$ planes (Amiguet *et al.*, 2014), suggesting phyllosilicate minerals do not meet von Mises' criterion. However, phyllosilicate minerals in deformed rocks often show intense alignment of (001) planes (e.g., Dempsey *et al.*, 2011), interpreted as an effect of the weak interlayer bonds within (001) planes, and platy habit (e.g., Kronenberg *et al.*, 1990). This alignment may be sufficient for aligned phyllosilicates to accommodate simple shear parallel to (001). Experimental investigation of climb-limited dislocation creep in geological materials typically produces a power-law stress - strain-rate relationship of the form (e.g., Fukuda and Shimizu, 2017):

$$\dot{\epsilon} = A(\sigma_1 - \sigma_3)^n exp\left(\frac{-Q}{RT}\right) \tag{2.21}$$

where A is a material constant, n is the stress exponent, Q is the activation energy, R is the gas constant, and T is temperature.

Dislocations in deformed materials cause distortions in the crystal lattice

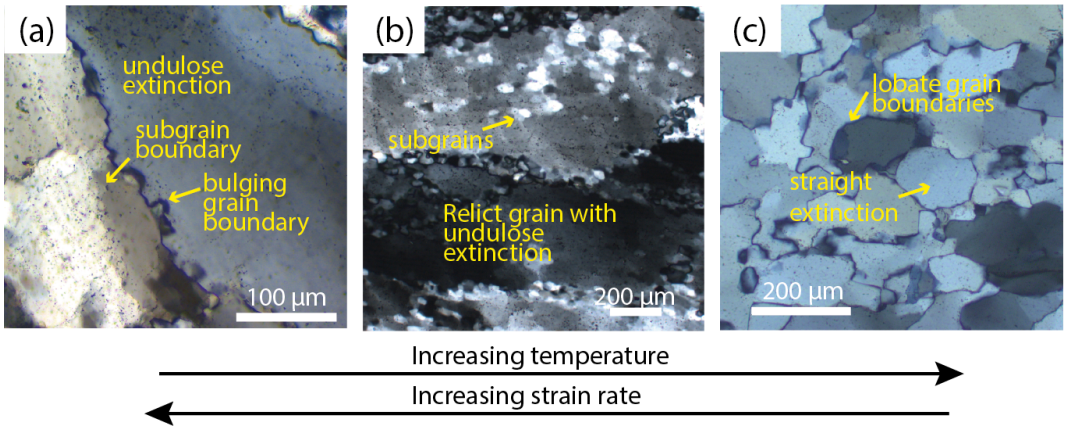

Figure 2.10: Cross-polarised photomicrographs showing characteristic microstructures of dislocation creep regimes in quartzite. (a) Bulging grain boundaries in a quartzite lens from coastal Makimine mélange. (b) Smaller recrystallised subgrains within and surrounding larger relict grains, in a deformed quartz vein from inland Makimine mélange. (c) Irregular shaped grains with lobate boundaries, characteristic of grain boundary migration recrystallisation. Micrograph from a deformed quartz vein in the NMR.

(Fig. 2.9), which appear as undulose extinction under the light microscope (Fig., 2.10). In naturally deformed quartzite, Stipp *et al.* (2002) recognised three different regimes of recovery, each of which have a characteristic microstructure. At low temperature, or high strain rate conditions, recovery occurs by grain boundary bulging. Quartz deformed in the bulging regime shows bulging grain boundaries (e.g., Fig. 2.10a), and relict grains are commonly surrounded by small recrystallised grains. Towards higher temperatures, or lower strain rates, the subgrain rotation mechanism becomes dominant. Quartzite deformed by subgrain rotation typically shows large relict grains with substantial internal distortion, surrounded by recrystallised grains that show relatively straight grain boundaries and little internal distortion (e.g., Fig. 2.10b). With further increase in temperature or decrease in strain rate, recovery occurs by grain boundary migration. This regime operates in a similar way to grain boundary bulging; however where grain boundary migration occurs, conditions are relatively conducive to moving dislocations through the crystal. As a result, grain boundaries sweep through crystals and typically show lobate and interfingered geometries (e.g., Fig. 2.10c).

2.6 Deformation mechanism maps

The dominance of different deformation mechanisms can be illustrated in a deformation mechanism map. These maps represent the dominant deformation mechanism for a material as a function of one of the controlling parameters, such as temperature (e.g., Fig. 2.11), or grain size. Boundaries between the fields for viscous creep mechanisms are interpolated by connecting points where different mechanisms operate at the same strain rate; in other words, in the field boundary region adjoining mechanisms contribute equally to the bulk strain (De Bresser *et al.*, 2001). Within mechanism fields, away from the boundary regions, one mechanism will make a dominant contribution to the bulk strain, however, other mechanisms will also operate, but contribute less to the bulk strain (Poirier, 1985). Construction of such maps for requires laboratory-derived parameters describing viscous creep for each of the mechanisms in a specific material; for a few materials these parameters are available (e.g., quartz, feldspar, olivine, calcite, ice, salt), however for most other minerals, and polymineralic rocks, the parameters (and/or appropriate creep equations) are not known. Fig. 2.11, based loosely on the deformation mechanism maps for quartz and calcite shown in Rutter (1976), shows that dislocation motion dominates at high temperature, high stress conditions (below the brittle failure envelope). Towards lower stresses, at high temperature, Naborro-Herring creep (diffusion through crystal lattices) occurs. Pressure solution creep occurs at temperatures and stresses below the those for Naborro-Herring creep, dislocation creep, and dislocation glide.

2.7 Constraints on stress and viscosity in exhumed shear zones

The orientation and mode of fractures provides an indication of the orientation and magnitude of the effective principal stresses (Fig. 2.4, section 2.3), providing the fractures retain their original orientation. Extension of more viscous layers within layered material results in boudinage or pinch-and-swell of the more viscous layer (e.g. Fig. 2.12), giving a qualitative indication of relative viscosity. Quantifying viscosity or stress using these structures requires assumptions about strain and rheology (e.g., Gardner *et al.*, 2016; Kenis *et al.*,

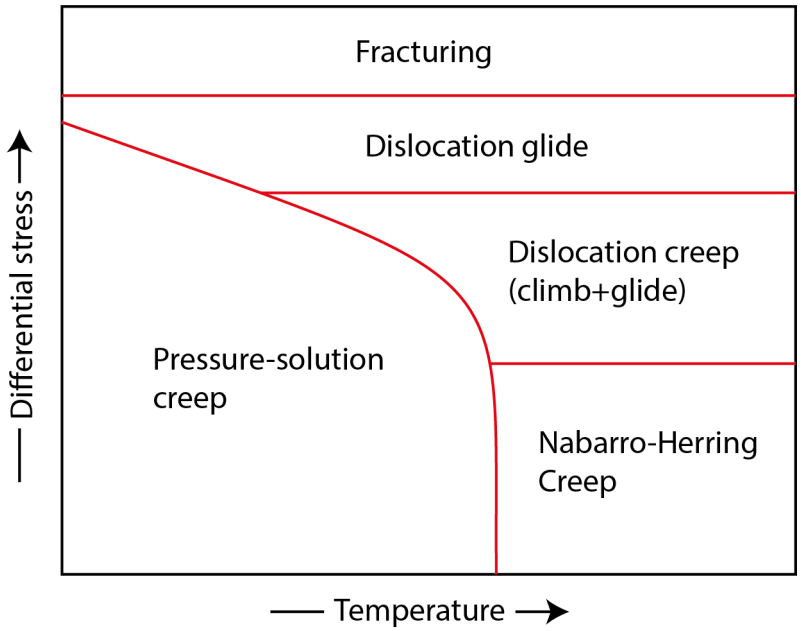

Figure 2.11: Sketched deformation mechanism map in differential stress - temperature space, based on the map for quartz in Rutter (1976).

2005).

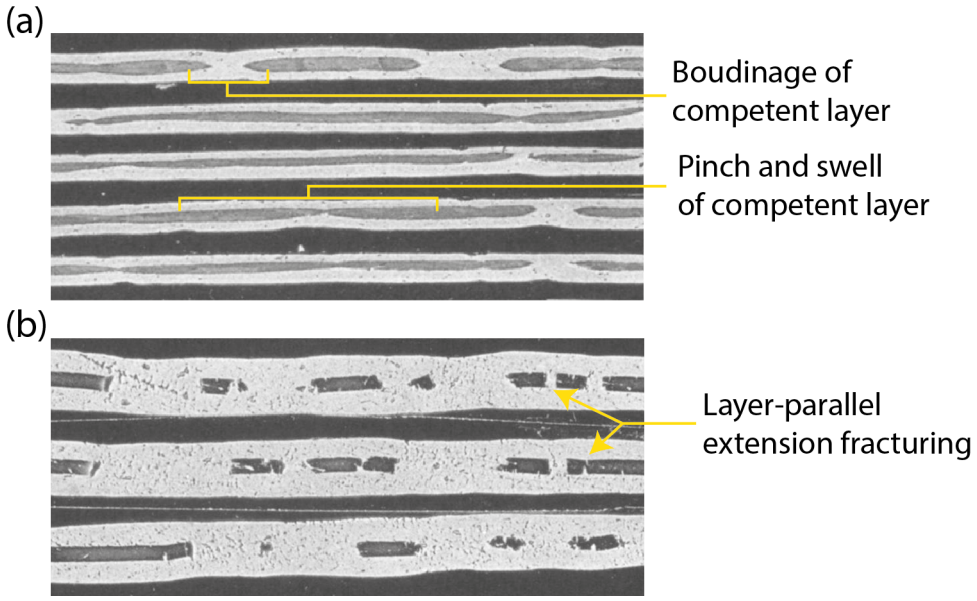

Figure 2.12: Results of experiments involving extension of putty containing layers of (a) plasticine and (b) cheese, with extension parallel to the layering. Modified from Ramberg (1955). Relatively competent plasticine layers show a continuum of structures from subtle pinch and swell to boudinage. The cheese, more competent than both putty and plasticine, lacks pinch and swell, and shows layer-normal extension fractures.

The ductile shear zones studied here contain abundant quartz veins which

deformed by dislocation creep. In a material deforming by dislocation creep, both stress (equation 2.21) and dislocation density (equation 2.20) increase with strain rate. Towards higher stresses (or strain rates) the rate of dislocation production increases, requiring an increase in the rate of recovery and recrystallisation, resulting in smaller recrystallised grain sizes. Several piezometer relationships have been developed that relate recrystallised grain sizes to differential stress, and are commonly of of the form (e.g., Cross *et al.*, 2017; Twiss, 1977):

$$(\sigma_1 - \sigma_3) = \left(\frac{d_{rex}}{o}\right)^{\left(\frac{1}{r}\right)} \tag{2.22}$$

where d_{rex} is the recrystallised grain size, and o and r are empirically determined constants. Recrystallised grain size piezometers can only be applied in single-mineral domains (e.g., deformed quartz veins), which prevents using them to directly constrain the strength of a polyphase aggregate. Less frequently used piezometers relate subgrain sizes to differential stress during creep. This type of piezometer relationship is advantageous, primarily because subgrains develop within individual grains, allowing them to be applied to polymineralic rocks (Goddard *et al.*, 2020).

2.8 Overview of plate interface slip styles

Motion along active plate boundaries (and other fault systems) is accommodated by slip styles that span characteristic durations ranging from infinite (continuous plate-rate creep) to less than a minute (regular earthquakes) (e.g., Gomberg *et al.*, 2016; Kanamori and Anderson, 1975). Intermediate in terms of characteristic duration are tectonic tremor, occurring in episodes lasting hours to days (Fig. 2.13; (e.g., Rogers and Dragert, 2003; Shelly *et al.*, 2006), and slow slip events, lasting between several days to a few months (e.g., Gomberg *et al.*, 2016; Ide *et al.*, 2007).

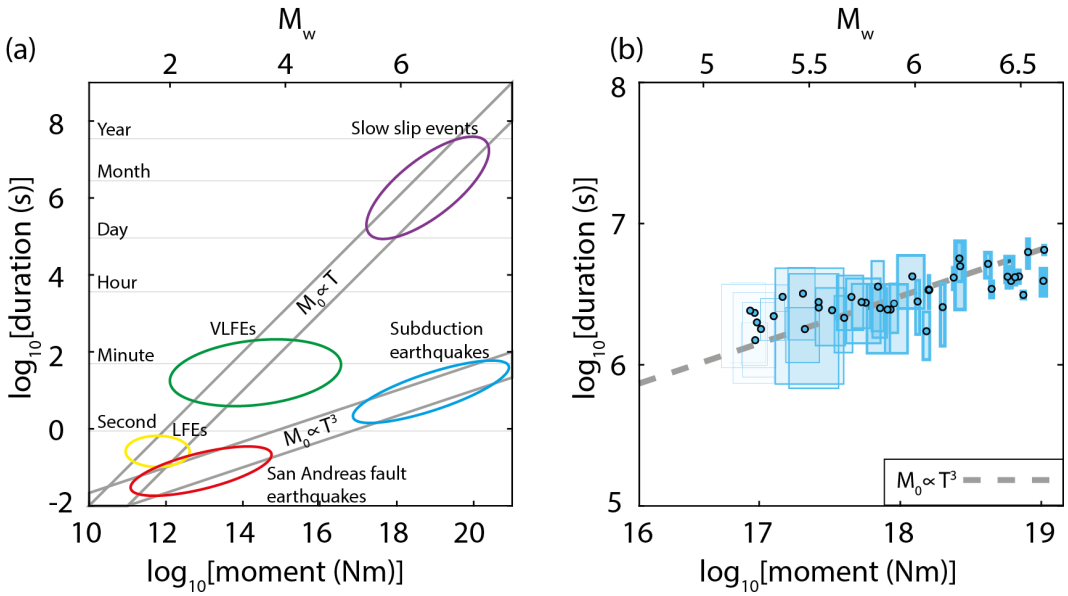

Figure 2.13: Scaling relationships for earthquakes, low and very low frequency earthquakes, and slow slip events, based on data presented in Ide *et al.* (2007), Peng and Gomberg (2010), Gomberg *et al.* (2016), and Michel *et al.* (2019). (a) Slip behaviour spans a wide range of characteristic durations and magnitudes. Typical earthquakes show cubic moment-duration scaling ($M_0 \propto T^3$) (Kanamori and Anderson, 1975), while Ide *et al.* (2007) proposed $M_0 \propto T$ for SSEs, VLFEs, and LFEs. (b) Comparison between moment and duration of SSEs along the Cascadia margin (blue dots, errors indicated by blue boxes), and the $M_0 \propto T^3$ scaling for SSEs proposed by Michel *et al.* (2019). Modified from Michel *et al.* (2019).

2.8.1 Earthquakes

Earthquakes accommodate displacement at rates of around a meter per second, and are the result of frictional failure of unstable or conditionally stable fault rocks (section 2.5.1). Along margins where the location of thrust earthquakes is well constrained (e.g. in Japan, Fig. 2.14), the depth distribution of earthquake hypocenters defines the seismogenic zone. Along other margins where thrust earthquakes are uncommon in the instrumental record (e.g. Cascadia, Hikurangi), the region of geodetic locking between the subducting and overriding plates is inferred to represent the seismogenic zone (e.g., Li *et al.*, 2018; Wallace, 2004). The size of earthquakes is typically measured by seismic moment (Aki, 1967), defined as:

$$M_0 = GA_rD \tag{2.23}$$

Where G is the shear modulus, A_r is the area of the rupture, and D is the aver-

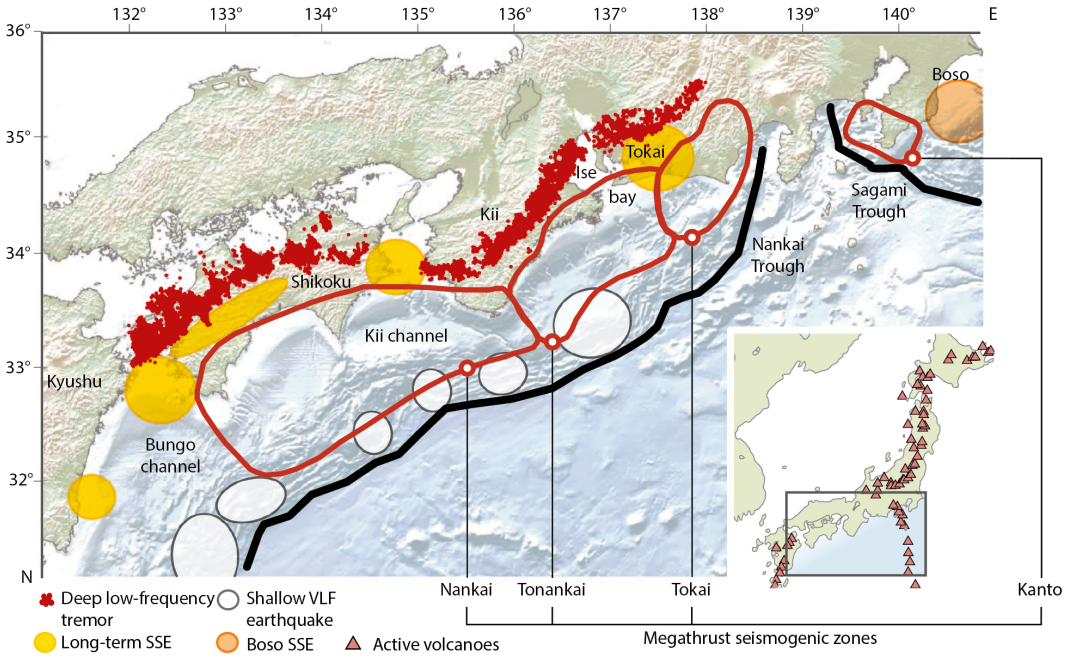

Figure 2.14: Distribution of plate boundary slip behaviour along the SW Japan margin. Tremor and slow slip phenomena occur down-dip of the seismogenic zone, which is defined by the rupture areas of megathrust earthquakes, indicated by the red polygons. The black line shows the surface expression of the plate boundary on the sea-floor. The inset shows the geographic context, with red triangles indicating the location of active volcanoes. From Obara and Kato (2016).

age coseismic displacement across the fault. The empirical moment magnitude (M_w) scale, based on seismic moment, is defined as (Hanks and Kanamori, 1979):

$$M_w = \frac{\log M_0 - 9.1}{1.5} \tag{2.24}$$

The relative frequency of earthquakes of different sizes is approximated by the empirical Gutenberg-Richter relationship, which predicts a power-law distribution of earthquake magnitudes, and that frequency decreases by a factor of 10 for each unit increase in magnitude (Gutenberg and Richter, 1944).

2.8.2 Tectonic tremor and low frequency earthquakes

Tectonic tremor is defined as low-frequency, low amplitude seismic signals that lack the distinct P- and S-wave arrivals used to locate typical earthquakes. Tremor occurring in a subduction zone was first discovered along the SW Japan margin (Obara, 2002), and has since been discovered along many other

active subduction zones, commonly but not always associated with slip rate transients know as slow slip events (Section 2.8.3, Obara and Kato, 2016; Rogers and Dragert, 2003; Wallace, 2020). Tremor occurs over a duration of weeks to months, and is thought to contain swarms of low- and very-low frequency earthquakes (LFEs) (Ito *et al.*, 2009; Katsumata and Kamaya, 2003; Obara and Ito, 2005; Shelly *et al.*, 2006), which have source durations of less than one second and a few tens of seconds, respectively (Peng and Gomberg, 2010). LFEs are thought to represent small magnitude ($M_w < 2$), low stress-drop earthquakes (Ide *et al.*, 2007; Kao *et al.*, 2010; Shelly *et al.*, 2006).

Thermomechanical models of subduction zones indicate the tremor and slow slip along the Cascadia (e.g., McCrory *et al.*, 2014; Peacock, 2009; Wech and Creager, 2011) and SW Japan (e.g., Obara and Kato, 2016; Seno and Yamasaki, 2003; Suenaga *et al.*, 2016) margins occurs where slab-top temperatures are within the range 300-550 °C, i.e. comparable conditions to the studied shear zone exposures. Within this temperature range, and roughly equivalent depths ($\sim 30-45$ km), brittle failure should be suppressed by high compressive stresses (for example, the vertical stress, Eq. 2.3), and low differential stresses resulting from efficient temperature-dependent viscous deformation (Sections 2.5.2, 2.5.3). Assuming a homogeneous shear zone, to achieve frictional deformation at these conditions requires either (a) exceptionally high stresses to intersect the brittle failure envelope, (b) a shear zone containing mechanically weak material, or (c) high pore fluid pressures reducing effective stresses.

Tremor occurrence has been shown to be modulated by small (1-15 kPa) stresses induced by earth and ocean tides (Houston, 2015; Ide and Tanaka, 2014; Nakata *et al.*, 2008; Rubinstein *et al.*, 2008; Thomas *et al.*, 2013), suggesting that stress conditions within the tremor source region are close to critical conditions for brittle failure (Sibson, 2017). High pore fluid pressure is commonly inferred to contribute to tremor and slow slip events by reducing the effective stress (e.g., Bernaudin and Gueydan, 2018; Liu and Rice, 2007; Zhu *et al.*, 2020), and Seno and Yamasaki (2003) showed that tremor was absent in parts of the SW Japan subduction zone inferred to subduct inferred relatively dry island-arc crust. To generate a pore fluid pressure, permeability must be sufficiently low; timescales of silica precipitation have been proposed to control the periodicity of tremor and slow slip (Audet and Bürgmann, 2014; Fisher and Brantley, 2014; Hyndman *et al.*, 2015; Ujiie *et al.*, 2018). However,

while fluid pressurisation driven by metamorphic dehydration is an appealing theory, no specific metamorphic reaction correlates with all tremor occurrence (Peacock, 2009).

2.8.3 Slow slip events

In subduction zones, slow slip events (SSEs) are generally observed near the up-dip and down-dip limits of the megathrust seismogenic zone, and in deeper regions near the mantle wedge corner, and are generally associated with tectonic tremor (Figs. 2.14; 1.1; McCrory *et al.*, 2014; Obara and Kato, 2016; Schwartz and Rokosky, 2007; Wallace, 2020). Instances where tremor and slow slip occur together are termed "episodic tremor and slow slip" (ETS) events (Obara *et al.*, 2004; Rogers and Dragert, 2003). Inversions based on geodetic studies typically show that slow slip events accommodate displacements of a few tens of cm, and that slip occurs periodically, over an area of a few hundred square km, comparable to moderate sized typical earthquakes (e.g., Dragert *et al.*, 2001; Obara *et al.*, 2004; Wallace, 2020). However slow slip events differ from typical earthquakes in that slip occurs at a much slower rate, typically several mm per day (e.g., Bartlow *et al.*, 2014; Bletery and Nocquet, 2020); rates too slow to generate detectable seismic waves. Linde *et al.* (1996) were the first to recognise episodic slow slip events, using borehole strainmeter data from the San Andreas Fault. Slow slip events have since been recognised along many subduction margins, following the deployment of continuous GPS instrumentation, e.g. in Japan (Hirose *et al.*, 1999; Obara *et al.*, 2004), Cascadia (Dragert *et al.*, 2001; Miller, 2002), Mexico (Larson *et al.*, 2004; Lowry *et al.*, 2001), New Zealand (Douglas *et al.*, 2005; Wallace and Beavan, 2006), Alaska (Fu and Freymueller, 2013; Ohta *et al.*, 2006), Costa Rica (Jiang *et al.*, 2012; Outerbridge *et al.*, 2010), and Chile (Klein *et al.*, 2018; Ruiz *et al.*, 2014). Most slow slip events occur with a semi-regular periodicity. For example, slow slip events along the Hikurangi margin in New Zealand accommodate 2-5 cm of displacement over a period of weeks to several months, every 2-5 years (Wallace, 2020; Wallace and Beavan, 2006). As SSEs, like regular earthquakes, represent local release of accumulated elastic stresses, SSEs have been suggested to load adjacent areas of the plate boundary, increasing the probability of an earthquake occurring (Mazzotti and Adams, 2004; Obara and Kato, 2016; Uchida *et al.*, 2016).

The occurrence of slow slip events near the edge of seismogenic regions has led to the suggestion that a transition in frictional properties controls the location of slow slip (Schwartz and Rokosky, 2007). In the framework of rate-and-state friction (section 2.5.1), SSEs have been suggested to arise along the base of the seismogenic zone due to a velocity-dependence of rate and state friction parameters, so that material become stable once a critical velocity is reached (e.g., Im *et al.*, 2020; Shibazaki and Iio, 2003). Small along-strike variations in the parameters a and (a-b) have also been suggested to produce SSEs near the edged of geodetically locked, seismogenic regions (Liu and Rice, 2005). SSEs are also proposed to result from dynamic interaction between frictional and viscous deformation (Ando *et al.*, 2012; Beall *et al.*, 2019a; Hayman and Lavier, 2014; Skarbek *et al.*, 2012) in shear zones containing mixtures of material with different rheology. Slow stick slip events have been produced in the laboratory, suggested to arise from a variety of deformation mechanisms including viscous deformation accompanied by fracture (Reber *et al.*, 2015) and by purely frictional slip (Ikari, 2019; Ikari *et al.*, 2015; Leeman *et al.*, 2016). Recent experiments by Scuderi *et al.* (2020) highlight the potential role of shear zone fabric heterogeneity in the modulation of slow slip events. To summarise, there are many proposed mechanisms for slow slip, but relatively few observations which allow insight into which of the proposed mechanisms operate.

2.8.4 Plate-rate creep

Aseismic, approximately plate rate creep is the dominant slip style at depths below the seismogenic zone, where viscous deformation mechanisms operate at stresses within the brittle failure envelope. However, geodetic inversions (e.g., Scholz and Campos, 2012; Wallace *et al.*, 2009) commonly indicate aseismic creep within inferred seismogenic zones. In these regions, aseismic creep is interpreted to result from variable rate-and-state frictional properties (e.g., Bilek and Lay, 2002; Igarashi *et al.*, 2003), or the operation of pressure-solution creep mechanisms (Fagereng and den Hartog, 2017; Rowe *et al.*, 2013). Slow slip events, which occur episodically (Section 2.8.3), are a form of aseismic creep, so an intriguing problem is understanding what controls whether aseismic creep occurs at a steady rate, or episodically. Numerical models of mixed-material shear zones indicate that the episodic formation and breakdown of

load-bearing networks of strong lithologies might be a source of slow slip periodicity (Beall *et al.*, 2019b)

2.9 Geological controls on fault slip style

Over the ∼20 years since the first observations of slow slip and tremor in subduction zones (Dragert *et al.*, 2001; Obara, 2002), seismic and geodetic data, and thermomechanical models have provided constraints on the location, characteristic duration, periodicity, and source mechanisms of these fault slip phenomena. However, the geological processes which control which fault slip style occurs where, in time and space, is a matter of ongoing work and the main topic of this thesis. Exhumed examples of subduction thrusts provide a chance to examine the geology of the plate boundary, and understand the deformation mechanisms responsible for fault slip behaviour.

Subduction plate interfaces exhumed from T> 250 °C typically show penetrative foliations defined by aligned phyllosilicates (e.g., Behr *et al.*, 2018; Behr and Platt, 2013; Fagereng, 2013; Fagereng *et al.*, 2018; Ioannidi *et al.*, 2020; Muñoz-Montecinos *et al.*, 2020; Rowe *et al.*, 2011; Schwarz and Stöckhert, 1996; Tewksbury-Christle *et al.*, 2021), which are developed in subducted sediments, hydrated oceanic crust, and serpentinite. Continuous, ductile deformation associated with foliation formation is inferred to occur by a viscous creep mechanism coupled to sliding along phyllosilicate foliations (e.g., Behr and Platt, 2013; Fagereng *et al.*, 2014; French *et al.*, 2019; Palazzin *et al.*, 2016; Schwarz and Stöckhert, 1996; Wassmann and Stöckhert, 2013). Psuedotachylite, indicating fast earthquake slip (Sibson, 1975), occurs relatively infrequently in exhumed subduction thrusts (Ikesawa *et al.*, 2003; Phillips *et al.*, 2019; Rowe *et al.*, 2005). However, indications of discontinuous brittle behaviour such as veining (e.g., Fagereng *et al.*, 2014; Fagereng and Sibson, 2010; Kotowski and Behr, 2019; Muñoz-Montecinos *et al.*, 2020; Ujiie *et al.*, 2018), and fracturing of more competent lithologies in a weaker matrix (e.g., Behr *et al.*, 2018; Fagereng, 2013; Fagereng *et al.*, 2014; Kotowski and Behr, 2019) are widespread over a large range in P and T conditions. In exhumed subduction plate interfaces, the ubiquitous presence of foliations developed during continuous creep suggests that a component of the total deformation along active plate boundaries occurs by an aseismic creep mechanism. Discontinuous, brittle deformation in

the form of fracturing and veining, which is commonly overprinted by ductile deformation (e.g., Fagereng *et al.*, 2018; Muñoz-Montecinos *et al.*, 2020) implies that stress conditions locally, and temporarily, exceed the brittle failure envelope. The common occurrence of discontinuous brittle structures over a wide P-T range, in a wide range of lithologies, suggests that the mechanism(s) that drives(s) embrittlement must operate over a broad area of the subduction thrust, and might not have a strong dependance on the deforming lithology or require specific P-T conditions.

While exhumed shear zones provide a change to observe structures developed during subduction deformation, single exposures reflect a time-integrated history of deformation, commonly including deformation related to exhumation. Differentiating structures and mineral assemblages relating to earlier subduction or exhumation is not aways straightforward. Comparisons between differed exhumed shear zones are also hindered by different subduction kinematics, input sequences, and thermal gradients. The Makimine mélange and NMR, exposed on Kyushu, are inferred to have accommodated subduction along a kinematically similar Late Cretaceous Eurasian margin. Therefore, these shear zone exposures represent an opportunity to examine progressive deformation to different finite strains and metamorphic grades, developed during subduction along a kinematically similar margin.

Chapter 3

Exhumed shear zones on Kyushu, SW Japan

The Makimine mélange and Nishisonogi Metamorphic Rocks (NMR) on Kyushu, SW Japan (Fig. 3.1), show subduction-related structures and prograde metamorphic mineral assemblages developed at different P and T conditions along a similar, Late Cretaceous margin. Each shear zone exposure contains subducted sediments, oceanic crust, and for NMR, serpentinite. The peak metamorphic grades in this series of exposures range from the prehnite-pumpellyite to greenschist facies transition, to the greenschist to amphibolite facies transition (Section 4.7), recording peak metamorphic temperatures between 328 ± 30 °C (Ujiie *et al.*, 2018) and $\sim 500 \pm 50$ °C (Ujiie *et al.*, 2021). Serpentinite deformed within the NMR suggests that this exposure was exhumed from near the mantle wedge. These shear zones therefore span the inferred thermally-controlled seismic-aseismic transition at ∼350 °C (Brace and Kohlstedt, 1980; Hyndman *et al.*, 1997) and the mantle-wedge corner, where episodic tremor and slow slip phenomena occur (Obara and Kato, 2016; Schwartz and Rokosky, 2007; Wallace, 2020).

The basement geology of SW Japan is dominated by approximate E-W trending terranes comprising sea floor and trench-fill sediments, and oceanic crust (Figure 3.1), accreted to the eastern Eurasian margin during a history of margin tectonics, beginning in the Cambrian (Isozaki *et al.*, 2010). On the east coast of Kyushu, the Makimine mélange occurs within the Late Cretaceous Shimanto Accretionary Complex (Figure 3.2), a domain of Late Cretaceous to Miocene sediments and oceanic crust, exposed from central through southern

Japan (Hara and Kimura, 2008; Kimura, 1997; Taira *et al.*, 1982), (Figure 3.1). On the west coast of Kyushu, the Nishisonogi metamorphic rocks, which have a Cretaceous metamorphic age (Faure *et al.*, 1988; Hattori and Shibata, 1982), occur within the Nagasaki Terrane. On the basis of similarities in lithology, metamorphism, and protolith and metamorphic ages, some authors suggest the NMR is an extension of the Sanbagawa terrane exposed on Shikoku and Honshu (Miyazaki *et al.*, 2016), however this correlation is not universally accepted (Wallis *et al.*, 2020), and the NMR may be an separate terrane.

3.1 Makimine mélange

The Makimine mélange, exposed from eastern to central Kyushu (Fig. 3.3) contains metamorphosed and deformed ocean plate sediments and oceanic crust. The mélange is interpreted to have accommodated subduction thrust shear at upper prehnite-pumpellyite to lower greenschist facies conditions (Mackenzie *et al.*, 1987; Ujiie *et al.*, 2018). In coastal (eastern) exposures of the mélange, oceanic plate stratigraphy is generally preserved; lenses of greenish metabasalt and reddish mudstone are overlain by reddish-brown tuff, in turn overlain by sandstone-mudstone mélange and coherent turbidites (Figure 3.4). This stratigraphic sequence is repeated at least twice, perhaps because of underplating (Ujiie *et al.*, 2018). Bedding planes within coastal Makimiine mélange generally strike east-west and dip gently to the north (Fig. 3.4a), and foliation is subparallel to bedding (Fig. 3.4b). Stretching lineation defined by the long axes of sandstone and metabasalt lenses is subparallel to foliation dip (Fig. 3.4b). Raman spectra of carbonaceous material (RSCM) in pelite from coastal mélange exposures suggest peak metamorphism at 328 ± 30 °C (Ujiie *et al.*, 2018). Inland exposures of the Makimine mélange, occur along discontinuous sections of river-bed near the junction of the Tsunanose and Gokase Rivers (approx. 32.6128 °N, 131.4512 °E). Time constraints and generally poor exposure prevented detailed geological mapping at this locality. Exposures in river-beds show meter to centimetre thick, mostly continuous layers of metabasalt and metasediments (Fig. 4.2). The orientation of foliations and stretching lineation are similar to coastal Makimine mélange exposures (Fig. 3.4b), and lithological layering is subparallel to foliation (Fig. 4.2b). RSCM thermometry of pelite from inland mélange exposures indicates a peak metamorphism

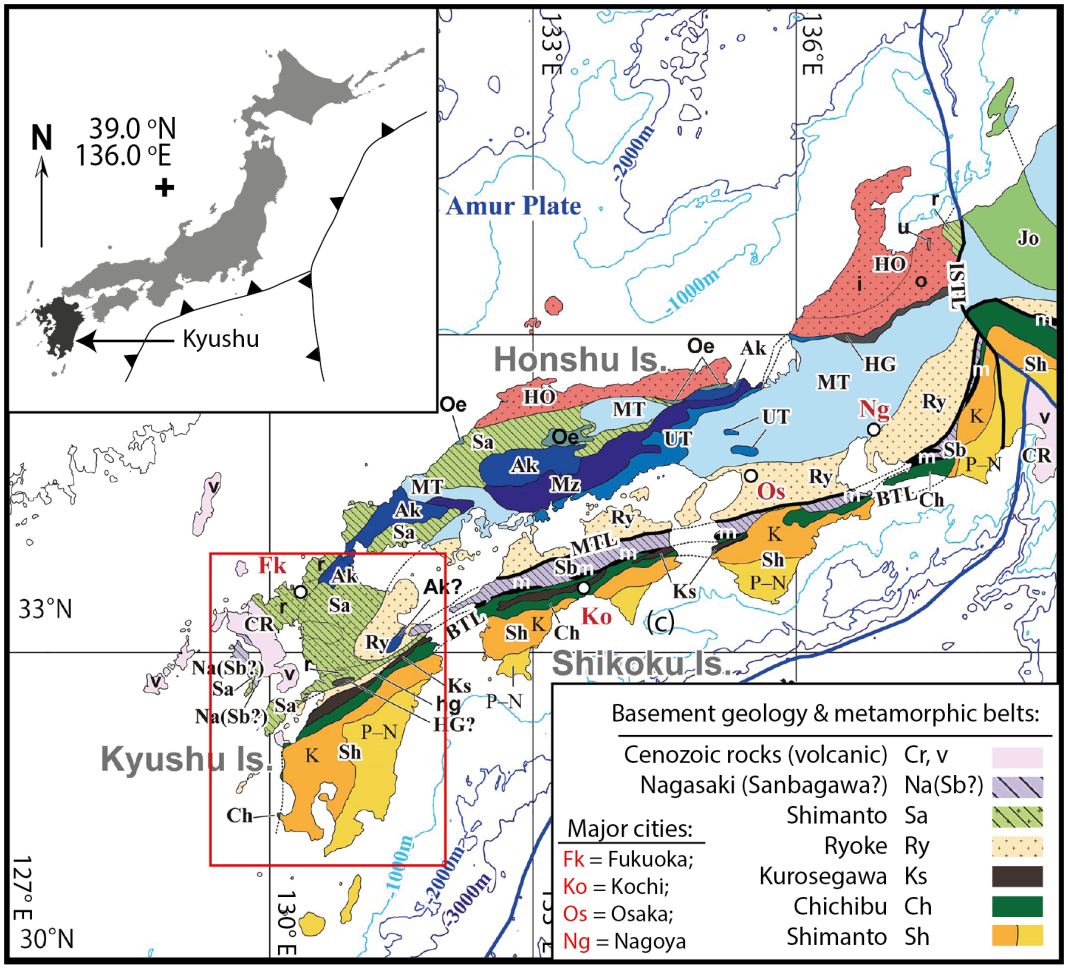

Figure 3.1: Location, active plate boundaries and regional-scale geology of SW Japan (adapted from Wallis *et al.*, 2020). The red rectangle shows the approximate extent of Fig. 3.2. The legend shows a section of terranes with the largest areal extent on Kyushu, and those most relevant to this work, for brevity. For the complete legend, the reader is referred to Wallis *et al.* (2020). The Nagasaki Terrane and Sanbagawa Terrane are coloured the same, owing to a potential but uncertain correlation between these units.

at 371 ± 30 °C, slightly warmer than for coastal exposures (Ujiie *et al.*, 2021).

3.2 Nishisonogi Metamorphic Rocks

The NMR consists of pelitic and psammitic schists, amphibolite, and serpentinite (Figure 3.5). The youngest U-Pb age for detrital zircon in the pelitic schist is 86 Ma (Kouchi *et al.*, 2011), suggesting deposition of the deformed and metamorphosed lithologies occurred as early as the Late Cretaceous. Ar-Ar and K-Ar ages range between 95-60 Ma for glaucophane, muscovite and biotite in pelitic schists, and are interpreted to reflect Late Cretaceous or early Paleocene metamorphism (Faure *et al.*, 1988; Hattori and Shibata, 1982). RSCM thermometry of pelite suggests peak metamorphism at $\sim 500 \pm 50$ °C (Ujiie *et al.*, 2021), broadly consistent with RSCM estimates by Mori *et al.* (2019) and the epidote-blueschist facies mineral assemblage. In the NMR there is no intact ocean plate stratigraphy preserved; rather, metamorphosed components of an ocean floor sequence, including amphibolitic, psammitic, and pelitic schists are intermixed in exposures of a broad kilometre-scale shear zone (Figure 3.5) that also contains serpentinite, potentially derived from the mantle wedge (Chapter 6). Foliation generally strikes north-south and dips east, and lineation plunges to the east (Fig. 3.5d). At a scale of tens of meters, foliation and lineation wrap around more competent lithologies (Fig. 3.5c), giving rise to considerable scatter in the fabric orientation data. At Yukinoura, $\sim$ 8 km across-strike from the studied exposures, microdiamonds in metapelite, and garnet-bearing metabasalts with possible psuedomorphs after lawsonite, suggest metamorphism at P $>$ 2.8 GPa, before retrogression to epidote-blueschist facies/amphibolite facies equilibria (Nishiyama *et al.*, 2020). The exhumation mechanism for the very high-pressure indicators is not clear. In contrast to Yukinoura, the NMR exposures at the Mie and Nishikashiyama localities considered in this study do not preserve signs of retrogression from such high pressures, so it is unclear whether the 2.8 GPa pressure constraint is also applicable. The preserved structures and mineralogy in the studied exposures imply non-coaxial shear with shear sense consistent with subduction at epidote-blueschist facies conditions.

3.3 Application as an analogue for active-margin processes

Tectonic reconstructions indicate that in the Late Cretaceous, young to moderately aged oceanic lithosphere subducted northwards along the NE-SW striking Eurasian margin (Muller *et al.*, 2008; Whittaker *et al.*, 2007). The kinematics of Late Cretaceous subduction are consistent with the top to south shear inferred for the Makimine mélange and the NMR (Section 4.4). On this basis, we interpret these three shear zone exposures to have experienced progressive deformation along a similar, NE-SW striking subduction thrust (Figure 3.6) accommodating subduction of young to moderately aged, relatively warm and buoyant lithosphere. Together, this series of exposures gives a depth-integrated geological view of the megathrust below the 300 °C isotherm, extending to ∼500 °C near the mantle-wedge corner, along a subduction zone with a relatively warm (see Section 4.7) paleo-geotherm. This T range contains the ETS source regions along the relatively warm Cascadia (McCrory *et al.*, 2014; Wech and Creager, 2011) and SW Japan margins (Obara and Kato, 2016; Obara *et al.*, 2010).

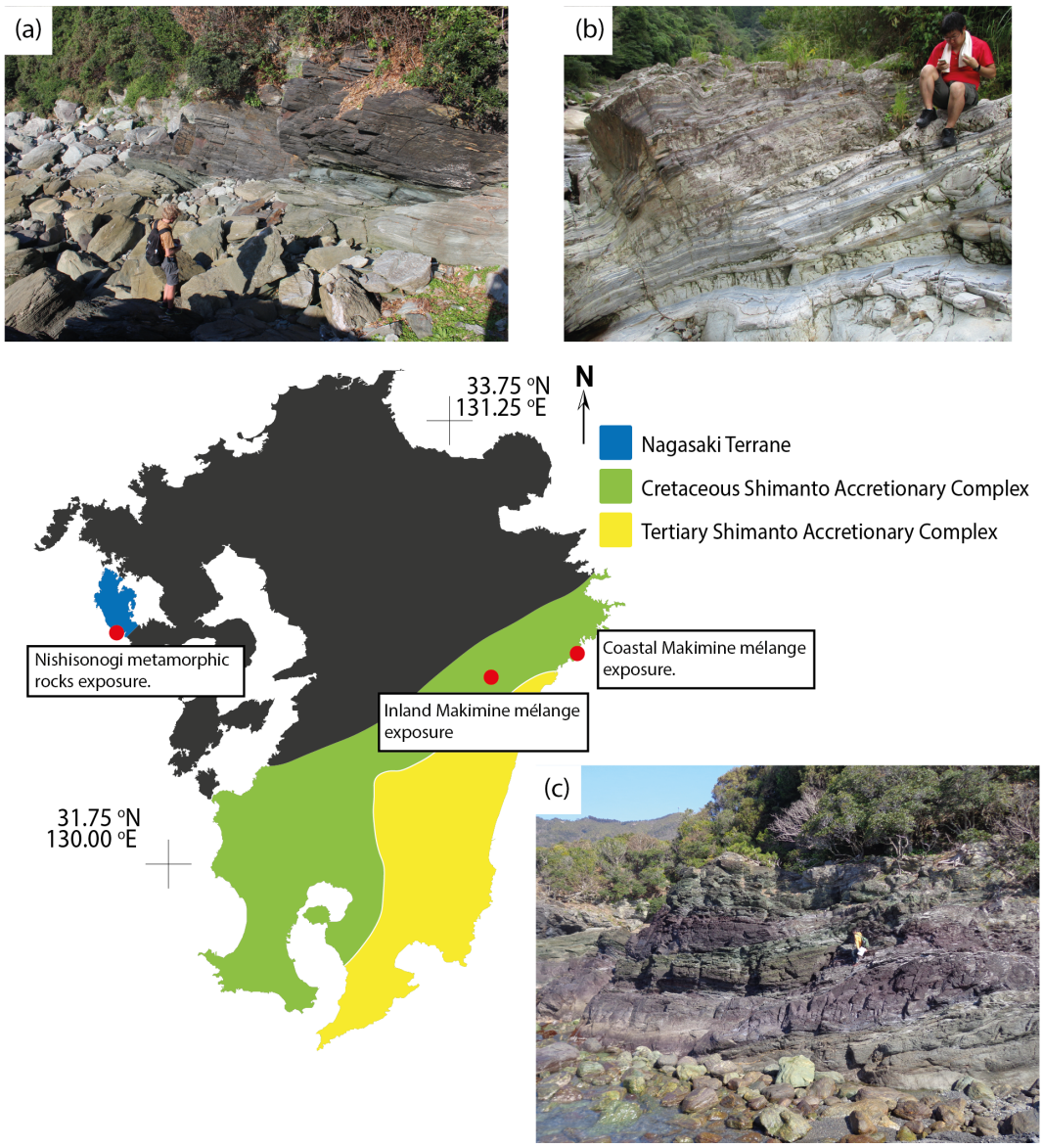

Figure 3.2: Map of Kyushu, showing the Cretaceous and Tertiary sections of the Shimanto Accretionary Complex, and the Nagasaki Metamorphic Rocks. Red circles show the location of the studied exposures. (a) Photograph of Nishisonogi Metamorphic rocks at the Nishikashiyama locality. (b) Photograph of inland Makimine mélange. (c) Photograph of coastal Makimine mélange. In (a), (b) and (c) reddish grey rocks are metasediments, and light green rocks are metabasalts.

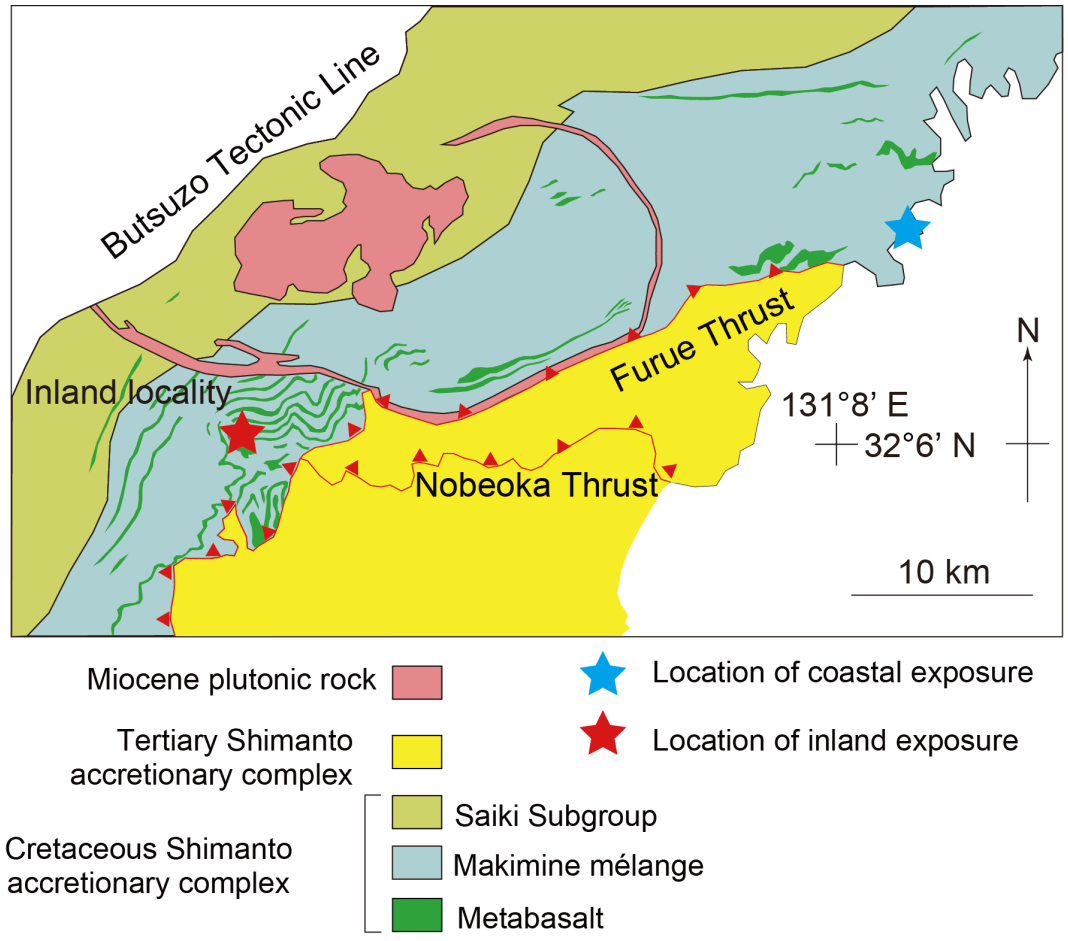

Figure 3.3: Geological map (modified from Murata, 1997) showing the distribution of the Makimine mélange within the Shimanto Acccretionary Complex in eastern Kyushu. Coloured stars show the location of the studied localities.

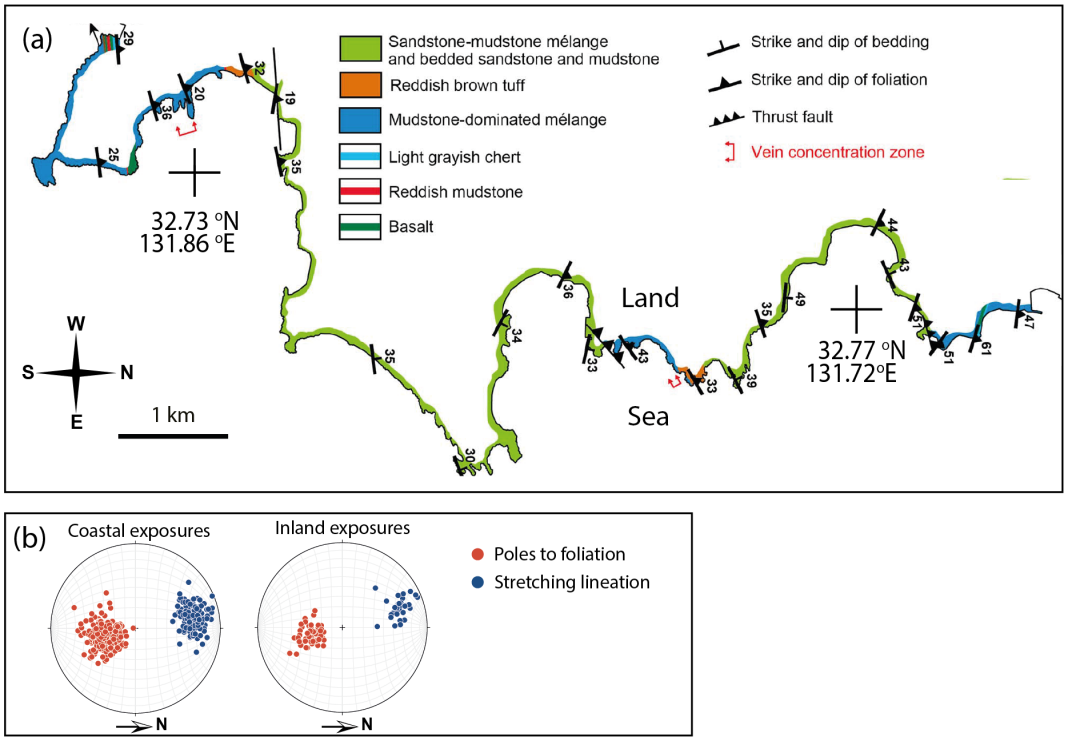

Figure 3.4: Geological map of and structural measurements from the studied coastal exposures of the Makimine mélange in the Shimanto Accretionary Complex. (a) Geological map of coastal Makimine mélange, modified from Ujiie *et al.* (2018) (note north is to the right). (b) Lower hemisphere, equal area stereoplots showing the orientation of foliation and stretching lineation in the coastal exposure shown in (a), and the inland exposure. North is to the right.

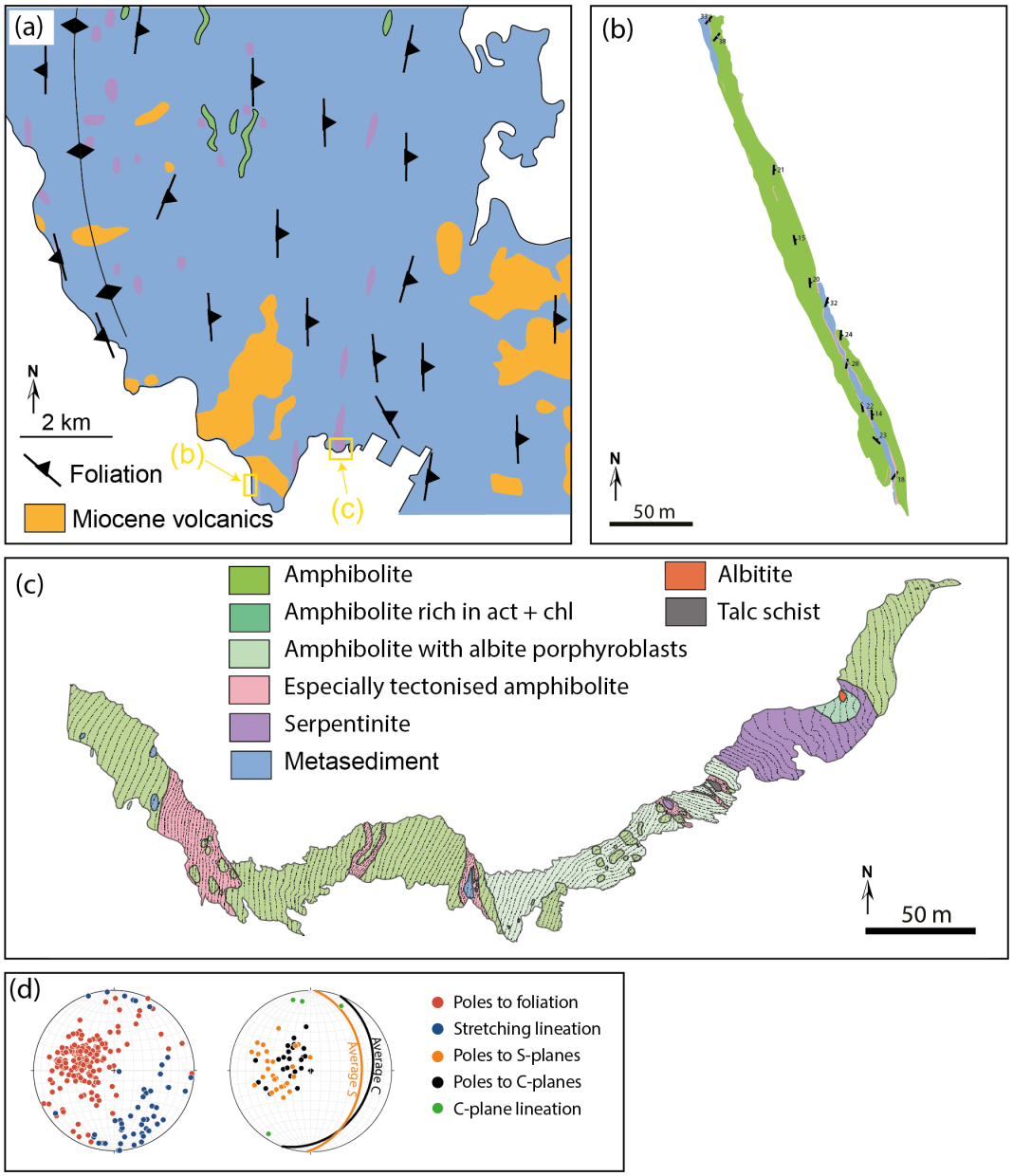

Figure 3.5: Geological maps of and structural measurements from exposures of the Nishisonogi metamorphic rocks in the Nagasaki Terrane. (a) Geological map of the Nishisonogi metamorphic rocks showing the location of maps in (b) and (c), adapted from Nishiyama *et al.* (2017), with Late Cretaceous lithologies colored as in (c). (b) Geological map of the Nishisonogi metamorphic rocks exposed near Nishikasiyama, lithologies coloured as in (c). (c) Geological map of the Nishisonogi metamorphic rocks exposed near Mie. Thin dashed lines indicate foliation traces. (d) Lower hemisphere, equal area sterioplots showing the orientation of bulk foliation, bulk stretching lineation, S and C planes, and C-plane lineation.

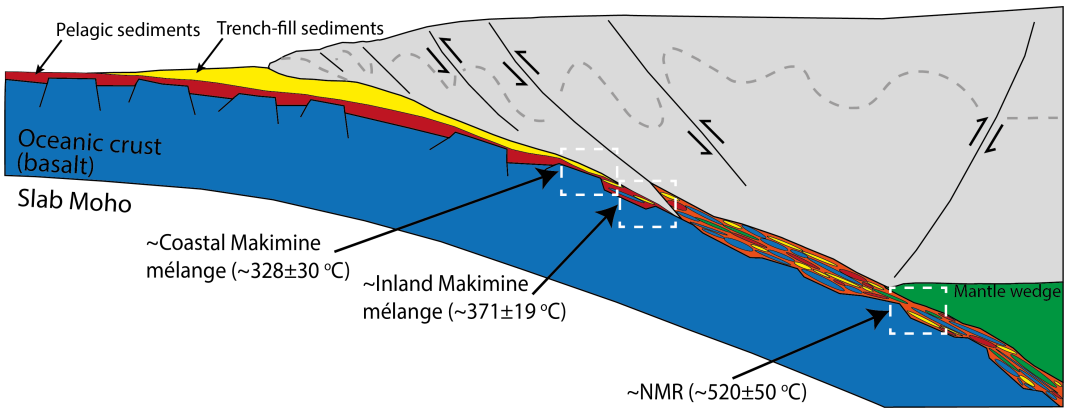

Figure 3.6: Schematic cross section of a subduction zone, showing the approximate setting of shear zone exposures prior to exhumation.

Chapter 4

Embrittlement within ductile shear zones across the base of the seismogenic zone

4.1 Abstract

Geophysical observations indicate that diverse slip behaviour occurs over a depth range down-dip of the subduction thrust seismogenic zone. Observation and modelling suggest that effective stresses are low and fluids play a key role in deformation. The effects of fluids during the mixed frictional-viscous deformation expected in this depth range is, however, still unclear. To address where and how conditions of low effective stress arise, and their effects on deformation style, we examined three exposures of exhumed plate interface shear zones on Kyushu, SW Japan. These exposures represent a down-dip transect along the plate interface at conditions similar to the regions where diverse slip behaviour occurs along warm modern convergent margins.

For an oceanic crust composition from one of the studied shear zones, mineral equilibrium modelling indicates that aqueous fluid is released in discrete temperature-dependent pulses corresponding to the breakdown of specific hydrous minerals. Notably, shear zone exposures that preserve mixed brittle-ductile behaviour deformed at temperature conditions $\sim 328 \pm 30$ °C and $\sim 500 \pm 50$ °C, near those of localised dehydration reactions. In contrast, exposures exhumed from intermediate metamorphic grades, away from ongoing dehydration reactions, deformed by dominantly ductile flow. We propose that

fluid supplied by localised dehydration reactions locally raises pore fluid pressure, creating patches of especially reduced effective stress within the subduction thrust, allowing mixed brittle-ductile deformation to occur at conditions where viscous flow would otherwise dominate. In heterogeneous shear zone exposures that preserve mixed brittle-ductile behaviour, the brittlely-formed veins are especially frequent near contacts between lithologies, suggesting that shear stress gradients along these contacts also contribute to embrittlement.

We conclude that the mineralogy, hydration state, and P-T path of subducting oceanic lithosphere controls the rate and location of fluid release, influencing the location of patches where effective stresses are especially low, allowing mixed brittle-ductile behaviour by a combination of fluid pressurisation and stress gradients along mechanical contrasts.

4.2 Introduction

Earthquakes and aseismic sliding are now understood to be end-members of a spectrum of fault slip styles on plate boundary fault systems (Section 2.8; Obara and Kato, 2016; Peng and Gomberg, 2010). In most locations, earthquakes nucleate within a depth range referred to as the seismogenic zone, below which deformation is dominantly aseismic. However, the transition zone between seismogenic and aseismic depths is home to a range of intermediate slip styles, and whether it can host earthquake propagation is important for understanding the possible range of earthquake magnitudes (e.g., Marone, 1998; Scholz, 1998). For example, some subduction megathrusts host episodic tremor and slow slip (ETS) between the base of the seismogenic zone and the mantle wedge corner (Obara, 2002; Rogers and Dragert, 2003; Schwartz and Rokosky, 2007), and the potential for earthquake propagation in this ETS zone remains unclear (Obara and Kato, 2016). Seismic signals suggest that tremor contains swarms of thrust-sense low-frequency shear slip events (LFEs) along the plate interface (Ide *et al.*, 2007; Shelly *et al.*, 2006), commonly but not always associated with aseismic, geodetically detected, strain rate transients known as slow slip events (SSEs) (Obara and Kato, 2016; Wallace, 2020). However, the physical mechanisms responsible for these intermediate slip styles remain uncertain (Behr and Bürgmann, 2021; Bürgmann, 2018; Kirkpatrick *et al.*, 2021). To better understand the mechanisms controlling fault slip styles, direct ge-

ological constraints are needed on deformation structures in transition zones between seismogenic and aseismic regions, and the mineral-scale mechanisms that accommodate deformation.

Here, we consider three exposures of subduction thrust shear zones exhumed from different P and T conditions on a similar, Late Cretaceous margin, outlined in Chapter 3. Structures within each of the studied shear zones record a history of mutually overprinting foliations and quartz veins, suggesting cyclicity in rheology, permeability, and fluid pressure during dominantly ductile deformation, as also observed in many other exhumed shear zones (e.g., Fagereng *et al.*, 2018; Fisher *et al.*, 1995; Kotowski and Behr, 2019; Meneghini and Moore, 2007; Rowe *et al.*, 2011). Changes in the deformed mineral assemblages between different P-T conditions caused the release of fluid along the prograde metamorphic path, potentially coinciding with changes in rheology (Condit *et al.*, 2020; Fagereng *et al.*, 2018; Peacock, 2009).

We describe the distribution of brittlely and ductilely developed structures and interpret the physical mechanisms responsible for deformation, to address the following questions: (1) Does the proportion of brittle and ductile deformation change between shear zones deformed at different metamorphic conditions? (2) What physical processes drive brittle and ductile deformation, and what factors (e.g., P, T, effective stress, deviatoric stress, fluid availability) determine the dominant deformation style; (3) how might these factors vary within the region between the base of the seismogenic zone and the mantle wedge corner?

4.3 Methods

We examined and sampled deformed sediments, oceanic crust, and quartz veins at three localities of exhumed shear zones on Kyushu, SW Japan. A combination of light and scanning electron microscopy was used to determine the petrography and microstructure of each sample. Electron microscope work was conducted using the Zeiss Sigma HD scanning electron microscope in the School of Earth and Environmental Sciences, Cardiff University. Data derived from energy dispersive spectra (EDS) were acquired using a 10 keV beam and a beam current of $\sim$4 nA.

Electron backscatter diffraction (EBSD) data were collected using a 20 keV

beam and a beam current of ∼4.3 nA. Raw data were collected at a step-size of 5 micron. The MTEX toolbox for MATLAB (Bachmann *et al.*, 2010, 2011) was used to process the data. The ebsd data cleanup routine is described briefly below, (for further detail refer to Bachmann *et al.*, 2010, 2011).

1. Construct grains
2. Remove datapoints that produce 1-pixel grains
3. Re-construct grains

Where indexinthe distribution of quartz c-axesg was especially poor, an additional 3 steps were preformed:

1. Calculate the fraction of the total pixels within the grain that were successfully indexed
2. For grains where $> 70\%$ pixels are indexed, extrapolate to fill the missing pixels.
3. Remove grains with $< 70\%$ indexed pixels

Quartz veins were sampled for stable isotope analyses, and samples were chosen of veins that cross-cut foliations defined by the peak metamorphic assemblage at each site, but were also themselves ductilely deformed with a subduction-related sense of shear. Analyses of quartz vein $\delta^{18}O$ were performed at the University of Cape Town following the laser fluorination method of Harris and Vogeli (2010). 2-3 mg of clean quartz chips, picked manually under a binocular microscope, were reacted with BrF_5 and collected as O_2. The isotope ratio of the O_2 gas was measured with a Finnegan Mat DeltaXP mass spectrometer in the Department of Archeology at the University of Cape Town. Raw data were converted to δ-notation relative to standard mean ocean water (SMOW) based on an internal garnet standard (MON GT; $\delta^{18}O = 5.38‰$). Long-term variations in the measured $\delta^{18}O$ of standards indicate standard deviation of $0.15‰$.

To improve estimates of the P-T conditions of deformation, and estimate amounts and conditions of fluid release in P-T space, stable mineral assemblages were calculated for the composition of a metabasalt sample from inland

Makimine mélange (Table 4.1). Calculations were completed in the Na_2O-CaO-K_2O-FeO-MgO-Al_2O_3-SiO_2-H_2O-TiO_2-O (NCKFMASHTO) chemical system using the program THERMOCALC version 3.45 and an updated version of the Holland and Powell (2011) thermodynamic dataset 6.2 (updated Monday 6 Feb, 2012). Calculations used the activity-composition relationships of Green *et al.* (2016), apart from the relations for prehnite and pumpellyite, which are from Holland and Powell (2011). Calculations at temperatures below 350 °C used a simplified version of the amphibole model that only considered Fe-Mg substation in ideal actinolite. The analysed composition of the metabasalt was converted to the ideal chemical system by disregarding minor amounts of Cr and Mn that cannot currently be accounted for in the activity-composition relations. C in the bulk composition relates to minor calcite within ductilely deformed veins, and was also excluded from the calculations. However, in order to account for Ca in calcite, the stoichiometric amount of Ca required to form calcite from the available C was subtracted from the total Ca. Similarly, Phosphorus was not considered in the calculations, but the stoichiometric amount of Ca required to form apatite was also subtracted from total Ca. 25% of total Fe was taken to be Fe^{3+}, in line with typical values for metamorphosed mafic rocks (c.f. the compilation in Rebay *et al.*, 2010), and the sample was assumed to be fluid-saturated at all conditions.

4.4 Tectonic fabrics in the exhumed shear zones

In coastal exposures of the Makimine mélange, foliation in metabasalt and metasediment strikes east-west, and dips gently to the north (Fig. 3.4) (Ujiie *et al.*, 2018). Sandstone and metabasalt occur as relatively competent, lenticular blocks in the mudstone matrix (Fig. 4.1a, b), and block long axes have a common orientation subparallel to the foliation dip. Foliation in the mudstone and metabasalt is locally cut by quartz veins that occur in two sets, sub-parallel and at high angles to the foliation (Fig. 4.1c), and in en-echelon tensile gash shear zones (Fig. 4.1d) (Ujiie *et al.*, 2018).

In inland exposures of the Makimine mélange, schistose sediments and metabasalts are interlayered, with layer thickness on the order of centimetres to several meters (Fig. 4.2a). Metabasalt occurs as layers with subtle pinch-and-swell geometry within metasediment (Fig 4.2a), suggesting that metabasalt

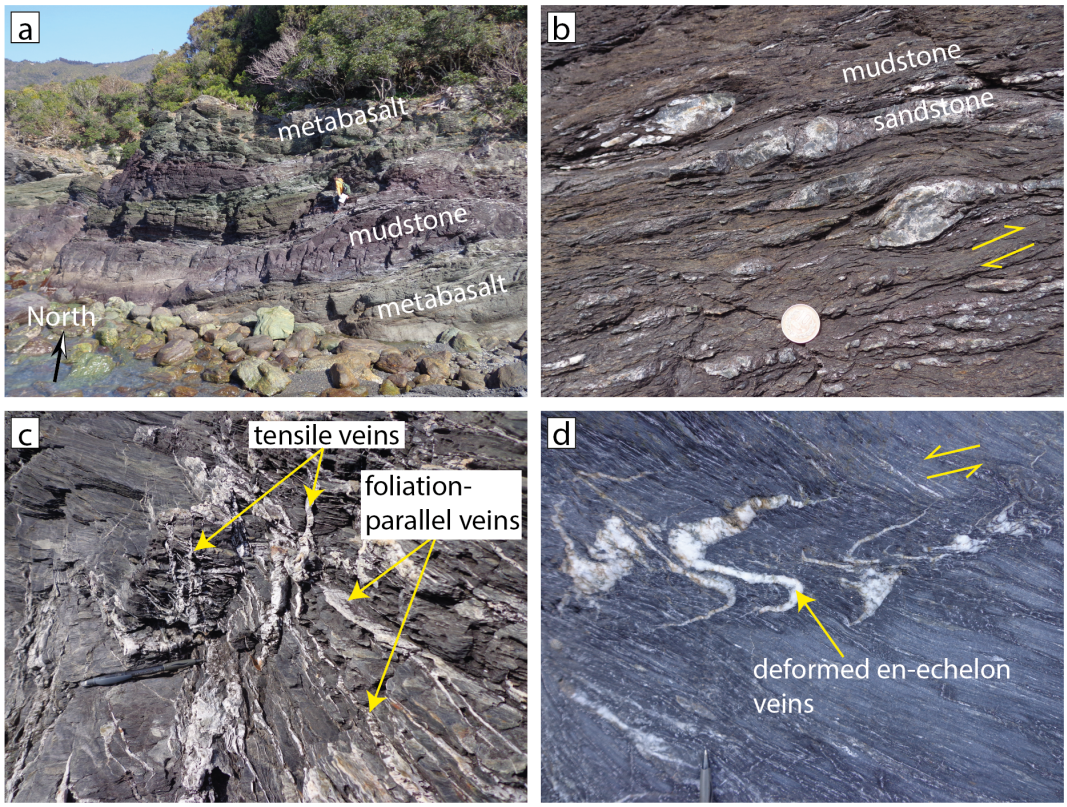

Figure 4.1: Structures within coastal exposures of the Makimine mélange: (a) Layers of greenish metabasalt intercalated with mudstone. (b) Sigmoidal lenses of quartzofeldspathic sandstone within mudstone, viewed approximately parallel to foliation dip. (c) Vertical tensile veins orthogonal to foliation, mutually cross-cut by foliation-parallel shear veins and tensile veins. (d) En-echelon veins ductilely deformed within mudstone.

	wt % oxide	Normalised molar oxide %	Adjusted molar oxide %
Si	48.81	53.40	53.40
Ti	1.20	0.99	0.99
Al	15.44	9.96	9.96
Fe	10.71	8.82	8.82
Mn	0.18	∼	∼
Mg	7.41	12.09	12.09
Ca	9.11	10.68	9.49
Na	3.52	3.74	3.74
K	0.24	0.17	0.17
P	0.12	∼	∼
H	2.67	∼	∼
C	0.76	∼	∼
Total	100.19	∼	∼

Table 4.1: XRF data in oxide weight percent, and conversion to molar oxide % for input to THERMOCALC.

was slightly more viscous at the conditions of deformation. Both lithologies have developed a penetrative foliation dipping gently north, similar to the foliation in coastal mélange exposures (Fig. 2.12). Stretching lineation is subparallel to foliation dip, as in coastal mélange exposures (Fig. 3.4b). Quartz veins occur within these exposures, although here, in contrast to the coastal exposures, veins are subparallel to the foliation and show pinch-and-swell to boudinage structure (Fig. 4.2b), indicating fracture and vein precipitation was followed by a substantial ductile deformation that consistently overprinted the brittle deformation phase and transposed the veins and the foliation.

Intermixed metasedimentary and amphibolite (metabasalt) schists, and serpentinite of the NMR have foliation generally dipping gently to the east (Fig. 3.5d), and lineation plunging gently to the south-south-east, features interpreted to be affected by post-subduction regional folding with a north-south trending fold hinge (shown in Fig. 3.5a). Foliation in metasediment and amphibolite schists curve throughout the exposure, with especially tight folding occurring near lithological contacts (Fig. 4.3a) Restoring the foliation to horizontal, S-C foliation geometries and lineation on C planes show a top-to-south

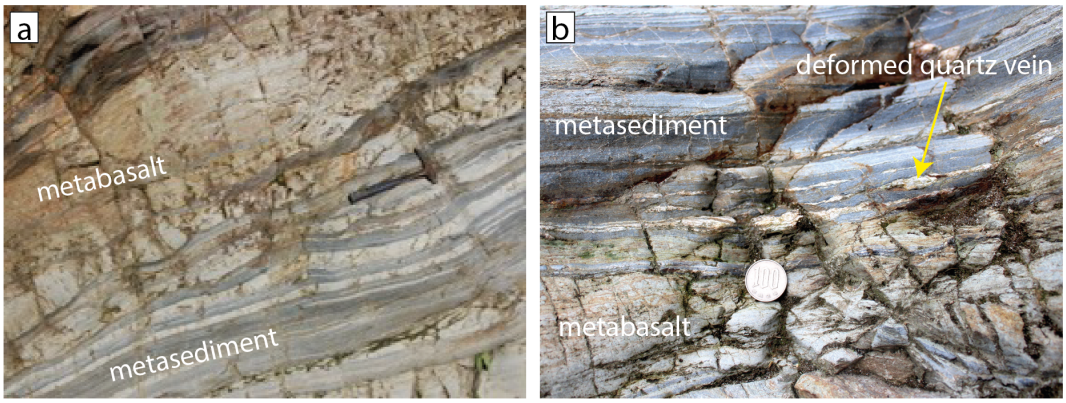

Figure 4.2: Structures within inland exposures of the Makimine mélange: (a) Layers of greenish metabasalt with pinch-and-swell structure, separated by metasediment. (b) Ductilely deformed veins within metasediment, close to a metabasalt-metasediment contact.

shear sense comparable to exposures of the Makimine mélange. Quartz veins appear throughout the shear zone exposure, both subparallel to the foliation and cross-cutting it at oblique angles (Fig. 4.3c, d).

Tectonic reconstructions indicate that in the Late Cretaceous, young to moderately aged oceanic lithosphere subducted northwards along the NE-SW striking Eurasian margin (Muller *et al.*, 2008; Whittaker *et al.*, 2007). The kinematics of Late Cretaceous subduction are consistent with the top-to-south shear inferred for the Makimine mélange and the NMR. On this basis, we interpret these three shear zone exposures to have experienced progressive deformation along a similar, NE-SW striking subduction thrust, accommodating subduction of young to moderately aged, relatively warm lithosphere.

4.5 Quartz veins within the shear zones

In coastal exposures of the Makimine mélange, shear veins occur subparallel to the mudstone cleavage (Fig. 4.1c) and are identified by quartz slickenfibers on vein surfaces, and crack-seal textures indicating opening at dilatational stepovers (Ujiie *et al.*, 2018). Extension veins, parallel and oblique to the foliation (Fig. 4.1c) are identified by vein-normal opening vectors; for example, the extension vein quartz shows euhedral grains with long-axes orthogonal to the vein boundaries (Ujiie *et al.*, 2018). Together the extension and shear veins form a pervasive fault-fracture mesh that accommodates a combination of dilation and thrust-sense shear, as described for a general case by Sibson

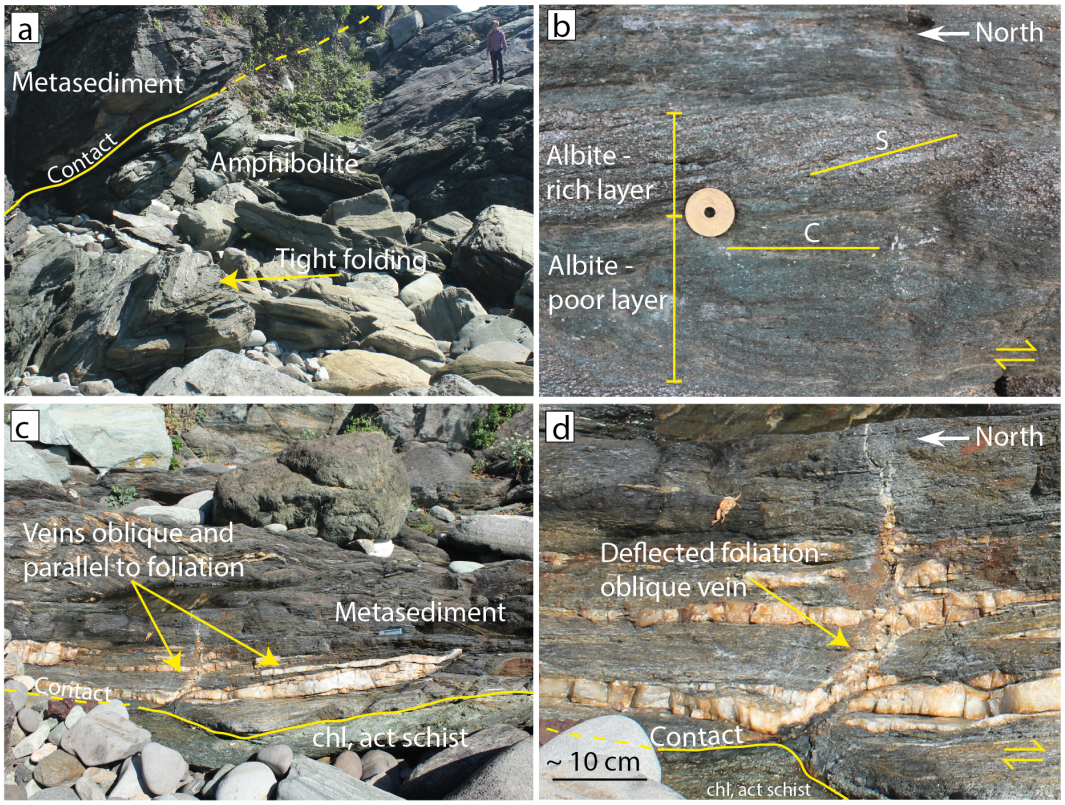

Figure 4.3: Structures within the NMR exposure, with inferred shear sense in (b) and (d) indicated by opposing arrows: (a) Exposure showing tight folding in amphibolite near a contact with metasediment. (b) S-C foliation geometry within amphibolite consistent with top-to-south shear. (c) Cluster of foliation-parallel and foliation-orthogonal veins along the contact between chlorite-actinolite schist and metasediment. (d) Close-up of veins in (c), showing a foliation-orthogonal vein deflected towards the foliation near a contact with chlorite-actinolite schist.

(1996, 2017). The thickness of these veins varies from a few mm to ∼5 cm, with typical lengths 1-2 m, although locally up to ∼10 m and limited by ourop size. Areas of concentrated veining occur within the mudstone-dominated mélange unit (Fig. 3.4a) and are inferred to be zones that experienced locally elevated strain rates (Ujiie *et al.*, 2018). The quartz veins have been ductilely deformed within localised, en-echelon shear zones (Fig. 4.1d).

In inland exposures of the Makimine mélange, veins are sub-parallel to foliation and have pinch-and-swell structure indicating ductile deformation (Fig. 4.2b). Unlike in coastal mélange exposures, vein morphologies are less clear in outcrop, and vein quartz lacks growth-related microstructures (e.g. fluid-inclusion planes, euhedral grains). Vein widths vary between a few centimetres and a few hundred microns. Vein lengths range between sub-mm lenses (Fig. 4.5b), interpreted as dismembered veins, and more intact examples with lengths up to ∼2 m.

In the NMR, although veins are dominantly sub-parallel to foliation, a substantial proportion of veins crosscut the foliation (Fig. 4.3c, d). Veins subparallel to the foliation show pinch-and-swell to boudinage structure, and veins cross-cutting foliation are commonly deflected along foliation planes (Fig. 4.3d). These observations indicate that fracture and vein precipitation was consistently followed by ductile deformation, although along many veins the ductile strain is small, and the veins cross-cut foliations defined by the peak metamorphic assemblage. The thickness of veins varies from $\sim$ 1 mm to $\sim$ 30 cm and veins range in length from $\sim$ 1 m to at least 5 m, but the maximum traced length is limited by the outcrop size. Near amphibolite-metasediment contacts the frequency of veins is especially high relative to the general frequency of veins in the study area (Fig. 4.3c), possibly caused by local pore space generation and H_2O and SiO_2 release during metasomatic reactions (Ujiie *et al.*, 2021).

4.6 Ductile fabrics within the shear zones

In metabasalts of the coastal Makimine mélange, chlorite-rich well-foliated domains separate less chloritic, relatively albite-rich sigmoidal lenses (Fig. 4.4a, b). Albite-rich lenses in metabasalt are elongate parallel to the long axes of sandstone lenses in metasediment, and the chloritic cleavage is especially well

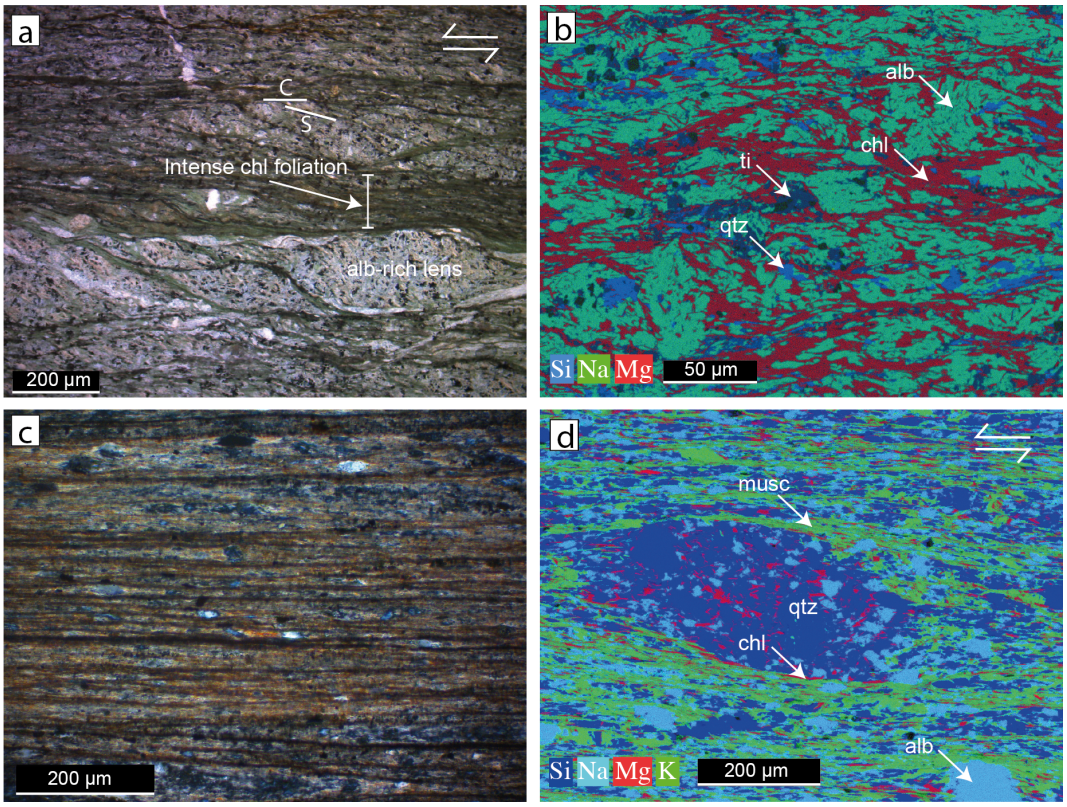

Figure 4.4: Micro-scale appearance of metabasalt (a, b) and metasediment (c, d) from coastal Makimine mélange. Opposing arrows in (a) and (d) show the inferred shear sense. (a) Photomicrograph of metabasalt showing S-C structure. Albite-rich lenses containing S-surfaces are separated by darker, relatively chloritic layers defining C-surfaces. (b) EDS element map highlighting the distribution of chlorite around albite and quartz in metabasalt. (c) Photomicrograph of metasediment showing the well-developed cleavage, with interstitial quartz grains elongate parallel to the cleavage. (d) EDS element map of metasediment, showing the muscovite-defined cleavage rotated adjacent to a quartz grain.

developed adjacent to these lenses (Fig. 4.4a). Within metasediment, cleavage surfaces are defined by layers of fine-grained muscovite, which separate phyllosilicate-poor quartzofeldspathic domains (Fig. 4.4c). The cleavage spacing in metasediment is generally in the range 10-100 μm, with tighter spacing adjacent to large quartz or albite grains (Fig 4.4d). Large grains and aggregates of quartz and albite in both metabasalt and metasediment commonly have sigmoidal shape.

In inland Makimine mélange, within metabasalt, aligned muscovite and chlorite define the foliation. Elongate and aligned grains of clinopyroxene, albite and amphibole define the stretching lineation (Fig. 4.5a). There are no indications of dislocation creep microstructures such as subgrains or bulging

grain boundaries in clinopyroxene or albite. Actinolite occurs in asymmetric strain shadows next to clinopyroxene grains, and appears to have formed by the breakdown of clinopyroxene (Fig. 4.5a). In metasediment, layers of fine-grained muscovite define the foliation (Fig. 4.5c), which is especially well developed adjacent to quartzite lenses, which define the stretching lineation in metasediment (Fig. 4.5b). Quartzite veins and lenses consist of large grains with undulose optical extinction, surrounded by smaller grains with straight optical extinction and relatively straight grain boundaries; a microstructure indicating dynamic recrystallisation by subgrain rotation (Stipp *et al.*, 2002). In places, grain boundaries also show bulging geometries, indicating a component of bulging recrystallisation (Stipp *et al.*, 2002). c-axis pole figures for quartz grains in quartzite lenses show a well-developed crossed girdle pattern consistent with top-to-south dislocation creep in quartzite (Fig. 4.5d).

In Chapter 5 a quartz recrystallised grain-size piezometer is used to estimate differential stresses in the range 87-187 MPa for quartzite layers within metasediment. c-axis pole figures for quartz grains within a quartz-rich area of the quartz+albite+muscovite+chlorite matrix show a similar, but much less distinct crossed-girdle structure (Fig. 4.5d).

In the NMR, in amphibolite, aligned elongate grains of albite and amphibole define the stretching lineation, and aligned muscovite, chlorite and actinolite define the foliation, which commonly shows S-C style geometry (Fig. 4.6a). In metasediment, muscovite defines the foliation, and the long axes of albite and quartz grains define the stretching lineation (Fig. 4.6b). Quartz veins parallel to the foliation in amphibolite and metasediment are characterised by low degrees of intragranular distortion and lobate grain boundaries (Fig. 4.6b), suggesting dynamic recrystallisation by grain boundary migration (Stipp *et al.*, 2002). Differential stresses for quartzite in amphibolite, estimated by quartz recrystallised grain-size piezometry, indicate differential stresses in the range 21-60 MPa (Chapter 5).

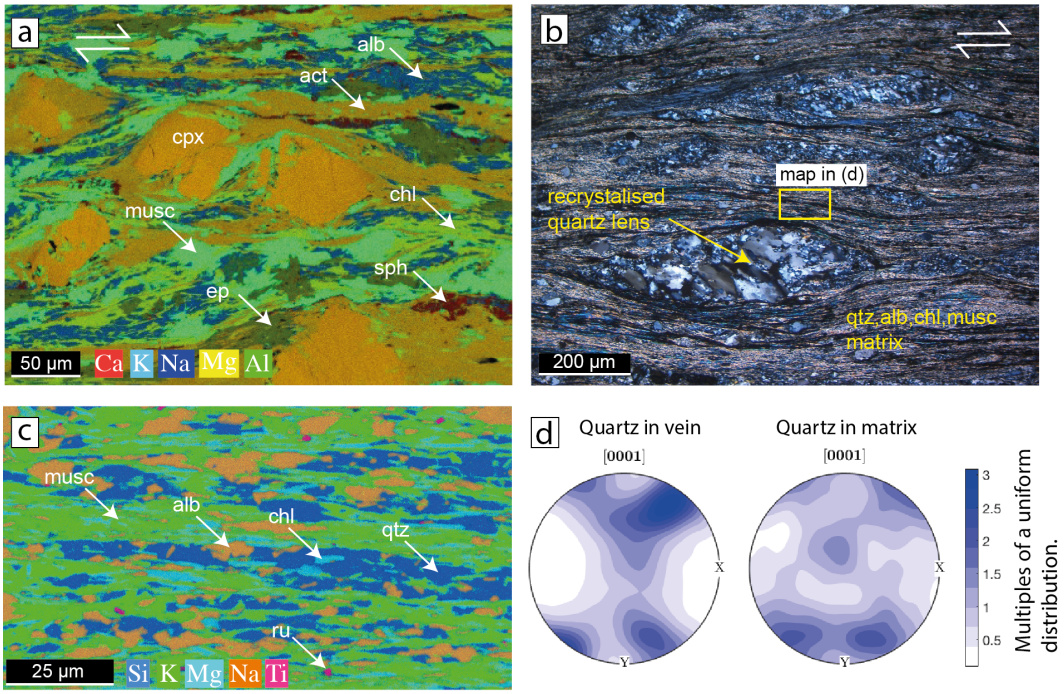

Figure 4.5: Micro-scale appearance of metabasalt (a) and metasediment (b, c) from inland Makimine mélange, and stereoplots showing quartz grain orientations in metasediment (d). Opposing arrows in (a) and (b) show the inferred shear sense. (a) EDS element map showing the muscovite and chlorite-defined foliation enveloping clinopyroxene and albite grains. Actinolite occurs as asymmetric rims around clinopyroxene. (b) Photomicrograph of metasediment showing sigmoidal lenses of dynamically recrystallised quartzite surrounded by a foliated matrix of quartz, albite chlorite and muscovite. (c) EDS element map showing segregated quartz-albite and chlorite-muscovite layers. (d) Equal area, lower hemisphere pole figures showing the distribution of quartz c-axes (one point per grain) in a recrystallised quartz vein (n=3500), and in a quartz-rich area of the quartz, albite chlorite and muscovite matrix (n=1000).

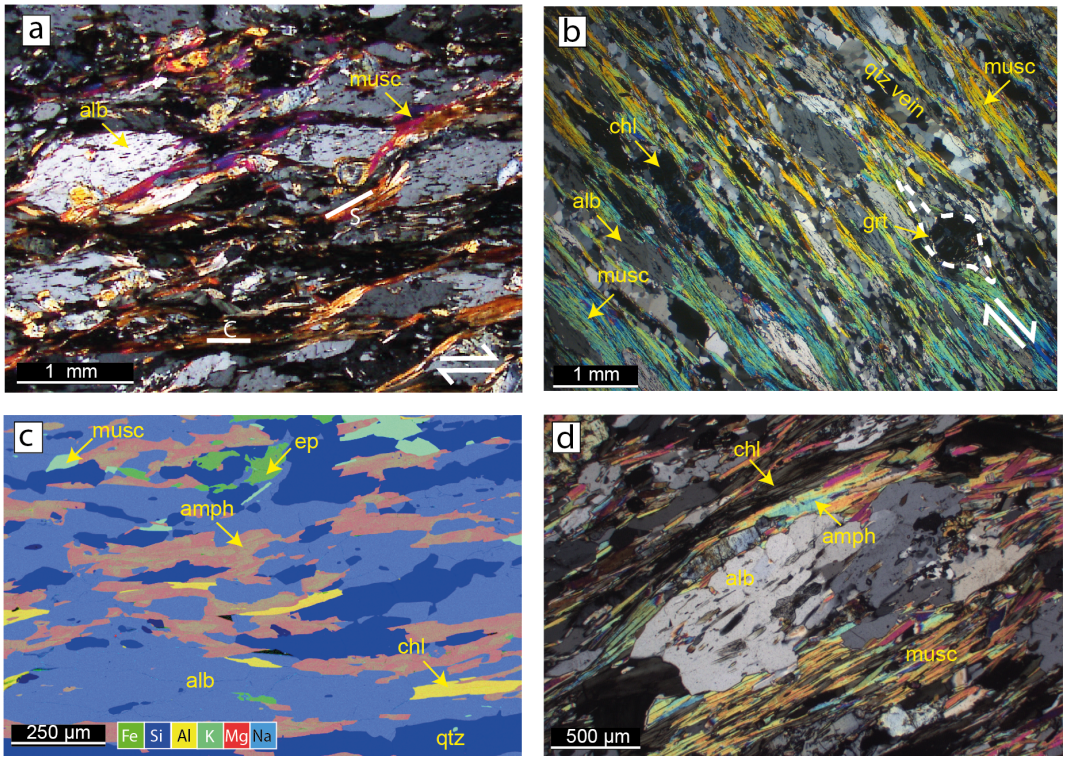

Figure 4.6: Microscale appearance of amphibolite and metasediment from the NMR. (a) Photomicrograph of amphibolite showing albite grains wrapped by muscovite, with S-C foliation geometry. (b) Photomicrograph of metasediment showing well-aligned muscovite separating layers of quartz and albite, and wrapping around garnet. Quartz precipitated in sigmoidal strain shadows adjacent to garnet grains indicates non-coaxial shear. Inferred shear sense indicated by opposing arrows (bottom right, panels a and b). (c) EDS element map of amphibolite. Albite shows no chemical zonation, but amphibole has pronounced zoning with a more aluminous, hornblende-like composition in cores, and a less aluminous, more actinolite-like composition in the rims. (d) Photomicrograph of amphibolite, showing muscovite, chlorite and amphibole wrapping around albite.

4.7 Mineral assemblages, thermodynamic equilibria and metamorphic dehydration reactions

The metamorphic conditions of the studied shear zones suggest burial to far greater depths than the few kilometres where substantial fluid-bearing porosity is expected to be maintained (e.g., Ellis *et al.*, 2015; Saffer and Tobin, 2011; Sun *et al.*, 2020). The main source of fluids at the conditions of the exhumed shear zones is therefore expected to be mineral-bound aqueous fluid released during metamorphic dehydration (Peacock, 1990), and therefore fluid production depends on the petrography and hydration state of the subducting oceanic lithosphere. In most cases, the oceanic crust will be volumetrically more significant than the sediment (e.g., Condit *et al.*, 2020; Peacock, 1990), and we therefore focus on fluid production from basalt protoliths.

Thermodynamically stable mineral assemblages calculated for an inland Makimine mélange metabasalt composition (Table 4.1), assuming water saturation, are shown in a P-T pseudosection in Fig. 4.7a. At pressures below 600 MPa, and temperatures <260 °C, equilibria contain the typical prehnite-pumpellyite facies assemblage of actinolite-chlorite-albite-prehnite-pumpellyite-quartz-titanite. With increasing temperature, a series of phase changes occur over the narrow T-window 260-300 °C, notably the loss of prehnite and pumpellyite in exchange for actinolite and epidote (Fig. 4.7a). This series of changes represents a transition from the prehnite-pumpellyite facies to the greenschist facies. The broad T window between 300-450 °C, at P<800 MPa, contains the typical greenschist facies assemblage actinolite-epidote-biotite-chlorite-albite-quartz-titanite (Fig. 4.7a).

Increasing temperature in the range 450-475 °C, at P<800 MPa, results in further phase changes, notably the loss of actinolite, then chlorite, both in exchange for hornblende (Fig. 4.7a) This series of changes represents a transition from the greenschist facies to the amphibolite facies. In the high-pressure, low temperature corner of the diagram, lawsonite-blueschist facies equilibria appear at P<900 MPa and T 350-450 °C. From within lawsonite-blueschist facies equilibria, increasing temperature results in the loss of Na-diopside and lawsonite, in exchange for actinolite and epidote.

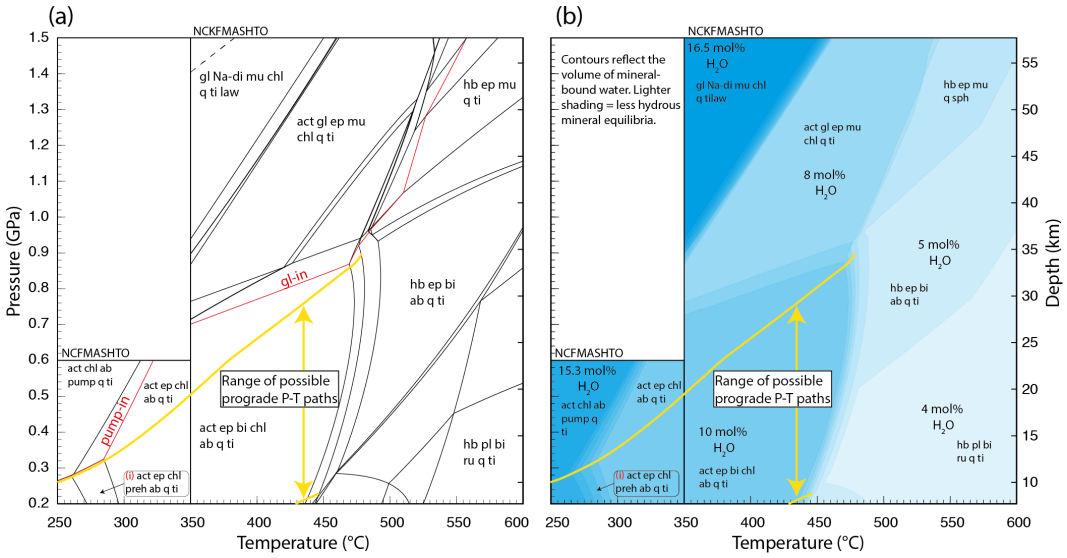

Figure 4.7: Mineral equilibria and mineral-bound water content calculated for the composition of a metabasalt sample from inland Makimine mélange. (a) Model equilibria overlain with the inferred P-T path for the studied Late Cretaceous margin. Solid lines indicate the position of equilibria boundaries, and the dashed line marks the distinction between nominal Na-diopside and nominal omphacite. (b) Contours showing volume fractions of mineral-bound water for the equilibria in (a).

In coastal Makimine mélange, where the peak metamorphic T is estimated to be 328 ± 30 °C (Ujiie *et al.*, 2018) metabasalt contains albite, chlorite, epidote, quartz, titanite, magnetite and minor prehnite. Peak pressure for this locality is currently unconstrained, however, this metabasalt mineral assemblage is broadly consistent with the equilibria (i) in Fig. 4.7a. Actinolite is not seen in thin section, but the model assemblage (i) is calculated to contain only a minor proportion of actinolite (∼10 vol. %).

At the slightly higher metamorphic conditions experienced by the rocks exposed in the inland Makimine mélange (peak T estimate 371 ± 30 °C; Ujiie *et al.*, 2021), metabasalt contains albite, quartz, chlorite, muscovite, epidote, actinolite, and clinopyroxene. EDS element maps show that clinopyroxene is partially replaced by actinolite formed in asymmetric strain shadows (Fig 4.5a), implying progressive but partial equilibration of the metabasalt during ductile deformation. Metamorphic clinopyroxene does not stabilise until far greater metamorphic grades, so clinopyroxene in this sample is considered to have an igneous origin.

The lack of prehnite and hornblende in inland Makimine metabasalt is consistent with peak thermal metamorphism between prehnite breakdown, oc-

curring over the T range 280-330 °C, and the actinolite-hornblende transition occurring over the range 450-475 °C. These constraints are consistent with the RSCM metamorphic temperature estimate (371 ± 30 °C). Assuming peak metamorphic temperature of 371 ± 30 °C, the lack of glaucophane suggests inland Makimine mélange experienced peak pressures <700 MPa (Fig. 4.7).

NMR amphibolite contains amphibole with hornblende cores surrounded by isometric actinolite rims (Fig. 4.6c). Isometric actinolite rims suggest largely static conditions during the actinolite-forming phase. Fig. 4.7a shows that hornblende is replaced by actinolite along a retrograde metamorphic path between 450 °C and 500 °C, over the P range 200 MPa to 1 GPa. Assuming peak thermal metamorphism at 500 °C, the lack of glaucophane in NMR amphibolite suggests peak pressures <11 GPa.

Contrast to metabasalts, metasediments from the studied exposures show only minor mineralogical changes within increasing metamorphic grade. Coastal Makimine and inland Makimine mélange metasediments show the same mineral assemblage; quartz, albite, muscovite, and chlorite. NMR metasediments show minor (∼5%) garnet in addition to the Makimine mélange mineral assemblage.

The constraints on peak pressure and temperature provided by metabasalt mineralogy, as described so far in this section, supported by RSCM thermometry, suggest the three shear zone exposures experienced a P-T path that tracked pressures below those required for pumpellyite and glaucophane stability. Phase boundaries below pumpellyite-in and glaucophane-in reactions are largely dependent on temperature, and relatively insensitive to pressure (Fig. 4.7a), preventing an estimate of the minimum metamorphic pressure by comparison of sample mineralogy with the model mineralogy in Fig. 4.7a. In the case of coastal Makimine mélange, phase boundary topology does not change substantially until P < 200 MPa. Peak metamorphism at ∼330 °C and 200 MPa, would reflect an exceptionally high thermal gradient for subduction (∼43 °C/km), so phase relations below 200 MPa are unlikely to be relevant to the shear zones studied here.

Between P > 200 MPa, and P where pumpellyite and glaucophane are stabilised in a hydrated basalt composition, progressive subduction leading to increased metamorphic temperatures drives phase changes that dramatically reduce the amount of mineral-bound water. Fig. 4.7b reflects the equilibria

in Fig. 4.7a contoured for the amount of mineral-bound water. Over the P-T windows 250-350 °C and 200-600 MPa, and 350-600 °C and 200 MPa to 1.5 GPa, aqueous fluid is released in three discrete pulses relating to the breakdown of prehnite and pumpellyite at 260-300 °C and <600 MPa, lawsonite at 300-500 °C and >900 MPa, and chlorite at 450-500 °C over the entire pressure range.

Within the range of possible P-T paths indicated in Fig. 4.7, prograde metamorphism from within the prehnite-pumpellyite facies (corresponding to T<∼270 °C) results in prehnite breakdown in metabasalt close to the conditions of coastal Makimine mélange (Fig. 4.7a), resulting in the release of ∼5 mol% H_2O between ∼270 °C and 290 °C (Fig. 4.7b). In contrast to the coastal Makimine mélange exposures, the large area of the diagram occupied by the greenschist facies, and containing the peak metamorphic conditions of inland Makimine mélange exposures, experiences no substantial change in the mineral-bound water content (Fig. 4.7b). The highest metamorphic grade exposure, the NMR, occurs within a region of chlorite breakdown (Fig. 4.7a) which releases another 5 mol% H_2O between 470 °C and 490 °C (Fig. 4.7b). The modelled fluid release is expected to occur at similar temperatures for the wide range of thermal gradients that track pressures between 200 MPa and below the maximum pressures constrained by the pumpellyite-in and glaucophane-in phase boundaries (Fig 4.7b).

4.8 δ^{18}O in quartz veins

Oxygen stable isotope ratios were measured on 4 veins in mudstone-dominated mélange within the coastal exposure of the Makimine mélange, 2 veins in metasediment from the inland exposure of the Makimine mélange, and 8 veins in metasediment, amphibolite, and chlorite-actinolite schist from the NMR (Table 4.2). Across all three shear zone exposures, δ^{18}O values in vein quartz vary between 15.0 and 17.9‰ (Fig. 4.8), with the highest values measured in samples from the prehnite-actinolite facies coastal Makimine mélange (peak T $\sim 328 \pm 30$ °C) and lowest values measured in samples from the epidote-blueschist facies NMR (peak T $\sim 500 \pm 50$ °C). Quartz vein δ^{18}O for all the studied exposures are comparable to other quartz vein δ^{18}O in values measured in subduction related complexes, such as the blueschist, greenschist and

amphibolite units of the Catalina Schist, southern California, where vein $\delta^{18}O$ values are between 14.4 and 17.4‰ (Bebout, 1991), and the amphibolite facies Kuiseb Schist, within the Namibian Damara belt, where vein $\delta^{18}O$ values are between 9.4 and 17.9‰ (Fagereng *et al.*, 2018).

Sample	Exposure	°N	°E	Note	Host rock	Description	Quartz δ^{18}O	Fluid δ^{18}O
SC-08	Makimine-coastal	32.72702	131.86035	From intensely foliated zone	Mudstone	Foliation parallel vein	17.9	12
SC-10	Makimine -coastal	32.72702	131.86035		Mudstone	Tensile vein, normal to foliation	17.5	11.5
SC-09	Makimine -coastal	32.72702	131.86035		Mudstone	Shear vein, laminated and slightly undulating	17.3	11.4
SC-04	Makimine -coastal	32.72702	131.86035		Mudstone	Tensile vein - sigmoidal. Sheared top-to-south in normal sense shear zone	16.8	10.9
SC-18	Makimine -inland	32.61285	131.45122		Metasediment	Foliation-parallel vein with subtle lineation on vein surface.	15.8	-
SC-19	Makimine -inland	32.61103	131.44772		Metasediment	Chips of foliation-parallel veins with pinch-and-swell structure	15.8	-
SC-28	NMR	32.81218	129.73251		High strain amphibolite	Foliation-parallel vein boudinaged in chlorite-actinolite schist	16.1	13.9
SC-40	NMR	32.81218	129.73251		High strain amphibolite	Boudinaged foliation-parallel vein	16.1	13.8
SC-32	NMR	32.81218	129.73251		Metasediment	Chips of foliation-parallel vein	15.7	13.4
SC-29	NMR	32.81218	129.73251		High strain amphibolite	Boudinaged foliation-parallel vein	15.5	13.2
SC-25	NMR	32.81218	129.73251		Amphibolite	Foliation parallel vein, slightly sigmoidal. Shear sense: top-to-south	15.4	13.2
SC-24	NMR	32.81218	129.73251		Amphibolite	Foliation-parallel vein	15.3	13
SC-42	NMR	32.81218	129.73251	Approx. 50 m east of GPS point	Amphibolite	Vein folded within the foliation	15.0	12.8
SC-41	NMR	32.81218	129.73251	Approx. 100 m east of GPS point	Amphibolite	Explosive, brecciated, quartz dominated veins cross-cutting foliation	15.0	12.7

Table 4.2: Quartz vein descriptions, and δ^{18}O measurements. Fluid δ^{18}O calculated following Matsuhisa *et al.* (1979), assuming precipitation at the peak metamorphic temperature of the coastal Makimine mélange and the NMR.

We calculate δ^{18}O of the vein-forming fluid for veins in the coastal Makimine mélange and in the NMR using temperature-dependent water-quartz fractionation factors (Matsuhisa *et al.*, 1979). In these shear zones, the sampled veins cross-cut the peak metamorphic foliation, but are also ductilely deformed and inferred to have precipitated at approximately peak metamorphic temperatures. Calculated fluid δ^{18}O values are between 10.9 and 12‰ for coastal Makimine mélange veins, and between 12.7 and 13.9‰ for the NMR veins (Fig. 4.8). Calculated fluid δ^{18}O is similar to the fluid δ^{18}O of 12 ± 1‰ calculated for vein-forming fluids in the amphibolite facies Kuiseb Schist, and fluid δ^{18}O of 13 ± 1‰ calculated for vein-forming fluids in the blueschist to amphibolite-facies units of the Catalina Schist (Bebout, 1991). These values are at the low end of values for subducted clastic sediments (δ^{18}O 10-20‰; Savin and Epstein, 1970), but greater than expected for fluids in equilibrium with oceanic crust (δ^{18}O < 8‰; Muehlenbachs, 1986; Stakes and Taylor, 1992), or mantle rocks (δ^{18}O ~ 5.5‰; Mattey *et al.*, 1994).

4.9 Inferred mechanisms of ductile creep across the base of the subduction thrust

4.9.1 Ductile creep at < 350 °C

Rocks in the coastal Makimine mélange were deformed at 328 ± 30 °C (Ujiie *et al.*, 2018) and both metasediments and metabasalts have well-developed cleavage (Fig. 4.4). Photomicrographs and element maps show that the foliation is defined by discrete, laterally continuous layers rich in aligned chlorite in metabasalt, and aligned muscovite and chlorite in metasediment. Intense mechanical anisotropy in phyllosilicate minerals (Hansen *et al.*, 2020; Mares and Kronenberg, 1993; Okamoto *et al.*, 2019) cause mechanically weak phyllosilicate cleavage planes to be parallel to the XY plane of the finite strain ellipsoid defined by the principal stretches X≥Y≥Z (Fig. 4.9). The alignment of relatively insoluble phyllosilicates can be facilitated by pressure solution creep of interspersed, relatively soluble non-phyllosilicates (e.g. quartz, albite) (Gratier, 1987; Weyl, 1959), a phenomenon where normal stress acting on grain surfaces enhances the local rate of dissolution. Gradients in grain boundary normal stress result in solubility gradients, driving elongation of grains in di-

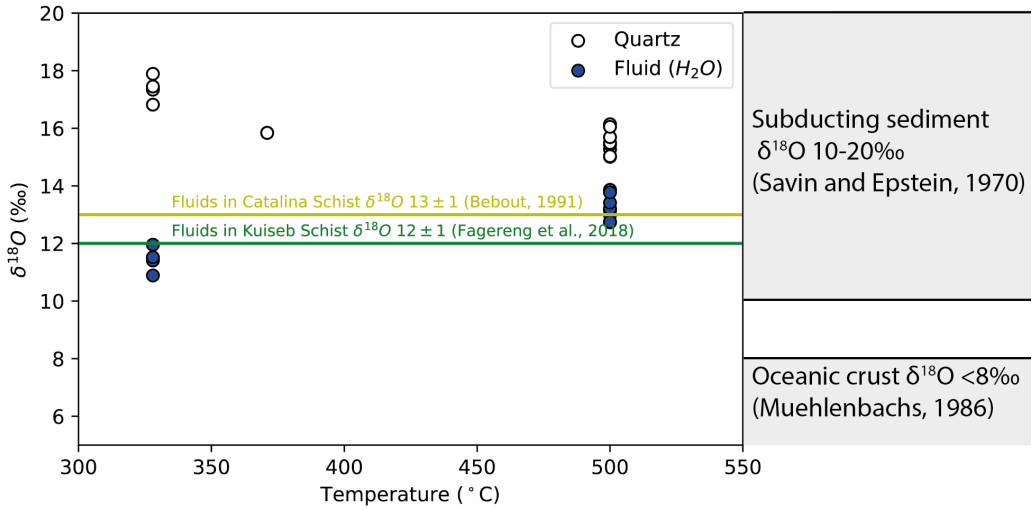

Figure 4.8: δ^{18}O of vein quartz for each of the localities, and for localities where veins precipitated at close to the final subduction-related strain, δ^{18}O of the vein-forming fluid, calculated for peak metamorphic temperature of the locality. Vein-forming fluids have δ^{18}O low within the range of δ^{18}O for subducting sediment presented in Savin and Epstein (1970), and higher than the δ^{18}O of oceanic crust Muehlenbachs (1986).

rections reflecting the local orientation of the greatest principal stretch, X (Fig. 4.9). In non-phyllosilicate minerals (e.g. quartz, albite) the rate of pressure solution is enhanced where phyllosilicates occur along grain boundaries (Gratier *et al.*, 2015; Greene *et al.*, 2009; Renard *et al.*, 1997; Weyl, 1959), assisting the progressive development of discrete phyllosilicate-rich layers such as those within metapelite and metabasalt in coastal Makimine mélange (Fig. 4.4).

Sigmoidal patterns of silica concentration adjacent to large quartz grains (Fig. 4.4d), are interpreted to reflect areas of relatively higher and lower normal stresses during non-coaxial shear, respectively enhancing and impeding the rate of pressure solution (Durney, 1976; Rutter, 1983). The phyllosilicate cleavage in metabasalt and metasediment in coastal Makimine mélange, although formed initially perpendicular to σ_1, is expected to have rotated toward the regional shear zone boundary during progressive non-coaxial strain (Fig. 4.9). Overall, the ductile fabrics in metasediments and metabasalts from coastal Makimine mélange exposures are interpreted to have formed during non-coaxial shear facilitated by pressure-solution creep of quartz and albite and sliding along mechanically weak chlorite and muscovite cleavages inclined to the direction of σ_1 (Fagereng and Sibson, 2010; Niemeijer and Spiers, 2005).

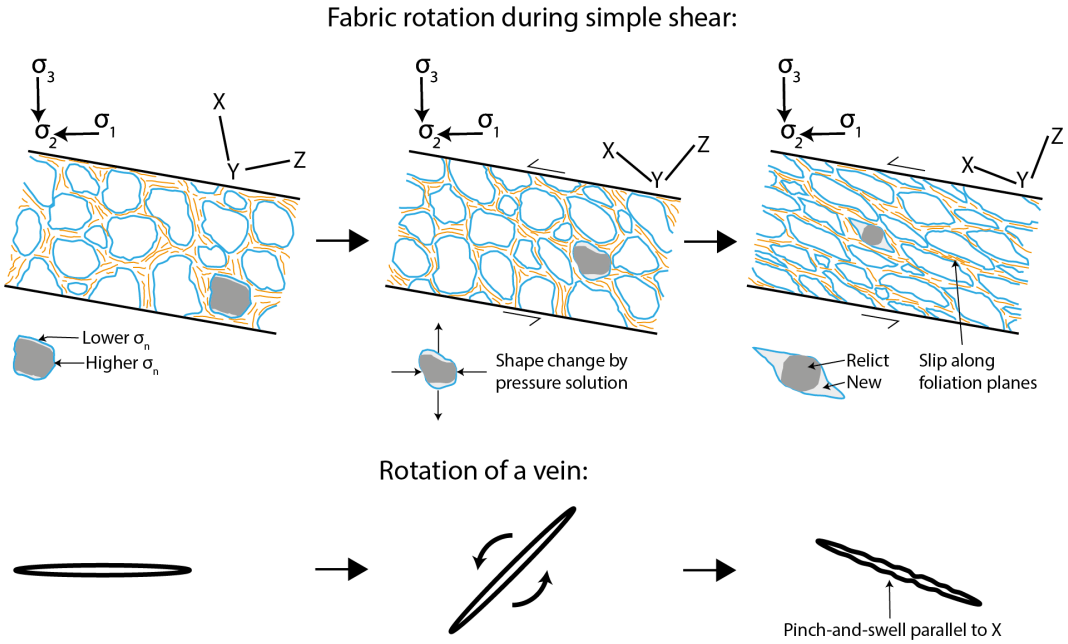

Figure 4.9: Schematic diagram showing progressive development of foliation and lineation fabrics in a gently dipping simple shear zone at low angles to σ_1. Pressure-solution creep of soluble minerals (blue), results in elongation of grains parallel to σ_3, defining the initial orientation of the greatest principal stretch X of the finite strain ellipsoid. Foliation and lineation track finite strain, rotating with progressive strain towards the shear zone boundary. Quartz veins, initially formed orthogonal to σ_3, also rotate with progressive strain.

In this case, the rheology controlling ductile shear is a frictional-viscous flow (Bos and Spiers, 2002; Niemeijer, 2018; Niemeijer and Spiers, 2005) sensitive to grain-size, mineral solubility, frictional strength, effective stress, and strain rate.

4.9.2 Ductile creep at > 350 °C

The well-developed muscovite cleavage in metasediments from inland exposures of the Makimine mélange (peak metamorphic temperature $\sim 371 \pm 30$ °C; Ujiie *et al.*, 2021) is interpreted to have formed by local dissolution and precipitation of quartz and albite, like in coastal mélange exposures. Variation in the intensity of the cleavage next to quartzite clasts (Fig. 4.5b) is interpreted to reflect areas of relatively higher and lower normal stresses during non-coaxial shear (Durney, 1976; Rutter, 1983). Pronounced quartz crystal preferred orientation (CPO) patterns in quartzite, and less pronounced CPO patterns in mixed-mineralogy, fine-grained metasediments (Fig. 4.5d) suggests dissolution-precipitation creep is more efficient than dislocation creep in fine grained, mixed-mineral rocks, as also inferred from theoretical studies (Wheeler, 1992), and observations in some continental shear zones (e.g., Kilian *et al.*, 2011; Stenvall *et al.*, 2019).

In metabasalts from inland Makimine mélange, shape-preferred orientations and lack of intracrystalline deformation in clinopyroxene and albite suggest that these minerals deformed by local dissolution and precipitation involving pressure solution. The sigmoidal shape of actinolite-clinopyroxene clasts (Fig. 4.5a) indicate that the clinopyroxene breakdown reaction occurred during non-coaxial shear (e.g. Fig. 4.9). The foliation, defined by muscovite and chlorite, curves around the clinopyroxene grains and likely forms mechanically weak horizons where shear strain localises. Like in coastal Makimine mélange, ductile fabrics in inland Makimine mélange are interpreted to have formed during non-coaxial shear by dissolution and precipitation of mechanically strong quartz, albite, and clinopyroxene, coupled to sliding along mechanically weak cleavages inclined to the direction of σ_1 (Fig. 4.9).

In metasediments from the NMR (peak metamorphic temperature $\sim 500 \pm 50$ °C; Ujiie *et al.*, 2021), laterally continuous layers of aligned muscovite define the foliation, and are separated by quartz and albite. Quartz grains in deformed veins have undulose optical extinction consistent with dislocation

creep (Stipp *et al.*, 2002). Lobate, inter-fingered grain boundaries (Fig. 4.6b) are indicative of the grain boundary migration recrystallisation mechanism (Stipp *et al.*, 2002). The shape preferred orientation of albite grains, and lack of intracrystalline distortion indicated by straight optical extinction (Fig. 4.6a) suggests albite deformed by pressure solution creep.

NMR metasediment, which is dominated by quartz and muscovite, contains boudinaged quartz veins deformed by dislocation creep (Fig. 4.3d). This geometry suggests quartz is stronger than muscovite-quartz aggregates, highlighting the mechanical importance of phyllosilicates in metasediment. At 500 ± 50 °C, and at a strain rate of 10^{-12}s^{-1}, as inferred for the NMR (Chapter 5), the muscovite rheology of Mares and Kronenberg (1993) (cast in power-law form by Bukovská *et al.*, 2016) gives differential stresses of ~ 7 MPa. At the same conditions, quartz undergoing dislocation creep deforms at differential stresses between 19 and 45 MPa (Hirth *et al.*, 2001) (water fugacity calculated as in Shinevar *et al.*, 2015). Therefore, at the temperature and strain rate inferred for the NMR, quartz deforming by dislocation creep is at least twice as strong as muscovite, consistent with the boudinaged quartz veins. Towards lower temperatures (e.g. in the Makimine mélange), or higher strain rates, laboratory flow laws (Hirth *et al.*, 2001; Mares and Kronenberg, 1993) indicate quartz undergoing dislocation creep becomes progressively stronger than muscovite.

In amphibolite, aligned muscovite and chlorite define the foliation, and elongate albite and amphibole grains define the lineation (Fig. 4.6a). Albite has straight optical extinction and displays no clear CPO (Fig. 5.3). Despite displaying a well-developed shape preferred orientation (SPO) (Fig. 4.6a) the grain size of the albite grains (~ 1 mm) is prohibitively large for efficient diffusion creep (Rybacki and Dresen, 2004). As a result, much of the deformation in metabasalt is inferred to have occurred by sliding along foliation planes defined by aligned chlorite and muscovite.

The rock fabrics preserved in metasediments and hydrated metabasalts exposed in all three of the studied shear zones indicate that ductile deformation was driven by local dissolution-precipitation and sliding along foliations that contain aligned mechanically weak phyllosilicates. This is similar to previous models for fault slip at low shear stresses (e.g., Fagereng and Sibson, 2010; Niemeijer and Spiers, 2005). In metasediment, at T $>$ 350 °C, volumetrically minor quartzite layers showing dislocation creep microstructure indicate

a small contribution of this mechanism to the overall strain. Dissolution-precipitation creep and sliding along foliation surfaces (Fig. 4.9) persists as the dominant mechanism in metasediments and hydrated basalts over entire range in P and T conditions recorded by the studied exposures. Similar microstructures have been observed in subduction thrust shear zones exhumed from temperatures < 300 °C (e.g., Fagereng and Diener, 2011; Meneghini and Moore, 2007; Palazzin *et al.*, 2016), and at comparable conditions to the studied shear zones (French *et al.*, 2019; Platt *et al.*, 2018; Wassmann and Stöckhert, 2013), and also at warmer conditions in continental crust (Condit and Mahan, 2018). Particularly in phyllosilicate-poor lithologies (e.g., clay-poor sediments, partially hydrated oceanic crust), the interconnected phyllosilicates likely host a substantial portion of the total strain. Numerical and phenomenological models (e.g., Gardner *et al.*, 2017; Handy, 1990) and laboratory experiments ,(e.g., Holyoke and Tullis, 2006) indicate that small ($\sim< 10\%$) portions of a weak phase (e.g., a phyllosilicate mineral) are sufficient to allow substantial strain localisation, such that the strength and rheology of phyllosilicates may contribute substantially to the strength and rheology of the plate interface.

4.10 Brittle deformation within the ductile shear zones

Quartz veins in coastal Makimine mélange are relatively undeformed, implying vein formation occurred towards the end of subduction-related deformation. Mutually cross-cutting shear and tensile veins suggest that the shear and extension fracturing events forming the fault-fracture mesh were coeval (Ujiie *et al.*, 2018). The stress and fluid pressure conditions during formation of this vein network, and the veins in the other shear zones, can be explored with a brittle failure mode diagram (Cox, 2010; Sibson, 1998) plotted for Andersonian stress regimes with vertical σ_1 or σ_3 (Fig. 4.10). The failure envelopes in Fig. 4.10 show stress conditions for tensile, tensile-shear, and shear failure in effective stress-differential stress space for rocks with friction coefficients (μ) of 0.4 and 0.6, tensile strength (T_0) 5 and 10 MPa, and cohesive strengths $= 2T_0$. This range of material parameters is broadly representative of metasediments (Lockner, 1995) and likely comparable to phyllosilicate-rich altered basalts, which are the dominant lithologies in the studied shear zones.

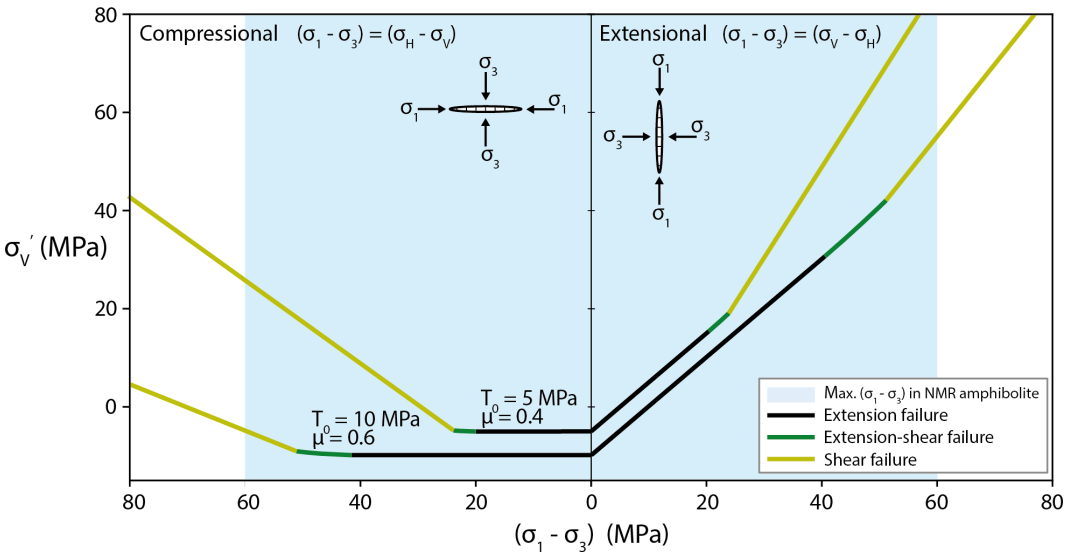

Figure 4.10: Composite brittle failure envelopes (following Sibson, 1998), coloured for failure mode, showing failure conditions in effective vertical stress - differential stress space. The blue rectangle shows the possible range of differential stresses in NMR amphibolite, constrained in chapter 5. Envelopes constructed assuming tensile strength, T_0 = 10 MPa and internal friction $\mu_i = 0.6$, and T_0 = 5 MPa, and $\mu_i = 0.4$. The plot illustrates how increasing differential stress or reducing effective vertical stress (increasing pore fluid pressure) promotes brittle failure.

In stress states favouring reverse and normal faulting, the formation of tensile veins is restricted to differential stress conditions $(\sigma_1 - \sigma_3) < 4T_0$ (Fig. 4.10 and Section 2.3). Micaceous metasediments similar to those in coastal Makimine mélange show T_0 generally in the range 5-10 MPa (e.g., Gholami and Rasouli, 2014), suggesting differential stress conditions in coastal Makimine mélange of less than a few tens of MPa at the time of tensile fracturing. Shear veins in coastal Makimine mélange, formed by hybrid tensile-shear fracturing (Ujiie *et al.*, 2018), require slightly higher differential stress (Fig. 4.10), but still in the order of tens of MPa. Subhorizontal extension veins subparallel to foliation, mutually crosscut by subvertical extension veins, imply local and/or temporary rotation of σ_3 from vertical to horizontal (Fig. 2.4) reflecting switching between stress states favouring reverse and normal faulting in coastal Makimine mélange (Ujiie *et al.*, 2018). Such switching is also consistent with small differential stress, particularly if stress drops are small, as suggested by Ujiie *et al.* (2018). As Fig. 4.10 assumes the shear zone is ideally oriented with respect to the stress field, the plotted failure criteria reflect the minimum differential stress and maximum effective normal stress required to

cause shear or tensile-shear failure (as also demonstrated in Fig. 2.3, section 2.3)

In inland Makimine mélange and the NMR, vein morphology related to their formation (e.g. slickenfibers, euhedral grains) are overprinted by dislocation creep, making the failure mode of the deformed veins unclear in the absence of displacement markers in the host rocks. Veins in inland Makimine mélange are ductilely stretched parallel to the subduction-related foliation, implying vein formation was followed by an dominantly ductile deformation. The veins deformed in inland Makimine mélange may have formed at shallower, cooler conditions, like those determined for the coastal Makimine mélange, before subducting deeper, and deforming in a dominantly ductile part of the subduction thrust.

Veins that cross-cut foliation in the NMR show ductile deformation consistent with the bulk shear (Fig. 4.3d), implying that these veins formed while subduction-related shear-deformation was still occurring. Progressive ductile shear will cause rotation of the late-forming veins towards parallel with the earlier-formed foliation (Fig. 4.9). Accordingly, the veins which crosscut foliation but also show small subduction-related ductile strains, must have formed near the last subduction-related deformation, but prior to exhumation. These observations imply that the NMR records brittle deformation that occurred at greater depths, and was superimposed on greater finite strains, than the ductile deformation recorded in the inland Makimine mélange.

In the NMR, foliations are more closely spaced, lineations are better developed, and veins are more frequent along contacts between metasediment and amphibolite, relative to elsewhere in the exposures. Contrast between the mechanical properties of metasediment and amphibolite will create stress and strain gradients, potentially leading to localisation of deformation and locally increased strain rates (Beall *et al.*, 2019b; Fagereng and Diener, 2011; Sibson, 1980; Tarling *et al.*, 2019; Ujiie *et al.*, 2021). Veins in the NMR are generally thicker than in coastal and inland Makimine mélange, reflecting either an increased frequency of repetitive fracturing and sealing, or that vein opening increments were larger.

The low driving stresses inferred for all of the studied shear zones (Chapter 5; Ujiie *et al.* 2018; Ujiie *et al.* 2021), allows for a mixture of tensile, hybrid tensile-shear, or shear failure, and switching in stress directions, and this

variation of stress directions and fracture modes is more likely at low effective stress (Fig. 4.10). This is consistent with mutually overprinting tensile and hybrid tensile-shear veins preserved in coastal Makimine mélange (Ujiie *et al.*, 2018). In addition to the hybrid tensile-shear veins, shear displacement has likely been accommodated, to unknown finite strains, by sliding along phyllosilicate fabrics, likely at low driving stress allowed by low effective stress and weak frictional resistance (Fig. 4.9). Tectonic tremor signals are generally accepted to reflect low frequency earthquakes (LFEs) accommodating shear slip within the plate interface (e.g., Ide *et al.*, 2007; Ide and Tanaka, 2014; Royer and Bostock, 2014; Shelly *et al.*, 2006), although Frank *et al.* (2014) show that LFEs may not encompass the entire tremor signal. Acoustic emissions during laboratory dehydration experiments are comparable to tremor (Burlini *et al.*, 2009), and dehydration-related tensile fractures perhaps reflect the noisy part of the tremor signal (Fagereng *et al.*, 2018). In this model, tremor consists of a combination of shear slip generating LFEs, driven by local fluctuations in differential stress or effective vertical stress (Fig. 4.10), and tensile fracture, generating the noisy part of the tremor signal, driven by fluctuations in local effective stress (Fig. 4.10) as a result of fluid pressurisation.

That veins formed coeval with ductile creep implies transient switching of rheology, and that driving stresses (and related strain rates), and/or fluid pressure within the subduction thrust were not constant. Geophysical studies have shown that tremor is sensitive to small (1-15 kPa) stress changes induced by earth and ocean tides (Nakata *et al.*, 2008; Royer *et al.*, 2015; Rubinstein *et al.*, 2008; Thomas *et al.*, 2013), indicating stress conditions in ETS regions are close to the critical conditions for brittle failure (Sibson, 2017). In this state, only small stress perturbations are required for a transient switch from steady ductile creep to local fracturing.

Within mixed-lithology shear zones, such as the studied examples, localised stress changes due to mechanical contrasts (e.g., Beall *et al.*, 2019a; Fagereng, 2013) might lead to switching between ductile creep and fracturing. The models presented in Beall *et al.* (2019a) deformed under pore fluid factor of 0.8, and required a large matrix-clast viscosity contrast (10^3) to generate mixed fracturing and creep. Such large viscosity contrasts are inconsistent with our observations of largely continuous tectonic fabrics in the mixed material shear zones which generated mixed fracturing and ductile creep. We suggest that

in the absence of such large viscosity contrasts, patches of effective stresses corresponding to pore fluid factors greater than the 0.8 in the models of Beall *et al.* (2019a), may generate a critically stressed shear zone. Patches of elevated effective stress driven by metabasalt dehydration reactions are likely to act together with metasomatic reactions along lithological contacts which may locally alter mineralogy and viscosity (e.g., Tarling *et al.*, 2019; Ujiie *et al.*, 2021).

4.10.1 Vein-forming fluid volume

If we consider veins as formed by brittle fracture followed by fluid influx and mineral precipitation (Bons *et al.*, 2012; Oliver and Bons, 2001), the quartz veins imply that silica-saturated fluid was present within the shear zones during mixed brittle-ductile deformation in both the coastal Makimine mélange and the NMR.

In coastal Makimine mélange, the fluid pressure is inferred to have cycled, locally, between lithostatic and hydrostatic levels Ujiie *et al.* (2018), with fracturing increasing permeability, thereby rapidly reducing fluid pressure, causing substantial silica supersaturation (Fig. 4.11; Ujiie *et al.*, 2018). Assuming that a fluid pressure drop triggers vein precipitation also in the NMR, we calculate the level of silica supersaturation as the difference between the equilibrium solubility at lithostatic and hydrostatic fluid pressure, at the peak metamorphic temperature of each shear zone, assuming a 15 °C/km thermal gradient. Calculations used the equilibrium solubility expression of Manning (1994) and the Holland and Powell (1991) equation of state for H_2O, as implemented in MATLAB by Fagereng and Ellis (2009). We calculate the total volume of H_2O needed to precipitate a 1 m diameter, 3 cm thick quartz vein, comparable to veins in the studied outcrops. This method calculates the total fluid volume to form a vein, rather than the volume per increment of vein opening. We assume any changes in fluid temperature are negligible, and that the initial level of supersaturation is maintained throughout the history of vein formation (detail in Appendix A). These assumptions lead to a minimum estimate for fluid volume. Calculations using a warmer thermal gradient would also result in larger estimated fluid volumes.

From the assumptions above, the vein-forming fluid in coastal Makimine mélange would, at least initially at the time of a fluid pressure drop, be su-

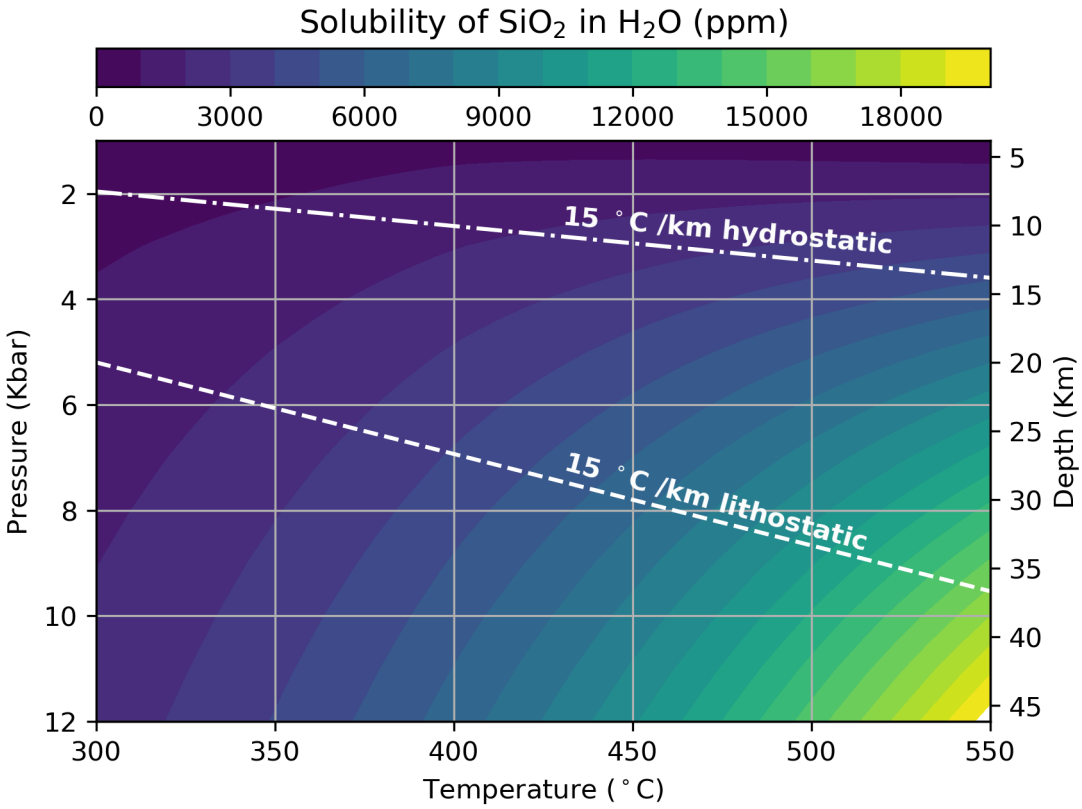

Figure 4.11: Solubility of silica in water as a function of P and T, calculated following Manning (1994) and Holland and Powell (1991) (detail in Appendix A). P-T paths for 15 °C /km lithostatic and hydrostatic pressure gradients are shown for reference.

persaturated with $\sim 0.1\%$ SiO_2. To precipitate a typical 3 cm time-integrated thickness for a 1 m diameter quartz vein from a fluid maintaining 0.1% supersaturated SiO_2 would require $\sim$330 m^3 of fluid at 330 °C. On the other hand, $\sim$50 m^3 of water is required for the same vein volume to precipitate at the approximate temperature of 500 °C experienced by the NMR at time of vein formation. Because we assume the supersaturation is maintained throughout precipitation, this minimum estimate remains the same for veins that form in single or multiple events. The assumptions dictate that the lower required fluid volumes at higher metamorphic grades are an effect of increased silica solubility, and that the assumed pressure drop becomes larger toward higher metamorphic grades. However, assuming a pressure drop equivalent in magnitude to that assumed for coastal Makimine mélange, the required amount of water to form the model vein at 500 ± 50 °C increases only modestly to $\sim$70 m^3.

The lower fluid volume required to form veins at higher metamorphic grades suggests that a lower volume of fluid is required to fill a similar volume fracture at higher temperature, so veins may fill faster, or more completely, potentially preserving thicker veins at higher metamorphic grades.

4.11 Fluid sources along the subduction thrust

Along subduction P-T paths, the oceanic crust composition modelled in Fig. 4.7, and other modelled subducting sediment and hydrated mantle compositions (e.g., Condit *et al.*, 2020; Fagereng and Diener, 2011; Fagereng *et al.*, 2018; Hacker, 2008; Kerrick and Connolly, 2001; Peacock, 2009) release fluids at specific P-T conditions corresponding to dehydration reactions, with substantially lesser volumes of fluid released at P-T conditions between these reactions. The range of potential P-T paths for the studied shear zones passes through two discrete pulses of fluid release from oceanic crust, relating to: (1) prehnite breakdown at 270-290°C releasing 5 mol% H_20, and (2) chlorite breakdown at 470-490°C, releasing another 5 mol% H_20, with (1) occurring at the conditions of coastal Makimine mélange and (2) occurring at the conditions of the NMR (Fig. 4.7). Inland Makimine mélange preserves deformation structures that formed in a thermodynamically stable greenschist facies mineral assemblage at conditions away from ongoing dehydration reactions, and

contains overprinted brittle deformation structures that likely formed at conditions of prehnite breakdown, as preserved in coastal Makimine.

Oxygen stable isotope ratios in vein quartz, and calculated oxygen stable isotope ratios for vein-forming fluids, either indicate a sedimentary fluid source, or represent mantle or crust-derived fluids with δ^{18}O buffered by metasediments, which have relatively high δ^{18}O (Fig. 4.8). In the NMR, where samples of vein quartz were analysed from amphibolite, chlorite-actinolite schist, and metasediments, the trend of increasing vein quartz δ^{18}O between amphibolite, chlorite-actinolite schist, and metasediments suggests some degree of host-rock buffering of vein δ^{18}O. However, vein-forming fluid δ^{18}O values 12.9-13.1‰ in the NMR are higher than expected for fluids in equilibrium with oceanic crust (δ^{18}O < 8‰; Muehlenbachs, 1986; Stakes and Taylor, 1992), or the mantle (δ^{18}O ~ 5.5‰; Mattey *et al.*, 1994).

In contrast to samples of oceanic crust, samples of metasediments have similar mineral assemblages over the range of metamorphic conditions reflected by the studied shear zones. The nearly invariant mineral assemblage suggests that along the inferred P-T path, any changes in the water content of metasediment would be minor, in comparison to changes in the water content of oceanic crust, the petrography of which varies substantially (Fig. 4.7a). Pseudosection models of the average oceanic sediment composition GLOSS (Plank and Langmuir, 1998) support this notion, gradually releasing ∼1.2 mol% H_20 along the P-T path inferred for shear zones studied here (Fagereng *et al.*, 2018).

Mantle and/or oceanic crust-derived fluids (δ^{18}O< 8‰), if present in the shear zones, may have had δ^{18}O buffered by relatively high δ^{18}O metasediments (Fig. 4.8). For coastal Makimine mélange veins, ^{3}He/^{4}He measurements indicate that here a portion of the vein-forming fluid was sourced from serpentinised oceanic mantle or serpentinised mantle wedge (Nishiyama *et al.*, 2020). Measurements of ^{84}Kr/^{36}Ar and ^{130}Xe/^{36}Ar in the veins suggest that the vein-forming fluid was comprised of 80-85% mantle-derived fluid, 15-18% oceanic crust-derived fluid, and the small remainder sourced from dehydrating sediments (Nishiyama *et al.*, 2020). These results support the concept of mantle and crust-derived fluids having had δ^{18}O buffered by metasediments, and suggest that fluids travel up-dip from conditions of serpentinite dehydration ($\sim$ 600 °C; Ulmer and Trommsdorff, 1995) to the conditions of coastal Makimine mélange exposures ($\sim 328 \pm 30$ °C Ujiie *et al.*, 2018). Foliation,

developed during non-coaxial shear (Fig. 4.9) results in anisotropic permeability (Faulkner and Rutter, 2000; Huenges *et al.*, 1997; Kwon *et al.*, 2004), and this expected to guide fluids upward, below or within the subduction thrust (Audet *et al.*, 2009; Audet and Bürgmann, 2014; Peacock *et al.*, 2011).

Calculations presented in Section 4.10.1 suggest that at least tens to hundreds of cubic meters of fluid are required to precipitate one of the observed quartz veins. In subducting metabasalt, prehnite breakdown followed by chlorite breakdown causes two discrete releases of 5 vol% fluid, each equivalent to 0.05 m^3 H_2O per m^3 metabasalt. Comparison with the estimated minimum required fluid volumes suggests that a single vein in coastal Makimine mélange would require the fluid produced from at least 6600 m^3 of metabasalt experiencing prehnite breakdown, while a vein in the NMR would require the fluid from at least 1000 m^3 of metabasalt experiencing chlorite breakdown. The large volumes of oceanic crust required to dehydrate in order to supply fluid for the formation of a single vein are consistent with the concept of substantial proportions of the vein-forming fluid containing cumulative contributions from deeper dehydration reactions.

While metamorphic dehydration reactions are expected to be the main source of fluids to the plate boundary shear zone, metasomatic reactions along contacts between reactive lithologies may also release fluid. For example, in the Makimine mélange and the NMR, reactions between metasediment and metabasalt drive local dehydration of dm-scale layers within metasediments, adjacent to metabasalts (Ujiie *et al.*, 2021). This local dehydration is expected to result in pore fluid pressurisation, which potentially assists localised embrittlement along lithological contacts. Reactions between metasediment and metabasalt in in the Makimine mélange and the NMR also result in an increase in the proportion of albite, which is mechanically strong (Masuda *et al.*, 2019; Rybacki and Dresen, 2004), resulting in strengthening of the reacted material. A similar process of metasomatic reactions leading to fluid pressurisation and local strengthening is inferred to occur between serpentinite, and meta-sedimentary and meta-volcanic rocks in the Livingstone fault, deformed at $\sim 250 - 350°C$ (Tarling *et al.*, 2019). As only small volumes of rock are involved with these metasomatic reactions, metasomatism resulting in locally elevated fluid pressures may be particularly efficient as a rheological control if the bulk effective stress is already low.

Along the northern Hikurangi margin, the relative magnitudes of the principal compressive stresses decrease prior to SSEs and increase during SSEs, interpreted to reflect transient fluctuations in fluid pressure driving the periodicity of ETS events (Warren-Smith *et al.*, 2019). Along the Cascadia margin, temporal changes in shear wave velocity contrast after ETS events are interpreted to reflect temporary reduction in fluid pressure after SSEs (Gosselin *et al.*, 2020), also consistent with ETS associated with fluid pressure fluctuations. If veins reflect the opening of fractures followed by fluid migration, mineral precipitation, and fracture sealing (Section 4.10), then the process of vein formation triggers permeability to rapidly increase as the fracture opens, and then slowly decrease as the vein forms. Cyclical permeability could explain the transient fluctuations in fluid pressure associated to SSEs (Gosselin *et al.*, 2020; Warren-Smith *et al.*, 2019). Fig. 4.10 shows that either differential stress increase or fluid pressurisation could drive fracturing and vein formation, resulted in transient fluctuations in permeability and fluid pressure.

Overall, we envisage that the quartz veins preserved in the ductile shear zones precipitated from fluids derived from dehydration reactions in subducting oceanic lithosphere. At the conditions of coastal Makimine mélange and the NMR, discrete pulses of fluid release from oceanic crust were likely to cause local increases in fluid pressure, as mineral dehydration reactions would have been ongoing during the last recorded phase of subduction thrust-related deformation.

4.12 Implications for deformation processes in subduction zones

Microstructural observations indicate that in all of the studied shear zones, ductile creep was pervasive in hydrated oceanic crust and subducting sediment, accommodated by grain-scale, fluid-assisted, dissolution and precipitation, coupled to sliding along mechanically weak phyllosilicate foliations (Fig. 4.9). Fluid-present conditions are also demonstrated by syn-subdution growth of hydrous minerals in strain shadows (Fig. 4.5a).

Subducting sediments are fluid-rich as they lithify under water-saturated conditions and contain hydrous phyllosilicates. On the other hand, fresh oceanic crust formed at mid-ocean ridges is relatively dry, typically contain-

ing < 0.5 wt% H_20 (Jambon and Zimmermann, 1990; Nichols *et al.*, 2002) - much less than the metabasalts in the shear zones described here. As shown in Fig. 4.7, relatively fluid-rich zeolite, prehnite-pumpellyite and greenschist-facies equilibrium assemblages are thermodynamically favoured under fluid saturated conditions (Alt *et al.*, 1986; Barnes *et al.*, 2020). Mechanically weak phyllosilicate minerals occur within these equilibria, but, forming these equilibria requires the addition of water to the relatively dry igneous crust, possible through sea-floor hydrothermal circulation, faulting along transforms, or along the outer-rise of subduction zones (Alt *et al.*, 1986; Ranero *et al.*, 2003; Shillington *et al.*, 2015). Given that these hydration mechanisms are intrinsically local, rather than necessarily pervasive throughout the pre-subduction oceanic crust, the scale at which the equilibrium assemblages develop may be an important control on the strength of subducting oceanic crust.

Along the inferred range of possible P-T paths, the hydrated crust preserved in the studied shear zones progresses through prehnite breakdown at 270-290°C, and chlorite breakdown at 450-480°C, releasing a sum of ~ 10 mol% H_20 in two discrete pulses. Veins, developed at close to peak subduction at $\sim 328 \pm 30$°C in coastal Makimine mélange and at $\sim 500 \pm 50$°C in the NMR require conditions of especially low effective stresses, or substantial local deviatoric stress increase, to form, including somewhat lower effective stress than sliding on well-oriented weak phyllosilicate foliae (Fig. 4.9). We infer that prehnite and chlorite dehydration locally increased the rate of fluid supply to the thrust, generating patches where effective stress was especially low, increasing the spatial and temporal frequency of brittle failure within the ductile shear zones.

In inland Makimine mélange, deformed at $\sim 371 \pm 30$°C, veins are recognised, but are pervasively overprinted by later ductile deformation at stresses controlled by fluid-assisted diffusion creep in a wide, phyllosilicate-rich shear zone. The ductile deformation recorded in the inland Makimine mélange occurred within a wide P-T range within the greenschist facies where the mineral assemblage is stable and little fluid is released. Little local fluid release allows for effective stresses sufficiently high to suppress brittle failure, provided permeability allows for efficient up-dip migration of fluids. We suggest that here, stresses are relatively stable, and sub-critical, compared to the other studied locations, where potentially small fluctuations in effective stress or fluid pressure close to the failure envelope cause cyclical fracturing and ductile creep.

In the NMR, vein distribution at the outcrop scale suggests local fracturing was more intense along lithological contacts, within a dominantly ductile but heterogenous shear zone. Along boundaries between different viscosity materials, mechanical contrasts suggest deformation likely occurred at locally elevated strain rates and higher stresses (e.g., Beall *et al.*, 2019b; Sibson, 1980; Ujiie *et al.*, 2021). That veins exist requires failure to have been at least partially tensile, requiring differential stress to have been low (Fig. 4.10). It is possible that veins in the NMR reflect one, or a combination of tensile or hybrid tensile-shear fractures, however structures that reflect failure mode are overprinted by recrystallisation. The preserved structures imply the NMR only hosts relatively small-displacement, clustered fractures, indicative of a small contribution of brittle failure to a dominantly ductile regime, as for example suggested by Gao and Wang (2017) as a mechanism for ETS below the base of the seismogenic zone. The relatively local and small displacement fracturing recorded in the studied exposures, particularly in the NMR, is consistent with the very small proportion of inter-plate slip accommodated by LFEs during ETS events (Chestler and Creager, 2017).

Overall, cyclicity between brittle and ductile deformation is suggested to arise under low effective stress, low differential stress conditions by (a); fluid pressurisation, fracturing, and quartz vein formation, and (b); variations in stress and strain rate along mechanical contrasts. Local conditions along compositional contacts are likely affected by metasomatic reactions, which may release fluids and change local rheology through crystallisation of new phases (Tarling *et al.*, 2019; Ujiie *et al.*, 2021). The shear zone scale ambient conditions, however, involve stresses that are low relative to frictional strength, enabled through deformation by dissolution-precipitation creep across a wide, fluid-saturated shear zone. In this realm, ductile deformation dominates, and brittle deformation is allowed by local failure conditions and limited in space because propagating fractures must overcome a large difference between ambient stress and frictional strength (e.g., Fagereng and Beall, 2021).

4.13 Conclusions

We have considered structures formed during brittle and ductile deformation, preserved in three shear zones exhumed from different metamorphic grades

along a kinematically similar, Late Cretaceous subduction thrust. Mineral assemblages within deformed metabasalts and metasediments indicate that the three studied exposures deformed within a temperature range spanning the transitional frictional-viscous region below the base of the seismogenic zone. In the studied shear zones, oceanic crust and subducted sediments deformed ductilely at low driving stresses. In all lithologies, the dominant deformation mechanism is frictional-viscous creep, accommodated by a composite mechanism involving sliding along phyllosilicate foliations and dissolution-precipitation creep of interstitial non-phyllosilicates, sensitive to grain size, friction, mineral solubility, effective stress, and strain rate.

In the studied shear zones, mixed brittle-ductile behaviour occurred at P-T conditions corresponding to specific dehydration reactions in the oceanic crust; prehnite breakdown at 270-290°C and chlorite breakdown at 450-480°C. Shear zone outcrops deformed at P-T conditions between these dehydration reactions likely deformed by aseismic creep, reflected by relatively homogeneous ductile structures. In heterogeneous shear zones that preserve mixed brittle-ductile deformation, the distribution of quartz veins suggests that variations in differential stress (and related strain rates) along mechanical contrasts stimulated local, transient embrittlement.

Our results imply that specific dehydration reactions can drive embrittlement within the ductile subduction thrust, and that the location of these reactions can control the distribution of brittle and ductile deformation. Our results also imply that brittle deformation can be driven by local variations in stresses or rheological effects of metasomatic reactions along mechanical contrasts in heterogeneous shear zones, but that this effect is more apparent if effective stresses are low or viscosity contrasts are high. Consequently, the hydration state and petrography of the subducting lithosphere, and the presence of mechanical heterogeneity are both potential drivers of the occurrence and distribution of embrittlement along otherwise ductile subduction thrusts.

Chapter 5

Strength of hydrated oceanic crust

5.1 Abstract

The rheology of the metamorphosed oceanic crust may be a critical control on megathrust strength and deformation style. However, little is known about the strength and deformation style of metamorphosed basalt. Exhumed megathrust shear zones exposed on Kyushu, SW Japan, contain hydrous metabasalts deformed at temperatures between ~ 300°C and ~ 500°C, spanning the inferred temperature-controlled seismic-aseismic transition. Field and microstructural observations of these shear zones, combined with quartz grain-size piezometry, indicate that metabasalts creep at shear stresses < 100 MPa at ~ 370°C and at shear stresses < 30 MPa at ~ 500 °C. These values are much lower than those suggested by viscous flow laws for basalt. The implication is that relatively weak, hydrous, metamorphosed oceanic crust can creep at low viscosities over a wide shear zone and have a critical influence on plate interface strength and deformation style around the seismic-aseismic transition.

This chapter is based on the published paper: Tulley, C. J., Fagereng, Å., & Ujiie, K. (2020). Hydrous oceanic crust hosts megathrust creep at low shear stresses. Science Advances, 6(22), eaba1529. https://doi.org/10.1126/sciadv.aba1529.

5.2 Introduction

Along convergent margins, a kilometres-thick shear zone typically separates the relatively rigid subducting and overriding plates (Abers, 2005). A much-used conceptual model is that the top of the mechanically strong basaltic oceanic crust is lubricated by weak subducting sediments (Behr *et al.*, 2018; Shreve and Cloos, 1986; Sobolev and Brown, 2019), allowing the plate interface to creep at low shear stresses. However, the thickness of subducting sediment is variable within and between margins, and during subduction, mineral dehydration and compaction may contribute to volume reduction $> 50\%$ by the time sediments have been buried to > 10 km (Moore and Vrolijk, 1992; Peacock, 1990). Subducting oceanic crust is also topographically rough in many creeping margins, meaning that creep occurs despite the presence of seamounts and horsts with thin sediment cover Wang and Bilek (2011). Therefore, although seismic observations commonly suggest the presence of a kilometres-thick creeping layer at the top of deeply subducted oceanic lithosphere (Tichelaar and Ruff, 1993), the oceanic crust may be exposed to the overriding plate along sediment-starved margins and in areas with thin to no sediment coverage. Creep of the oceanic crust would negate the need for a continuous layer of deeply subducted lubricating sediments, but it is unclear whether oceanic crust can be sufficiently weak to accommodate plate-rate creep at low inferred shear stresses.

Fresh basaltic rocks have high frictional strengths $\mu \sim 0.75$ and display velocity-weakening behaviour (He *et al.*, 2007), a requirement for earthquake nucleation. Viscous creep of dry basalt at shear stresses < 200 MPa requires temperatures > 650 °C, assuming a moderate strain rate ($10^{-12}s^{-1}$) (Mackwell *et al.*, 1998). Such high strengths are incompatible with the inferred low shear strengths of creeping plate interfaces at the base of the seismogenic zone (Hardebeck and Loveless, 2018). However, phyllosilicate minerals that form during metamorphism of hydrated oceanic crust at greenschist, blueschist, and amphibolite facies conditions (Fagereng *et al.*, 2018) deform at low shear stresses and are velocity strengthening over a wide pressure-temperature (P-T) range

(Mares and Kronenberg, 1993; Okamoto *et al.*, 2019). The transition from blueschist or amphibolite to eclogite is expected to notably increase the viscosity of oceanic crust (Behr *et al.*, 2018); however, here, we are considering sub-eclogite facies conditions.

We investigate the hypothesis that hydrous, metamorphosed oceanic crust with a weak phyllosilicate-bearing mineralogy may creep at shear stresses low enough to accommodate significant plate interface displacement at geological strain rates. Field and microstructural observations from exhumed megathrust shear zones exposed at three localities on Kyushu, southwest Japan, indicate that, during warm subduction, hydrated oceanic crust is far weaker than dry basalt and comparable in strength to metasediment. We conclude that hydrous oceanic crust may accommodate significant megathrust shear strain and therefore may have a strong influence on the strength and deformation style of the plate interface.

5.3 Microstructures within hydrated oceanic crust

At the thin-section scale, metabasalt in coastal Makimine mélange contain albite-poor solution selvages, which define a poorly developed anastomosing foliation separating relatively albite-rich lenses which are elongate parallel to foliation (Fig. 4.4a, b). The typical spacing between solution selvages is 250 μm, and the thickness of each selvage ranges from 10 to 100 μm. EDS maps highlight reduced albite content within solution selvages, relative to the albite-rich lenses, and show a well-developed microscale foliation defined by aligned chlorite.

In inland Makimine mélange, the foliation in metabasalt is defined by aligned actinolite, chlorite, and muscovite. Clinopyroxene grains have a weak shape preferred orientation (SPO) with grain long axes parallel to foliation (Fig. 4.5). EBSD analysis of clinopyroxene indicates a weak crystallographic preferred orientation (CPO) with [001] aligned to the foliation (Fig. 5.1a), and lattice distortions across clinopyroxene grains are generally $< 2^{\circ}$(Fig. 5.1b). Actinolite forms asymmetric strain shadows adjacent to clinopyroxene grains (Fig. 4.5). Small (< 50 μm) albite grains are dispersed throughout the metabasalt and also have a strong SPO with long axes parallel to foliation (Fig. 4.5a).

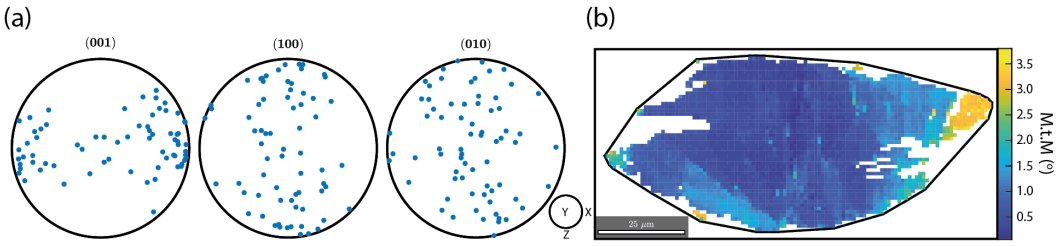

Figure 5.1: EBSD orientation data from clinopyroxene in inland Makimine mélange metabasalt. (a) Pole figures showing the orientation of 69 pyroxene grains (one point per grain) from inland Makimine metabasalt. There is a weak [001] preferred orientation. (b) Map of pixel misorientation relative to the mean grain orientation, for a pyroxene grain. Local distortions are generally $< 2°$.

In metabasalt from the NMR, long axes of albite and actinolite grains define the stretching lineation in amphibolite schist, whereas aligned muscovite and chlorite platelets define the foliation. Minor epidote, titanite, and apatite also occur in the metabasalt. Quartz is present in boudinaged veins and as dispersed single grains. Pole figures for muscovite and chlorite show a strong CPO consistent with the alignment observed in thin section. Both muscovite and chlorite have the common phyllosilicate preferred orientation (Dempsey *et al.*, 2011) with (001) parallel to foliation and [100] distributed in a girdle along the foliation plane (Fig. 5.3). Pole figures indicate that some chlorite grains have (001) oriented nearly orthogonal to the foliation; these grains occur in strain shadows adjacent to albite grains.

Actinolite has a strong CPO with [001] parallel to lineation and (100) parallel to foliation (Fig. 5.3). There are, however, no microstructural indicators (such as subgrains or bulging grain boundaries) of dislocation creep in actinolite. EBSD analysis indicates that local misorientations within grains are typically < 3 °(Fig. 5.2a) and the total distortion within grains is generally no more than a few degrees (Fig. 5.2b). In contrast to the hydrous minerals in the metabasalt, albite has no clear CPO (Fig. 5.3) but does have a strong SPO with long axes parallel to lineation (Fig. 4.6a). Boudinaged quartz veins have a strong CPO, with two c-axis clusters inclined between the Y and Z kinematic directions (Fig. 5.3) indicative of rhomb $< a >$ slip (Schmid and Casey, 1986).

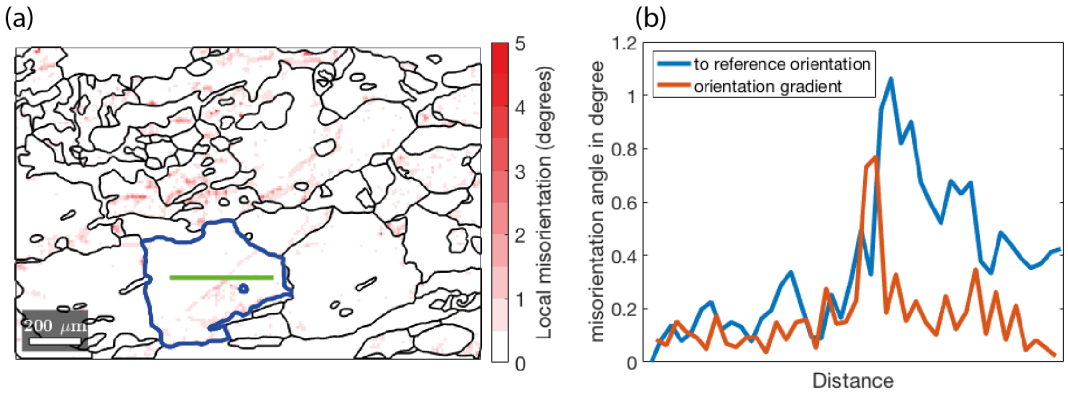

Figure 5.2: EBSD orientation data from NMR plagioclase. (a) Kernal average misorientation (misorientation of pixels with respect to neighbour pixels) within grains is generally < 3 °. (b) Orientation profile across a representative grain; the total internal distortion is generally less than a few degrees.

5.4 Fabric forming mechanisms

The foliation observed in coastal Makimine metabasalt corresponds to alternating albite-poor and albite-rich layering (Fig. 4.4), interpreted to represent local dissolution of albite along planes orthogonal to σ_1. Localised dissolution of albite produced relative increases in chlorite along dissolution seams. In inland Makimine mélange, the SPO of clinopyroxene and albite also indicates pressure solution, again accommodating shortening orthogonal to σ_1. Aligned actinolite and chlorite form asymmetric strain shadows adjacent to clinopyroxene porphyroclasts and are interpreted as replacement textures that grew during noncoaxial shear (Fig. 4.5). Overall, the fabric in both coastal and inland Makimine metabasalts is interpreted to be the product of coaxial shortening by dissolution-precipitation creep, coupled to noncoaxial shear by frictional sliding along foliae. The SPO of albite, actinolite, and dispersed quartz grains in NMR amphibolite indicates foliation-normal shortening associated with grain growth in preferred orientations. The CPO and SPO of chlorite and muscovite (Figs. 5.3 and 4.6) are interpreted to have formed by rotation and growth of the phyllosilicates into mechanically stable orientations during shortening and noncoaxial shear.

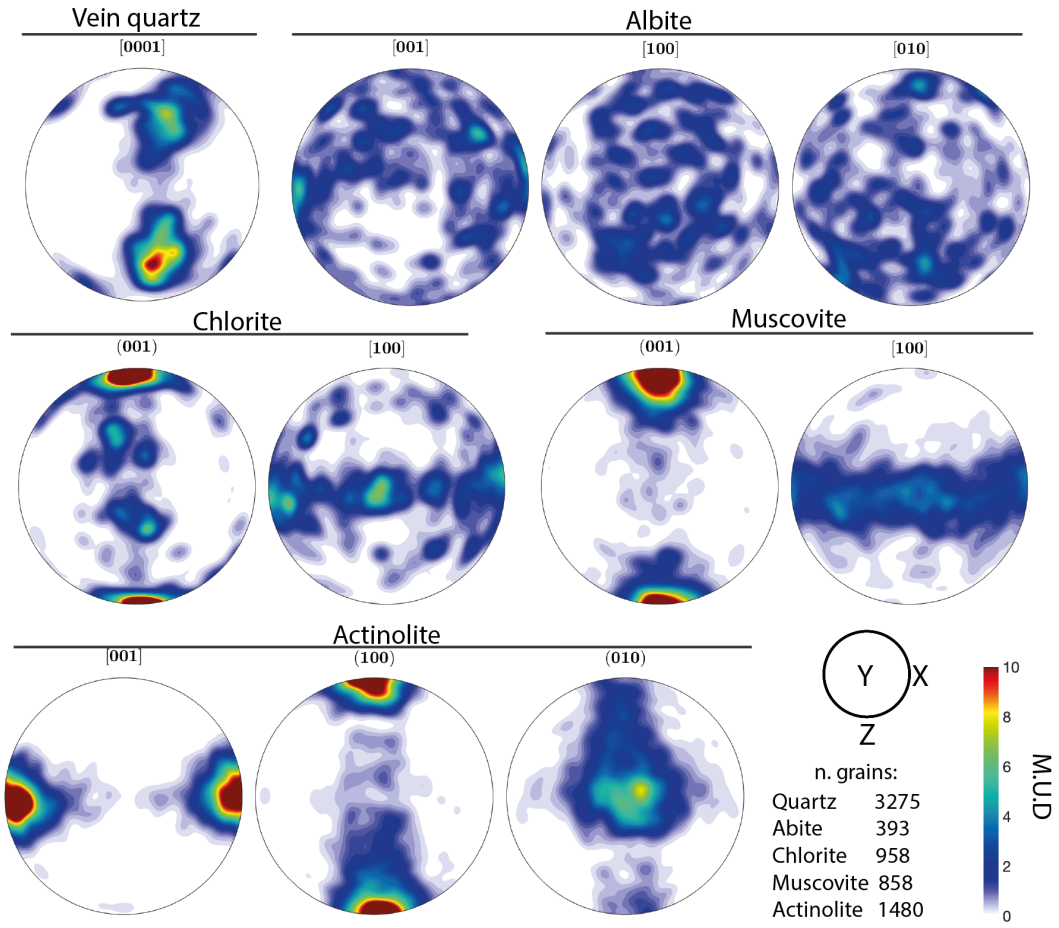

Figure 5.3: Equal area, lower hemisphere pole figures for grain orientations in amphibolite from the NMR, showing one point per grain. Contours in units of multiples of a uniform distribution (MUD); regions with MUD > 10 are shown in dark red. Quartz (boudinaged veins) shows two clusters each inclined between the Y and Z kinematic directions. Albite shows no clear preferred orientation. Muscovite and chlorite have strong preferred orientations with (001) planes parallel to foliation. Muscovite [100] forms a continuous girdle parallel to foliation, whereas in chlorite [100] is weakly clustered parallel and perpendicular to the shear direction. Actinolite [001] axes are aligned with the shear direction, and (100) and (101) planes lie parallel and orthogonal to foliation, respectively.

5.5 Frictional-viscous creep in hydrated oceanic crust

In the coastal Makimine mélange metabasalt, the formation of a solution cleavage gives rise to a mechanical anisotropy, given the contrasting frictional strengths of albite and foliated chlorite ($\mu = 0.75$ and $\mu = 0.2$, respectively; He *et al.*, 2007; Okamoto *et al.*, 2019). In the inland Makimine metabasalt, the chlorite, actinolite, and epidote foliation is locally disrupted by rigid clinopyroxene grains, giving rise to a curvi-planar foliation (Fig. 4.5). SPO in albite and clinopyroxene, and the formation of actinolite and chlorite in strain shadows adjacent to clinopyroxene, suggests that deformation of the metabasalt occurred at least partially by dissolution-precipitation creep. Overall, deformation is interpreted to have occurred by frictional sliding along the actinolite, chlorite, and muscovite foliation, coupled to dissolution-precipitation creep of albite and clinopyroxene. The importance of dissolution-precipitation creep is consistent with previous observations of high-pressure, low-temperature metamorphic rocks (Wassmann and Stöckhert, 2013).

In NMR amphibolite, slip along the phyllosilicate foliae is likely to be an important deformation mechanism, given the contrast between strong albite and the weak phyllosilicate minerals (He *et al.*, 2007; Okamoto *et al.*, 2019). The CPO of muscovite and chlorite (Fig. 5.3) reflects easy slip along (001) in phyllosilicates compared to slip along other crystallographic planes (Mares and Kronenberg, 1993). Mechanically strong albite grains are commonly surrounded by the phyllosilicates and amphibole (Fig. 4.6), suggesting that albite is a strong phase in a relatively weak phyllosilicate-dominated matrix. Crystallographic preferred orientations in albite (Fig. 5.3) do not correspond to recognised slip systems, suggesting deformation by a mechanism other than dislocation creep. Grains of actinolite, muscovite, and chlorite commonly occur as inclusions within albite and almost always have the same orientation as isolated grains (Fig. 4.6a), implying that albite grain boundaries moved diffusively around the hydrous minerals. These observations together strongly suggest that albite is deformed by diffusion, despite having a grain size much larger than is usually reported for diffusion creep (Rybacki and Dresen, 2004; Wassmann and Stöckhert, 2013). One possibility to explain the large grain sizes in albite is grain growth, stimulated by Na-rich fluids inferred to be

present at peak metamorphic conditions in the NMR (Mori *et al.*, 2014). Given the slow strain rates that can be accommodated by diffusion creep in albite at Nishisonogi-like conditions and grain sizes (Rybacki and Dresen, 2004) and the relatively weak strength of (001) planes in phyllosilicates (Mares and Kronenberg, 1993; Okamoto *et al.*, 2019), we expect that albite accommodated minor amounts of strain relative to the phyllosilicates.

5.6 Deformed quartz veins in oceanic crust

Ductilely deformed quartz veins aligned with a foliation implies that the veins experienced deformation at the foliation-forming conditions. As the veins deformed by dislocation creep, their microstructure should reflect the stress conditions during deformation. Piezometers relate dynamically recrystallised grain sizes to flow stresses during viscous deformation (Section 2.7), allowing estimates of the strength of naturally deformed rocks. Quartz veins are present in the inland Makimine metabasalt, but many of the quartz grains are pinned by chlorite, making them unsuitable for piezometry. Using an EBSD-based method (Cross *et al.*, 2017), we calculated a recrystallised quartz grain size of $10.0 \pm 4.9\mu$m from foliation-parallel quartzite layers with pinch-and-swell geometries in inland Makimine metasediment (Fig. 5.4).

These grain sizes suggest differential stresses in the range of 87 to 187 MPa. We expect that the strengths obtained from quartzite layers in metasediment are comparable to the strength of metabasalt, given similar pinch-and-swell geometry of quartzite and metabasalt layers within the metasediment and that the amplitude and wavelength of pinch-and-swell structures reflect the magnitude of viscosity contrast (Ramsay, 1967).

Boudinaged quartz veins in NMR amphibolite have microstructures indicating deformation mostly by grain-boundary migration recrystallisation. We isolate a population of grains with low internal distortion and a grain size of 70.3 ± 44 μm (Fig. 5.5), giving differential stresses of 21 to 60 MPa, again using an EBSD-based method (Cross *et al.*, 2017).

These stresses are an upper bound on the strength of metabasalt, as the boudinage of quartz veins implies that they are stronger than the host amphibolite. The piezometer-derived strength estimates and RSCM temperature estimates for the NMR and inland Makimine mélange define a strength-

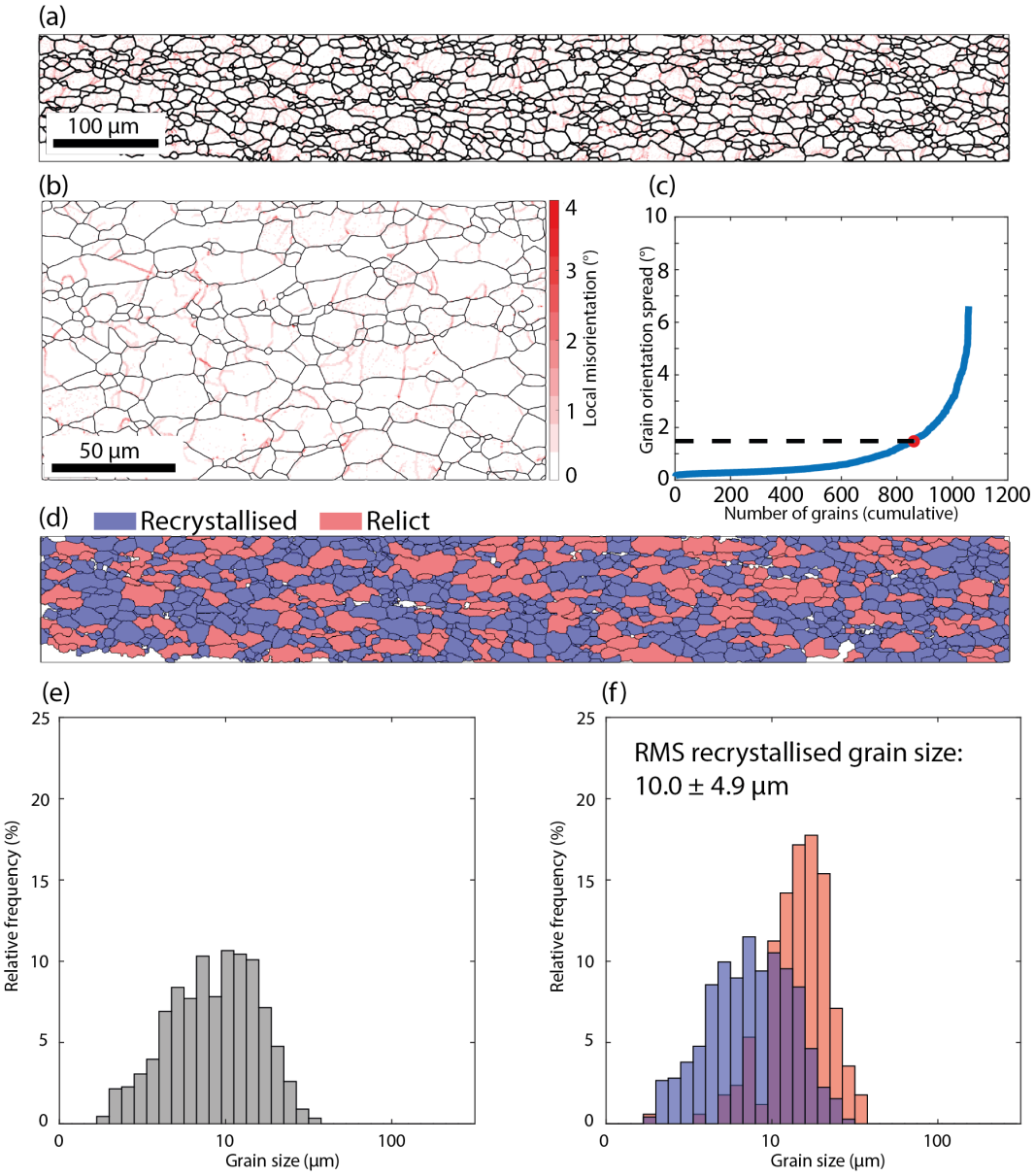

Figure 5.4: EBSD-derived orientation data from a recrystallised quartz vein in metasediment in inland Makimine mélange.(a) Map showing all of the analysed grains, coloured according to the local misorientation within each grain (colour scale same as (b).(b) Map showing a smaller area of the vein. (c) Plot of the cumulative number of grains verses the range of orientations within each grain (grain orientation spread; GOS). The knee in the curve (red circle) reflects the threshold between recrystallised and relict grains. (d) Recrystallised and relict grains separated on the basis of GOS. (e) Log_{10} grain size distribution for all of the analysed grains. (f) Same as (e), but with relict and recrystallised grains colored separately.

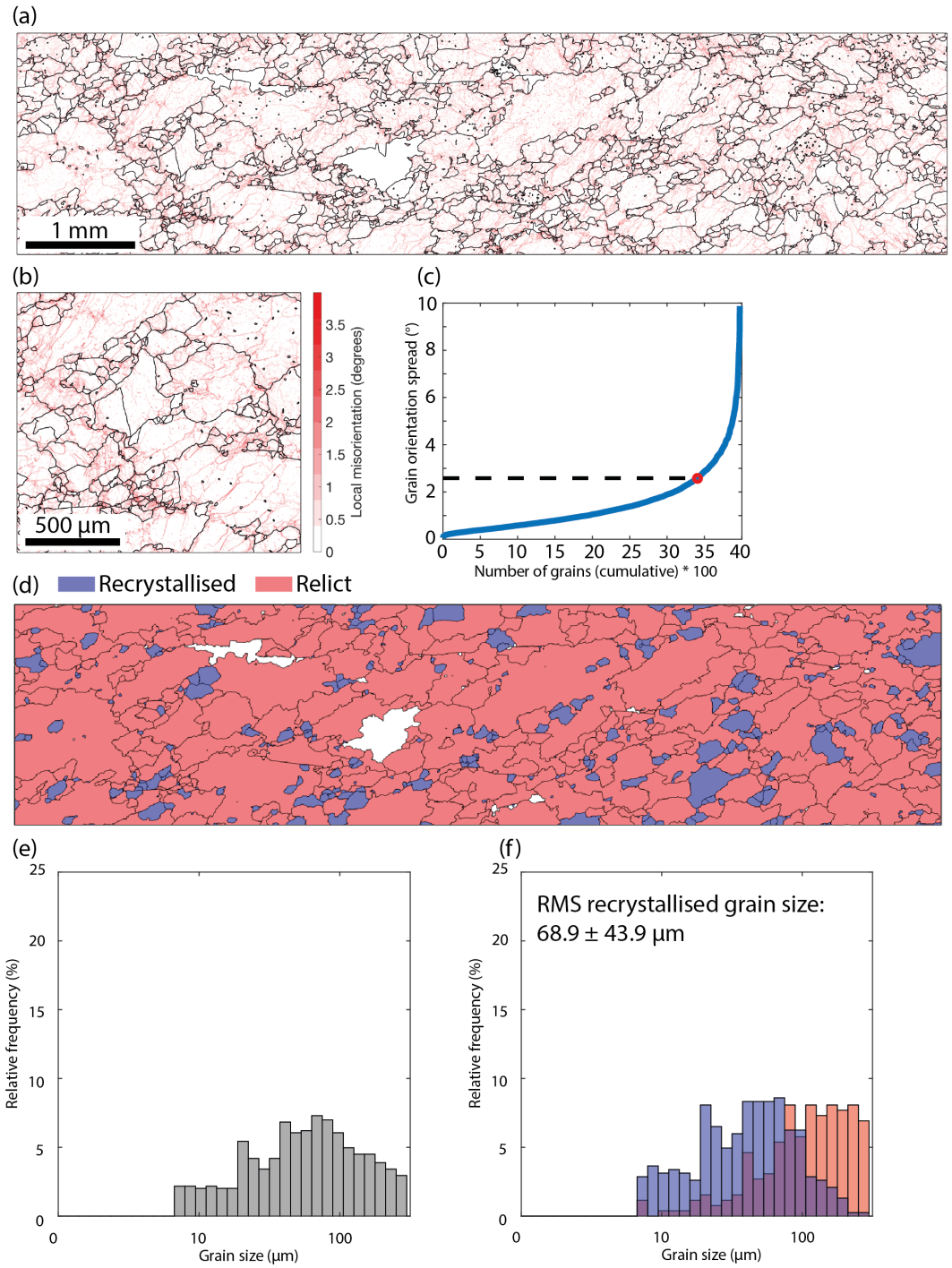

Figure 5.5: EBSD-derived orientation data from a recrystallised quartz vein in amphibolite from the NMR.(a) Map showing all of the analysed grains, coloured according to the local misorientation within each grain (colour scale same as (b).(b) Map showing a smaller area of the vein. (c) Plot of the cumulative number of grains verses the range of orientations within each grain (grain orientation spread; GOS). The knee in the curve (red circle) reflects the threshold between recrystallised and relict grains. (d) Recrystallised and relict grains separated on the basis of GOS. (e) Log_{10} grain size distribution for all of the analysed grains. (f) Same as (e), but with relict and recrystallised grains colored separately.

temperature curve for the Kyushu metabasalts. Comparison with a quartz rheology (Hirth *et al.*, 2001) suggests that the deformation preserved in the Kyushu metabasalts occurred at a strain rate of $\sim 10^{-12}s^{-1}$ (Fig. 5.6), consistent with previous bulk strain rate estimates for margin-scale shear zones (Fagereng and Biggs, 2019).

5.7 Strength of the oceanic crust

For ease of comparison with stresses required for frictional sliding, the differential stresses suggested by quartz grain size piezometry were converted to shear stresses following Behr and Platt (2014):

$$\tau = \frac{(\sigma_1 - \sigma_3)}{\sqrt{3}} \tag{5.1}$$

At a strain rate of $\sim 10^{-12}s^{-1}$, approximately equivalent to the strain rate experienced by the Kyushu metabasalts (Fig. 5.6a), the commonly used flow law for dry diabase (Mackwell *et al.*, 1998) suggests that unaltered oceanic crust requires temperatures > 650 °C for shear stresses to be less than < 200 MPa (Fig. 5.6b). In contrast, our geologically constrained creep strengths for relatively competent quartzite layers deformed during bulk noncoaxial shear within hydrous metabasalt suggest that deformation of hydrated oceanic crust occurred at shear stresses of approximately 50 to 108 MPa at 370 °C and less than 12 to 35 MPa at 500 °C.

Overall, we observed that phyllosilicates are ubiquitous in the Kyushu metabasalts and well oriented for slip along mechanically weak basal planes. We infer that the presence of interconnected phyllosilicates and water-saturated conditions in the Kyushu metabasalts facilitated solution-precipitation creep and frictional sliding along phyllosilicate laminae (Bos and Spiers, 2002), accommodating macroscopically ductile deformation of the oceanic crust at shear stresses far lower than predicated for unaltered basalt. To illustrate this difference between hydrous metabasalt and unaltered basalt, Fig. 5.6b compares our geologically constrained ductile shear strengths for metabasalt to existing mechanical data, assuming a strain rate of $\sim 10^{-12}s^{-1}$, a pore fluid factor (pore fluid pressure/vertical stress) $\lambda = 0.8$, and a geothermal gradient of 20 °C/km. Our geologically constrained maximum strengths are significantly less than predicted by flow laws for dry diabase (Mackwell *et al.*, 1998). The

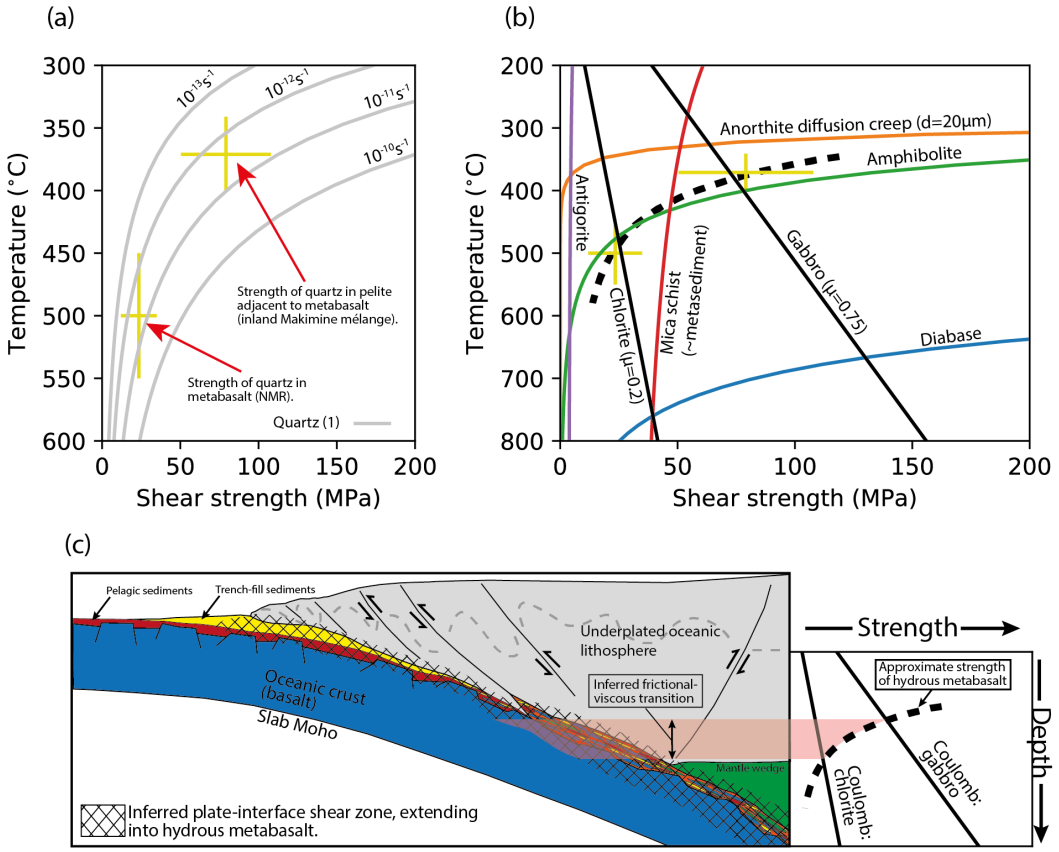

Figure 5.6: Piezometer-derived shear stress estimates and RSCM-derived temperature estimates for quartz veins deformed in inland Makimine mélange and the NMR. (a) Experimentally determined strength-temperature curves for quartz undergoing dislocation creep (Hirth *et al.*, 2001) give stresses close to the estimated values for the exhumed shear zones at a strain rate of $10^{-12}s^{-1}$. (b) Shear stress and temperature estimates define a strength-temperature curve for hydrous oceanic crust, which is far weaker than dry diabase (Mackwell *et al.*, 1998). Coulomb strengths with friction $\mu = 0.75$ and $\mu = 0.2$ represent the cohesion-less strength of unaltered oceanic crust (He *et al.*, 2007) and chlorite (Okamoto *et al.*, 2019), respectively (assuming a pore fluid factor $\lambda = 0.8$). The sketched strength curve suggests a frictional-viscous transition near $\sim 400°C$. The mica schist flow law (Shea and Kronenberg, 1992) represents the viscous strength of phyllosilicate-rich subducted sediment. Viscous strengths for antigorite and amphibolite are taken from (Hilairet *et al.*, 2007) and Hacker and Christie (1990), respectively. (c) Schematic cross section shows the broad plate interface shear zone extending into hydrated oceanic crust. As represented here, the frictional-viscous transition in hydrated oceanic crust would occur up-dip of the mantle wedge corner.

amphibolite flow law of Hacker and Christie (1990) tracks stresses close to the maximum stresses constrained by the piezometer. The Coulomb strengths of gabbro (He *et al.*, 2007) and chlorite (Okamoto *et al.*, 2019), representing end-member frictional strengths for the oceanic crust, intersect the estimated ductile strength-temperature curve for hydrous metabasalt at shear stresses between $\sim$ 60 MPa and $\sim$ 25 MPa at temperatures between $\sim$ 370 °C and $\sim$ 450 °C (Fig. 5.6b), implying a frictional-viscous transition for hydrous metabasalts within these shear stress and temperature ranges.

Subducted phyllosilicate-rich sediments represented by a mica-schist flow law (Shea and Kronenberg, 1992) have a strength approximately equal to our piezometer estimate at $\sim$ 370 °C but are stronger than our piezometer estimate for metabasalt at $\sim$ 500 °C (Fig. 5.6b). Our field observations of long wavelength, low amplitude pinch and swell of ductilely deformed metabasalt within metasediment in Makimine mélange exposures (Figs. 4.2 and 4.1) suggest that hydrated oceanic crust and metasediment have similar viscosities, but that hydrated oceanic crust is slightly more viscous. Parallel layering of metasediment and amphibolite in the NMR is not as clear because of the limited spatial extent of the outcrop. However, exposed metasediment-amphibolite contacts are approximately planar (Fig. 4.2), and we do not observe indications of marked viscosity contrasts between metasediment and amphibolite. Another mineral commonly inferred to be important for subduction thrust shear is antigorite serpentine. The power-law equation for dislocation creep in antigorite (Hilairet *et al.*, 2007) predicts shear strengths < 5 MPa over the entire temperature range considered (Fig. 5.6). However, the mechanisms controlling ductile deformation in natural antigorite are uncertain, as is the extrapolation of laboratory behaviour to nature (Auzende *et al.* (2015); see Chapter 6 for discussion).

5.8 Implications for active margins

In general, the extent of weakening by growth of phyllosilicates will depend upon their volume fraction and interconnectivity (Handy, 1990). The volume fraction of phyllosilicates in metabasalt, and the strain accommodated by dissolution-precipitation creep, will primarily depend on the amount of hydrous fluid available to the crust during subduction and any initial clay content

induced by hydration at the mid-ocean ridge, on the sea floor, and at the outer rise. The estimated strengths of the exhumed hydrous metabasalts suggest that if subducting crust is sufficiently hydrated, then creep in metabasalt can accommodate megathrust strain at similar driving stress to weak phyllosilicate-rich sediments, negating the need for a continuous layer of lubricating subducted sediment to explain a low viscosity plate interface at the base of the seismogenic zone. An important depth limitation to extrapolation of this conclusion is that the weakness of metabasalt will only apply at pressure, temperature, and fluid conditions unsuitable for pervasive eclogitization.

Taking the frictional strengths of chlorite (Okamoto *et al.*, 2019) and gabbro (He *et al.*, 2007) as lower and upper bounds on the frictional strength of the oceanic crust, and assuming a thermal gradient of 20 °C/km and a pore fluid factor of $\lambda = 0.8$, the frictional-viscous transition for hydrated oceanic crust is expected to occur in the range of 370 °C to 450 °C at shear stresses between 60 MPa and 25 MPa (Fig. 5.6b). On this basis, we suggest that the frictional-viscous transition in hydrated oceanic crust may influence the bulk rheology and slip behaviour of the subduction thrust interface in this temperature range. Lateral variations in creep versus seismogenic slip may also be explained by variations in basalt rheology. Faulting on the sea floor and at the outer rise is likely to increase permeability, allowing locally pervasive hydration of the oceanic crust. Given that hydration may vary from margin to margin, and within margins, the strength of the basaltic crust may be quite variable. We note that if the basaltic crust is hydrous and foliated, then the low velocity seismic signals that are commonly interpreted as the sediment-dominated megathrust may also originate from hydrated oceanic crust. Overall, this study provides a field and microstructural basis to recent margin-scale observations in Alaska (Shillington *et al.*, 2015), where it has been suggested that plate interface creep occurs in areas where the oceanic crust is more hydrated. Weakening of the oceanic crust because of hydration may be a common process along all creeping margins. We suspect that, along colder margins, our observations may be applicable at greater depths, because the deformation mechanisms we infer are largely temperature (rather than pressure) sensitive.

5.9 Conclusion

Coastal Makimine mélange, inland Makimine mélange, and NMR record Late Cretaceous plate boundary deformation at the Eurasian margin. Peak metamorphic temperatures from 300 °C to 500 °C suggest that these three shear zones are exhumed analogs for deformation at and below the base of a megathrust seismogenic zone. In all three shear zones, metabasalt contains aligned and interconnected phyllosilicate minerals surrounding more competent minerals deformed by diffusion creep with dominant shear sense consistent with paleo-subduction kinematics. Paleo-strength estimates using recrystallised quartz grain-size piezometry support the hypothesis of weak hydrous metabasalts; calculated strengths for the exhumed metabasalts are comparable to metasediments and are significantly weaker than experimentally determined flow laws for unaltered diabase. In general, the results suggest that the strength of hydrous oceanic crust is weak enough to control subduction thrust rheology in the viscous regime at the base of the seismogenic zone. Hydrous metabasalts may therefore form a substantial part of the weak, tabular zones commonly inferred to be present along subduction interfaces, instead of or in addition to the metasediments typically thought to make up this layer. Consequently, the hydration state of oceanic crust may have a profound control on the depth of interseismic coupling, particularly in relatively sediment-starved margins.

Chapter 6

Strain and strain-rate dependent rheology of antigorite

6.1 Abstract

Antigorite serpentinite is expected to have an important role in controlling the behaviour of the fore-arc mantle wedge and the plate boundary along subduction zones. However, despite substantial experimental investigation, the processes controlling the rheology of antigorite at mantle wedge conditions, are still unclear. An exhumed plate boundary shear zone exposed on near Nagasaki, SW Japan, shows lenses of antigorite serpentinite deformed together with metamorphosed ocean plate lithologies under amphibolite facies conditions. Microstructural observations indicate that antigorite deforms by a composite mechanism involving pressure solution creep and sliding along grain boundaries; a mechanism yet to be recognised in laboratory experiments. Our observations also indicate that the development of foliation in antigorite, driven by the pressure solution creep mechanism, results in a reduced apparent viscosity. Variation in the intensity of the foliation gives rise to viscosity heterogeneity, which we infer to contribute to mixed brittle-viscous behaviour during non-coaxial strain. Additionally, observation of foliation in the metamorphosed ocean plate stratigraphy wrapping lenses of antigorite implies that, at least at the conditions of the studied shear zone, antigorite may be more viscous than subducted sediments and hydrated oceanic crust.

6.2 Introduction

Antigorite, the high temperature serpentine polytype, is thought to occur at subduction zones, where fluids released from subducting oceanic lithosphere hydrate the overlying mantle wedge (Hyndman and Peacock, 2003; Kamiya and Kobayashi, 2000; Peacock, 1993). The inferred low viscosity of antigorite at mantle-wedge conditions (Amiguet *et al.*, 2014; Chernak and Hirth, 2010; Hilairet *et al.*, 2007) suggests that it may strongly influence mantle-wedge and plate-interface dynamics (van Keken, 2003; Wada *et al.*, 2008). Additionally, laboratory observations of slow slip and slow fault propagation in antigorite (French and Zhu, 2017; Okazaki and Katayama, 2015), and velocity-dependent rate and state friction parameters (Reinen *et al.*, 1991), suggest antigorite may deform by a range of slip styles, potentially including episodic tremor and slow slip (ETS). However, the strength of antigorite relative to ocean plate lithologies, and the rheology of antigorite at mantle wedge conditions and geological strain rates is unclear (Amiguet *et al.*, 2014; Auzende *et al.*, 2015).

Deformation experiments on antigorite have revealed a range of microstructures, reflecting variations in mineral-scale deformation mechanisms. In triaxial laboratory experiments at room temperature and confining pressure > 200 MPa, antigorite deforms in a distributed manner by slip along shear microcracks formed parallel to the (001) cleavage (David *et al.*, 2018; Escartín *et al.*, 1997; Raleigh and Paterson, 1965). Nanoindentation experiments also suggest deformation occurs by sliding along shear microcracks parallel to (001) (Hansen *et al.*, 2020). Experiments at $>\sim 300$ °C show contrasting results; some experiments produce homogeneous deformation throughout the sample, interpreted to reflect dislocation creep (Hilairet *et al.*, 2007) or dislocation creep with a contribution from cataclasis (Amiguet *et al.*, 2014), while others show deformation localised along narrow tabular shear zones, interpreted to reflect deformation controlled by frictional processes (Chernak and Hirth, 2010; French *et al.*, 2019; Hirauchi *et al.*, 2020; Proctor and Hirth, 2016).

Naturally deformed antigorite preserves microstructures indicating a range of deformation mechanisms. Subgrains, kinking, and stacking disorders (Amiguet *et al.*, 2014; Auzende *et al.*, 2015; Liu *et al.*, 2020; Padrón-Navarta *et al.*, 2012) suggest contributions from dislocation motion. Indented, interpenetraitng grain boundaries, and antigorite formed in strain shadows (Auzende

et al., 2015, 2006; Liu *et al.*, 2020; Wassmann *et al.*, 2011) suggests contributions from dissolution-precipitation creep. Grain rotation and the development of a crystal preferred orientation with limited evidence for dislocation motion (Nagaya and Wallis, 2018) suggests grain boundary sliding is also an important mechanism. Which of these mechanisms, or combination of mechanisms, controls antigorite rheology at mantle-wedge conditions (including at natural strains, strain rates, and fluid conditions) is uncertain. As strength and rheology are controlled by the rate-limiting deformation mechanism (e.g., Knipe, 1989; Rutter, 1976), understanding natural deformation mechanisms in antigorite is key to the meaningful extrapolation of laboratory results, and understanding antigorite rheology in natural, active shear zones.

Structures within the NMR provide constraints on the relative viscosity of antigorite and ocean plate lithologies, and the physical mechanisms that control antigorite rheology at natural deformation conditions. Microstructural observations indicate that antigorite deforms by a strain-rate dependent mechanism involving dissolution-precipitation creep and grain boundary sliding, and that fabric development accompanied by non-coaxial strain may drive progressive weakening of antigorite. Outcrop observations indicate that antigorite deforming by this mechanism is more viscous than adjacent and interleaved ocean plate stratigraphy, implying that a serpentinite mantle wedge may not be required to facilitate slab-mantle decoupling. We conclude that dissolution-precipitation creep and grain boundary sliding in antigorite, unrecognised at laboratory strain rates, may be of substantial importance to mantle wedge and subduction thrust rheology.

6.3 Methods

Cross-polarized transmitted light images and backscattered electron images of the microstructure were taken from polished thin sections cut approximately parallel to the XZ plane of the finite strain ellipsoid. Backscattered electron images were produced using a Zeiss Sigma field emission scanning electron microscope (SEM) in the School of Earth and Environmental Sciences, Cardiff University, Wales. The SEM was operated at a working distance of 8.9 mm using beam conditions 4.3 nA and 10 keV. Samples were coated with $\sim$ 10 nm of C to prevent charging. Raman spectra were collected from uncoated polished

thin sections to determine the serpentine polytype in a microstructural context, using an WITec Alpha 300R+ confocal Raman microscope in the Department of Chemistry, The University of Otago, New Zealand. Spectra were collected in the high-wavenumber region of serpentinite spectra (3600-3750 cm^{-1}), where chrysotile, lizardite, and antigorite polytypes produce distinct peaks. Analytical and data-processing methods followed those outlined in Rooney *et al.* (2018).

6.4 Outcrop observations

A well-exposed section of the NMR occurs near Mie (approx. 32.8203 °N, 129.7562 °E, WGS84). Here, outcrops show amphibolite, serpentinite, and minor metasediment intermixed in a broad ductile shear zone (Fig. 3.5). The studied exposures show a pervasive, intensely developed foliation in metasediment and amphibolite, while in serpentinite, the foliation is generally well-developed, but varies in outcrop from intensely developed to absent.

In general, foliations dip $\sim 20 - 50°$ to the south-east (Fig. 3.5d), with substantial scatter reflecting folding and deflection around contacts between lithologies with different competency (Fig. 3.5c). The term 'competency' is used here to indicate a relative viscosity on the basis of outcrop observations. Linear fabrics are difficult to recognise in the serpentinite, although lineation in the surrounding metamorphosed oceanic plate stratigraphy generally plunges gently to the south-west, approximately within the plane of foliation in serpentinite. S/C type foliation geometries and lineation on C-planes in amphibolite (Fig. 3.5d, also Ujiie *et al.* (2021)), and S/C type foliation geometries in serpentinite (Fig. 6.1c), are consistent with non-coaxial strain with a top-to-south shear sense.

In the west of the mapped area, a lens of serpentinite with a structural thickness $\sim$ 130 meters occurs within amphibolite (Fig. 3.5d). The other dimensions of the lens are unclear because of the limited spatial extent of the outcrop; however, other serpentinite lenses elsewhere in the NMR show similar widths, and lengths up to 1 km (Fig. 3.5a). Serpentinite, despite appearing mineralogically uniform in outcrop, contains more competent lenses within a matrix, which locally shows a scaly fabric (Fig. 6.1a, 6.1b, 6.1c). Competent serpentinite lenses show a less intensely developed foliation relative to adjacent

serpentinite (Fig. 6.1a,b).

At a scale of tens of meters, foliation in the serpentinite lens is generally subparallel to foliation in the adjacent amphibolite (Fig. 3.5d), however, at smaller scales (e.g. Fig. 6.1b, 6.1e) the foliation is highly irregular, and wraps around blocks of serpentinite with poorly-defined foliation. Magnesite veins, commonly rimmed by amphibole, both obliquely cross-cut and lie parallel to the serpentinite foliation. Veins of splintery serpentine, typically rimmed by magnesite-amphibole mixture (Fig. 6.1f), are also both oblique and parallel to the foliation. Laths of serpentinite within splintery veins are commonly inclined to the vein margin, suggesting a mixture of extension and shear strain.

6.5 Microstructure of serpentinite

Away from fractures and veins, the serpentinite contains only minor magnesite, talc and ilmenite (estimated $< 2\%$). The dominant microstructure is an anastomosing, variably developed foliation trace defined by optically aligned serpentine (Fig. 6.2a). Thin sections show a spectrum of microstructures between non-foliated and intensely foliated serpentine, where anastomosing layers of foliated serpentine envelop lenses where the foliation is absent or less intense (Fig. 6.2a). In general, changes in the intensity of the foliation are gradual and progressive. However, along the margins of poorly foliated lenses, the intensity of the foliation generally changes abruptly (e.g. Fig. 6.2a, 6.3).

Non-foliated serpentinite contains fan-shaped aggregates of serpentine grains arranged in an interpenetrating texture where there is no clear preferred cleavage plane orientation (Fig. 6.2c). This texture is characteristic of antigorite (e.g., Hirauchi *et al.*, 2010; King *et al.*, 2003; Rouméjon *et al.*, 2019; Williams, 1979). In non-foliated serpentinite, serpentine grains are mostly euhedral and typically $< 1\mu$m wide and < 50 μm long (Fig. 6.2c).

Where the foliation is present but poorly developed, the microstructure consists of poorly foliated serpentine interleaved with anastomosing layers of well-foliated serpentine (Fig. 6.2b). Serpentine grains within poorly foliated serpentinite are commonly indented by neighbouring grains (Fig. 6.2e), and indentation microstructures are most common along grain boundaries characterised by high angles between neighbour cleavage planes.

The most intensely foliated serpentinite contains euhedral grains with well

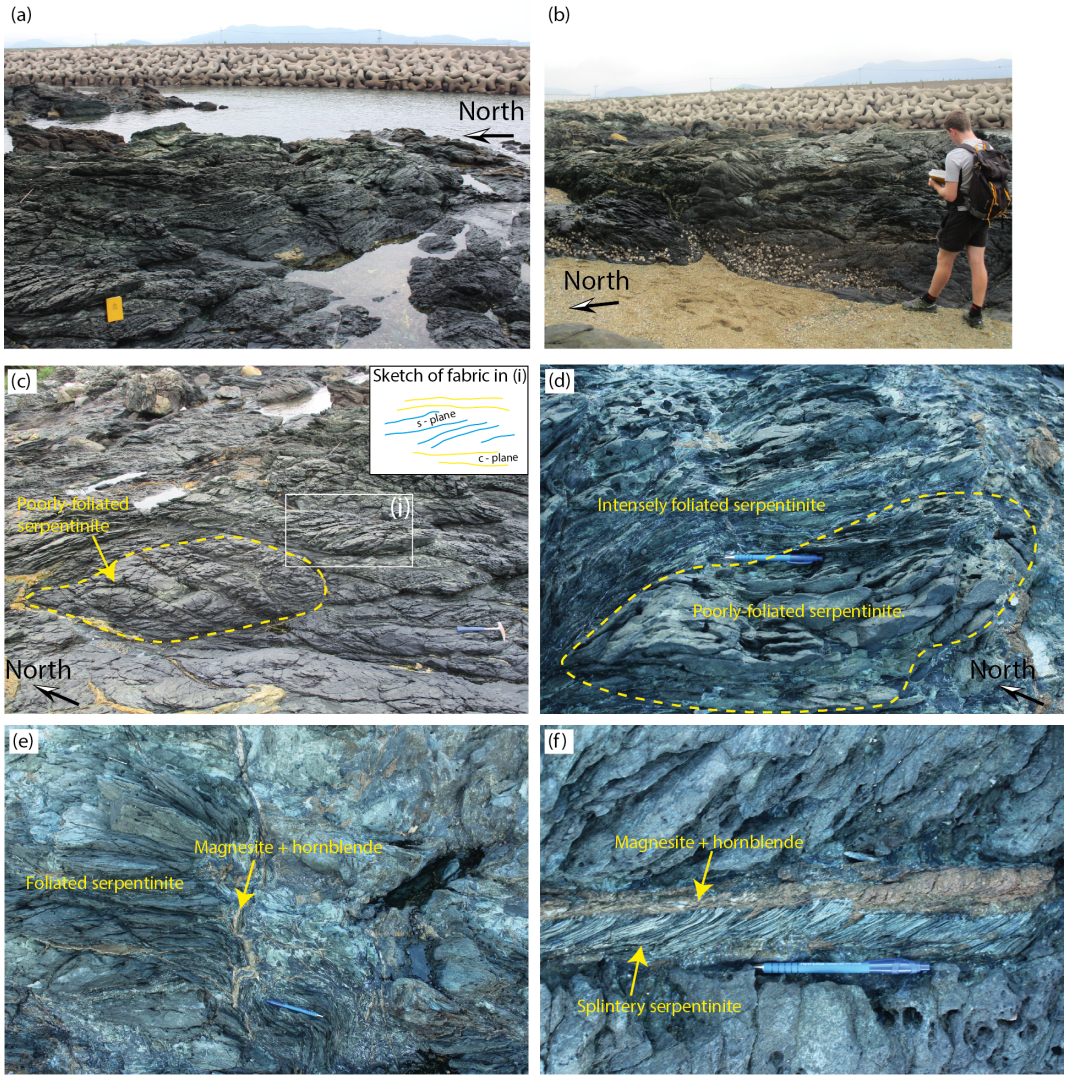

Figure 6.1: Outcrop photographs showing typical structures in serpentinite. (a, b) Views of the serpentinite outcrop showing the scaly and often chaotic nature of the foliation. (c, d) Lenticular blocks of poorly foliated serpentinite within a more intensely foliated matrix. Foliation in serpentinite adjacent to the block in (c) shows S-C geometry consistent with top-to-south shear. (e) Magnesite-hornblende veins generally occur subparallel to foliation, but locally crosscut the foliation. (f) Splintery-textured serpentinite vein rimmed by dolomite and hornblende, obliquely cross-cutting foliation. Serpentinite laths are inclined to the vein margin implying hybrid tensile-shear failure.

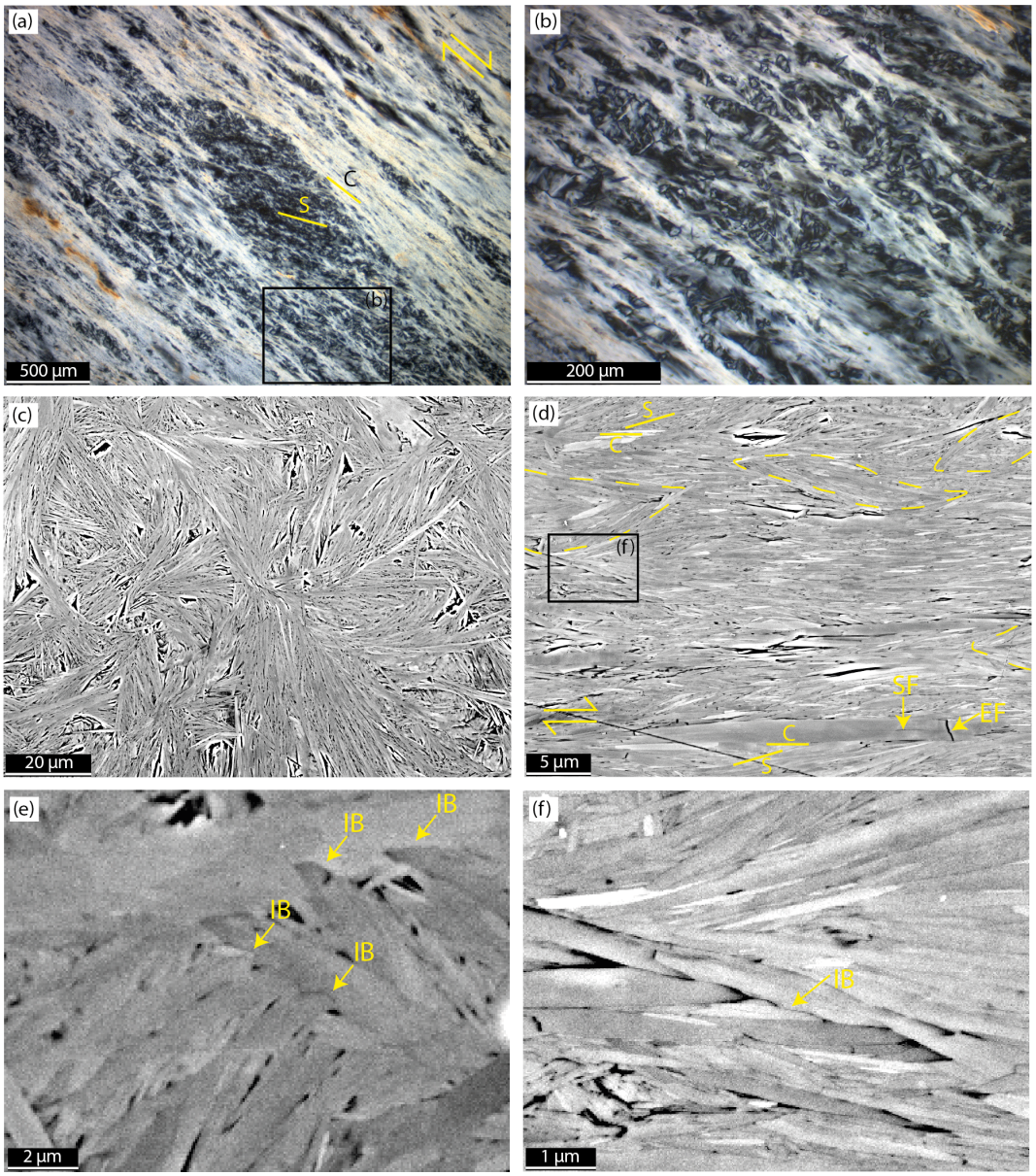

Figure 6.2: Cross-polarised light images (a, b) and back-scattered electron images (c-f) showing microscale fabrics in serpentinite. (a) Typical microstructure of serpentinite; phacoids of poorly foliated serpentinite within a more intensely foliated matrix. Rectangle shows the location of (b). (b) Moderately foliated serpentinite near the margin of the phacoid in (a). (c) Typical microstructure of non-foliated serpentinite. (d) Typical microstructure of intensely foliated serpentinite. Large grains show extension fractures (EF) and shear fractures (SF). Rectangle shows the location of (f). (e) Neighbour grains in poorly foliated serpentine show locally indented grain boundaries (IB). (f) Subtle indentation of neighbouring grains in intensely foliated serpentinite.

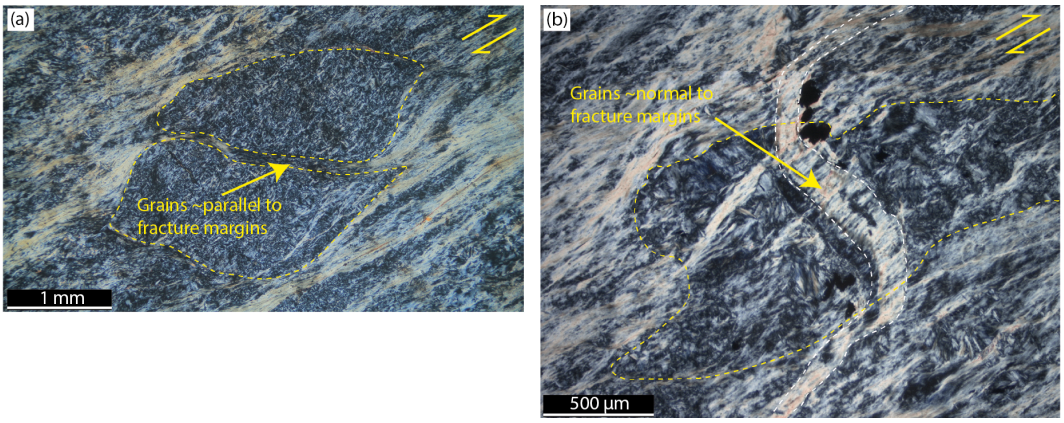

Figure 6.3: Brittle failure of competent poorly foliated lenses (a) Fractured lens of poorly foliated serpentinite within a more intensely foliated matrix. Note the intense foliation immediately adjacent to the lens. (b) Serpentinite vein cross-cutting a poorly foliated lens and deflected along foliation planes in the adjacent more intensely foliated matrix. In both cases, the fractures accommodate extension of the lenses parallel to the local foliation.

aligned cleavage planes (Fig. 6.2d). Grains are typically < 0.5 μm wide and < 20 μm long; finer than in areas where the foliation is less intense. In places, intensely foliated serpentinite shows a subtle scaly geometry. Like in poorly foliated serpentine, grains in intensely foliated serpentinite show indented boundaries (Fig. 6.2f), although indentation of neighbouring grains is less frequently observed in the most intensely foliated serpentinite. Large grains within intensely foliated serpentinite (Fig. 6.2d), contain tensile microfractures oriented oblique to the grain long axis indicating foliation-parallel extension. Shear fractures also occur, parallel to cleavage planes and grain long-axes.

Lenses of poorly to non-foliated serpentinite within more intensely foliated serpentinite commonly contain fractures (Fig. 6.3). Fractures in poorly foliated serpentinite lenses show opening directions approximately parallel to long-axis of the lens, indicating foliation-parallel extension. Fracture planes are generally at a high angle to the incipient foliation in lenses (Fig. 6.3), suggesting that during fracturing, σ_1 within the lens was at a high angle to the bulk foliation orientation. Generally, lenses that contain fractures show a strong contrast in fabric type across the lens-matrix margin (e.g. Fig. 6.3a). Veins that cut poorly foliated lenses and extend into more intensely foliated matrix (e.g. Fig. 6.3b) appear relatively intact within the lenses, but are thinned and deflected parallel to the foliation in the matrix.

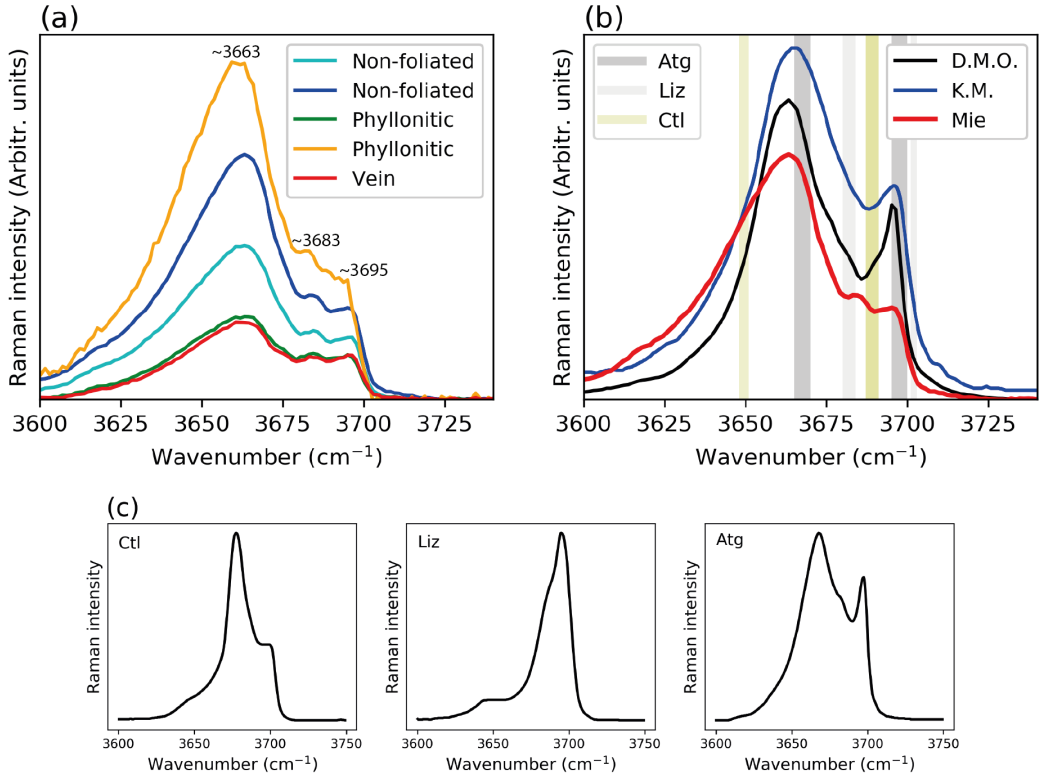

Figure 6.4: Raman spectra from serpentinite in the study area and reference antigorite samples. (a) Spectra and peak positions for non-foliated, phyllonitic and vein serpentinite from the study area. (b) Comparison between a representative spectrum from Mie serpentinite, a spectrum obtained from an antigorite reference sample from the Dun Mountain Ophiolite (D.M.O.) (Tarling *et al.*, 2019), and the antigorite spectrum presented in Petriglieri *et al.* (2015), from the Koniambo Massif (K.M). Vertical lines show the range of peak positions previously reported for antigorite (Atg), lizardite (Liz), and chrysotile (Ctl), based on the compilation in Rooney *et al.* (2018). (c) Typical shapes of lizardite, chrysotile, and antigorite spectra, modified from Rooney *et al.* (2018).

6.6 Raman spectra analysis

Non-foliated and intensely foliated serpentine, and serpentine veins, show similar Raman spectra (Fig. 6.4a). The shape of the spectra does not vary between fabric types and is similar to the shape of previously analysed antigorite spectra (Fig. 6.4b); although, compared to published antigorite spectra and reference antigorite samples analysed during the same analytical session, these spectra lack a prominent trough near 3687 cm^{-1}.

In the analysed samples, the strongest peak is consistently centred near 3663 cm^{-1} (Fig. 6.4a). Two smaller peaks with similar intensities appear near 3683 cm^{-1}, and 3695 cm^{-1}. The strongest peak in the studied samples, near

3663 cm^{-1}, occurs at slightly lower wavenumber than the strongest peak in previously analysed antigorite samples, which occurs between 3665-3670 cm^{-1}. The peak near 3695 cm^{-1} is within the range of positions between 3695-3700 cm^{-1} reported for the smaller antigorite peak in the high wavenumber region. The peak near 3683 cm^{-1} is close to a lizardite peak which occurs in the range 3683-3684 cm^{-1} (Rooney *et al.*, 2018); however, a shoulder near 3701-3703 cm^{-1} is present in lizardite spectra but not in spectra from Mie serpentinite. None of the observed spectra show shapes or peak positions consistent with chrysotile.

Electron images of serpentine grains (e.g. Fig. 6.2e, f) show no variation in mineral habit which might reflect intergrowth of different minerals or serpentine polytypes, so this seems an unlikely explanation for the unusual spectra shape. We infer that the Mie serpentine is the antigorite polytype (as also suggested by Hirauchi *et al.*, 2020), based on Raman spectra in the low-wavenumber region), but has a slightly different chemical structure than previously analysed antigorite. Overall, Raman spectra suggest that the Mie serpentinite is the antigorite polytype, and imply that there is no variation in polytype between the fabric types.

6.7 Foliation development in antigorite

Non-foliated antigorite with an interpenetrating texture has previously been interpreted to develop during either hydration of olivine or prograde metamorphism of mesh-textured lizardite serpentine (Boudier *et al.*, 2010; O'Hanley, 1991; Wicks and Whittaker, 1977). The near-isometric interpenetrating microstructure of non-foliated antigorite (Fig. 6.2c) suggests antigorite formed under static conditions (Maltman, 1978; Morales *et al.*, 2018). Thermomechanical models of subduction zones (e.g., Abers *et al.*, 2006; Syracuse *et al.*, 2010; Wada *et al.*, 2008), and the distribution of shear wave anisotropy (indicating elastic anisotropy perhaps relating to deformation) from active subduction zones (Currie *et al.*, 2004; Uchida *et al.*, 2020) indicate that a shallow portion of the mantle wedge is decoupled from the slab. Consequently, the nose of the mantle wedge provides a relatively static environment for serpentinisation (Wada *et al.*, 2008). We infer that the interpenetrating fabric in Mie serpentinite developed under static conditions, potentially in a hydrated mantle

wedge.

The foliation and sense of shear are consistent between the serpentinite and the adjacent amphibolite, implying that the serpentinite deformed together with amphibolite. Hornblende, defining the lineation in adjacent amphibolite, is thermodynamically stable at > 500 °C (Section 4.7) suggesting antigorite and amphibolite deformed together at near peak metamorphic conditions. Raman spectra obtained from carbonaceous material in metapelite indicate peak metamorphism of the NMR occurred at 440 °C - 550 °C (Mori *et al.*, 2019; Ujiie *et al.*, 2021), consistent with the hornblende lineation in amphibolite. The mixing of slab and mantle lithologies suggests the NMR represents a broad shear zone deformed near the slab-mantle boundary. Within the serpentinite, there are no clear indications of retrograde metamorphism. Magnesite and serpentinite veins, some of which are deformed along the foliation, are interpreted to be related to subduction, although non-deflected veins may relate to exhumation. Isometric actinolite rims around hornblende grains in amphibolite suggest the prograde structures experienced little change during exhumation. The study area may have experienced some amount of bulk rotation during exhumation, but this should not change the relative orientations of structures developed during subduction.

S/C foliation geometries in poorly foliated (Fig. 6.2a), and intensely foliated (Fig. 6.2d) serpentinite imply that non-coaxial strain, consistent with subduction thrust deformation, accompanied all stages of fabric development. The development of foliation requires rotation of interpenetrating grains towards a common orientation that aligns basal planes, a process potentially driven by non-coaxial strain (Escher and Watterson, 1974; Haines *et al.*, 2013; Ramsay, 1980). Naturally deformed antigorite commonly shows a strong preference for aligned (001) planes (Katayama *et al.*, 2009; Nagaya *et al.*, 2017; Van de Moortéle *et al.*, 2010), reflecting the highly anisotropic mechanical properties of phyllosilicate minerals (Hansen *et al.*, 2020; Kronenberg *et al.*, 1990).

Rotation of intensely interpenetrating grains towards a common orientation requires changing the shape of individual grains (Fig. 6.5). Mineral-scale deformation is accomplished by the most efficient of three main mechanisms, each favoured at different environmental conditions (e.g., Knipe, 1989); (1) fracturing and frictional sliding, (2) the movement of dislocations (e.g., glide,

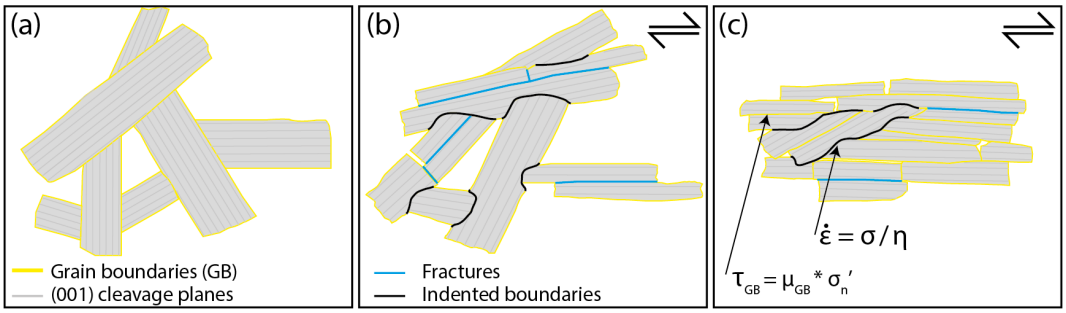

Figure 6.5: Schematic diagram showing the inferred microstructural evolution during non-coaxial strain. (a) Pre-deformation (b) Incipient strain. Grains rotate towards the regional shear plane and sliding occurs along grain boundaries. Strain incompatibilities are resolved by pressure solution, and fracturing which contributes to a reduced grain size. (c) Increased strain results in a more intense foliation. In (b) and (c), grain boundary sliding occurs above a critical shear stress τ_{GB} determined by grain boundary friction μ_{GB} and effective normal stress $\sigma_n^{'}$. The strain rate for pressure solution depends on the applied stress, and a viscosity term η, which encompasses parameters relating to dissolution and precipitation kinetics.

kinking, subgrain formation), and (3) dissolution and precipitation. Fracturing and frictional sliding are suppressed by confining pressure, and depend on friction, and the cohesive and tensile strengths of minerals (Byerlee, 1968; Paterson and Wong, 2005; Robertson, 1955). The effectiveness of strain by dislocation movement depends on temperature, strain rate, and material parameters (Poirier, 1985). Strain by dissolution-precipitation depends on driving stresses (and related strain rates), as well as dissolution and precipitation kinetics (Gratier *et al.*, 1999; Raj and Ashby, 1971; Rutter, 1976).

Poorly foliated serpentinite shows indications of dissolution-precipitation by pressure solution creep, where grains at high angles to the foliation locally indent grains parallel to the foliation (Fig. 6.2e, f). Other naturally deformed antigorites also show indications of pressure solution creep, such as precipitation in strain shadows behind interstitial non-serpentine grains (Wassmann *et al.*, 2011) and recrystallisation along intragranular fractures (Auzende *et al.*, 2015, 2006). Antigorite veins deflected along the foliation (Fig. 6.3b) provide evidence for precipitation during foliation-forming deformation, perhaps dissolved during pressure solution. Pressure solution creep coupled to grain boundary sliding is a composite deformation mechanism commonly inferred to drive fabric development in phyllosilicate-rich fault rocks (e.g., Bos and Spiers, 2002; Fagereng and den Hartog, 2017; Imber *et al.*, 2001).

The smaller grain size of foliated serpentine, compared to non-foliated ser-

pentine, indicates that fabric development was accompanied by grain size reduction. Large grains in intensely foliated serpentinite are cut by intragranular fractures both parallel and orthogonal to the cleavage (Fig. 6.2d), indicating brittle fracturing contributes to grain size reduction. Other mechanisms such as conjugate glide along (101) and ($1\bar{0}1$) planes (Amiguet *et al.*, 2014), subgrain formation (Auzende *et al.*, 2015; Padrón-Navarta *et al.*, 2012), or precipitation of smaller grains, might also contribute to reduce the grain size. In poorly foliated antigorite, moderately common anhedral grains might reflect precipitation, but these are generally larger than the volumetrically dominant euhedral laths. Additionally, we do not see grain boundaries offset along conjugate glide planes, suggesting that mechanism does not operate in NMR antigorite. While we do not observe indications of dislocation motion, such as kinking, subgrains, bulging grain boundaries, or offsets along conjugate glide planes, some contribution from dislocation motion cannot be ruled out entirely. However, the lack of slip systems in antigorite prohibits distributed deformation by dislocation motion (Chernak and Hirth, 2010) in the absence of a recrystallisation mechanism, such as dissolution-precipitation. Overall, we infer that a composite mechanism involving sliding along grain boundaries and pressure solution creep (Fig. 6.5) accommodates the transition from non-foliated to foliated antigorite.

6.8 Mixed brittle-ductile behaviour

The evolution from non-foliated to foliated textures, inferred to occur with progressive non-coaxial strain, suggests that lesser finite strains were achieved in less poorly foliated lenses, relative to the matrix. Less deformed poorly foliated lenses within a more intensely deformed and foliated matrix implies imply a competency contrast between lenses and the matrix. Fibre loading theory (e.g., Lloyd *et al.*, 1982; Zhao and Ji, 1997), demonstrates that matrix stresses are amplified in relatively competent inclusions, such as poorly foliated antigorite lenses within a more intensely foliated antigorite matrix, and that the magnitude of the stress amplification is dependent on the competency contrast between lenses and the matrix. Fibre loading theory also demonstrates that the greatest degree of stress amplification occurs at the centre of a more competent lens (Fagereng, 2013), consistent with the observation that fractures

generally cut through the centre of poorly foliated lenses (Fig. 6.3).

The orientation of the stress field is expected to refract across a competency contrast (Beall *et al.*, 2019b; Strömgård, 1973), with greater degrees of refraction occurring across greater competency contrasts (Fagereng, 2013). If the angle between σ_1 in the matrix and the lens boundary is $> 45°$, then σ_1 in the lens will refract toward the normal to the lens long-axis, favouring foliation-parallel extension (e.g. Fig. 6.3b). Conversely, if the angle between σ_1 in the matrix and the lens boundary is $< 45°$ the stress field will rotate to favour foliation-normal extension (Fagereng, 2013; Strömgård, 1973). In Mie serpentinite, extension fractures occur at high angles to the lens long-axis, suggesting local σ_1 in the matrix is $> 45°$ to the adjacent lens long-axis, and to the bulk foliation. Extension-fracturing of the lenses suggests that σ_3 within the lens is negative, consistent with numerical models of strong inclusions deforming in a weak matrix Beall *et al.* (2019a); Wilson *et al.* (2009).

Gradients in stress and strain rate magnitudes across lens margins suggest that strain should localise within the matrix adjacent to lenses (e.g., Masuda and Ando, 1988; Wilson *et al.*, 2009). This is reflected in Fig. 6.3a, where intense foliation occurs locally along a lens margin. Amplification of matrix stresses within lenses may be sufficient to generate fracturing of the lenses, without externally imposed variations in fluid pressure or strain rate (Beall *et al.*, 2019b). Short term variations in differential stress (and associated strain rates), or variations in pore fluid pressure may also have driven episodic fracturing of the serpentinite, independent of local viscosity contrast effects. Cyclic changes in strain rate, permeability, and fluid pressure associated with repetitive slow slip events (Gosselin *et al.*, 2020; Schwartz and Rokosky, 2007; Warren-Smith *et al.*, 2019), considered to take place near the mantle wedge corner in several locations (Brown *et al.*, 2009; Matsubara *et al.*, 2009; McCrory *et al.*, 2014), could also impose stress and fluid pressure variations within the serpentinite, perhaps generating cyclic episodes of brittle failure. On the other hand, transient slow slip events may begin within the serpentinite, potentially driven by the transient development and destruction of force chains comprised of relatively viscous lenses of poorly foliated serpentinite (Beall *et al.*, 2019b).

6.9 Rheology of antigorite

Serpentinites deformed to high strains in the laboratory show strengths that evolves substantially with strain and foliation development. (Chernak and Hirth, 2010) deformed poorly foliated antigorite and powdered antigorite by axial compression at 0.85 -1.5 GPa, to axial (flattening) strains up to 46%. Experiments within the temperature window 400-625 °C, close to the metamorphic temperature of the NMR, showed initial strain-hardening up to axial strains $\sim 5-10\%$, followed by substantial weakening. Recovered samples show localised shear zones containing fine-grained, foliated antigorite, which is inferred to host strain after the initial strain-hardening phase. Our observations and the experimental results of (Chernak and Hirth, 2010) are both consistent with a serpentine rheology that is strongly dependent on fabric intensity and orientation relative to the stress field, as observed experimentally for other rocks dominated by phyllosilicates (Collettini *et al.*, 2009; Holyoke and Tullis, 2006; Kronenberg *et al.*, 1990).

To explain observations of distributed deformation (Fig. 6.5a), aligned grain boundaries (Fig. 6.5d), and localised dissolution (Fig. 6.5e, 6.5f), initial antigorite foliation development in the NMR is inferred to be accomplished by pressure solution creep and sliding along grain boundaries (Fig. 6.5). In NMR antigorite, the inferred strain progression from non-foliated to foliated fabrics results in the alignment of basal planes, which represent the mechanically weakest planes in antigorite (Hansen *et al.*, 2020). Antigorite with more intensely aligned grains presents less obstacles to sliding along foliation planes (Fig. 6.5), potentially resulting in grain boundary sliding accommodating more of the strain in intensely foliated antigorite, relative to in poorly foliated antigorite. In this case, pressure solution, the initially dominant deformation mechanism may be less dominant under high strain conditions; a conclusion also reached by Holyoke and Tullis (2006), who deformed biotite-quartz-plagioclase gneiss. Overall, antigorite in the NMR is inferred to deform by a combination of grain boundary sliding and pressure solution creep.

Recent experiments provide some insight into intracrystalline deformation and grain boundary sliding. Hansen *et al.* (2020) showed that room-temperature nanoindentations of antigorite produced shear microfractures along (001) planes, and did not cause measurable distortion of the crystal lattice, sug-

gesting dislocation processes were not active at these experimental conditions. Idrissi *et al.* (2020) generated tensile strain of antigorite within a transmission electron microscope (TEM), allowing in-situ observation of atomic-scale processes during deformation at room temperature under high vacuum (i.e. no confining pressure) conditions. In these experiments, antigorite deforms by sliding along (001) grain boundaries, consistent with previous experimental studies (David *et al.*, 2018; Escartín *et al.*, 1997; Hansen *et al.*, 2020), and our interpretation of grain boundary sliding coupled to pressure solution creep. In-situ TEM analysis by Idrissi *et al.* (2020) showed dislocations within the sample did not move during deformation, despite Schmidt factor analysis indicating shear stresses of several hundred MPa resolved on dislocation glide planes. Rather, shear microcracking along (001) occurred adjacent to grain boundaries, consistent with deformation accommodated by grain boundary sliding. Permanent strains in response to slow loading rates were greater than permanent strains generated in response to faster loading rates, implying a rate-dependent mechanism facilitates grain boundary sliding. This result may relate to the velocity-strengthening behaviour shown by antigorite in experiments at low sliding velocities (Chernak and Hirth, 2010; Reinen *et al.*, 1991). Sliding along grain boundaries is expected to follow Amonton's law, such that for sliding to occur, the shear stress resolved on the grain boundary (τ_{GB}) must exceed $\tau_{GB} = (\mu\sigma_n^{'})$+C , where $\sigma_n^{'} = \sigma_n - P_f$, μ is a friction coefficient, $\sigma_n^{'}$ is the effective normal stress, σ_n is the applied normal stress, P_f is the pore fluid pressure, and C is cohesion.

Pressure solution creep is a linear-viscous mechanism (Raj and Ashby, 1971), where the deformation rate ($\dot{\epsilon}$) is controlled by the effective normal stress gradient $\sigma_n^{'}$, which may relate to the differential stress, and a viscosity term (η), combined in a simplified flow law of the form $\dot{\epsilon} = \sigma_n^{'}/\eta$ (e.g., Gratier *et al.*, 1999; Raj and Ashby, 1971). The viscosity term η represents various parameters relating to the kinetics of material dissolution, transportation and precipitation, which, for a given material, are proportional to temperature and inversely proportional to grain size (Raj and Ashby, 1971; Rutter, 1976). Overall, experimental results (Idrissi *et al.*, 2020; Reinen *et al.*, 1991) and theoretical considerations (Raj and Ashby, 1971) indicate that the composite mechanism of pressure solution and grain boundary sliding produces strengths dependent on strain rate.

Where strain rates and associated deviatoric stresses are sufficiently low so that pressure-solution creep enables grain boundary sliding, we envisage this mechanism to operate though all stages of fabric development. Towards higher strain rates, or conditions where pressure solution creep is less efficient, we expect strengthening of antigorite and increased activity of mechanisms which require higher stress (see Fig. 2.6), such as fracturing or dislocation motion. Theoretically, the pressure solution mechanism is able to operate at infinitesimally small differential stresses (Raj and Ashby, 1971; Rutter, 1976), whereas the motion of dislocations along a particular slip system requires a critical shear stress to be imparted on the slip system in order to overcome lattice resistance to slip (Schmid, 1928; Schmid and Boas, 1935; Wenk and Christie, 1991). While estimates of the critical shear stress for sliding along any of the inferred slip systems in antigorite are lacking, glide parallel to (001) in the phyllosilicates muscovite (Basu *et al.*, 2009) and biotite (Kronenberg *et al.*, 1990) requires resolved shear stresses between 20-80 MPa. In antigorite, periodic reversals of the tetrahedral layer results in the two inferred slip systems $[10\bar{1}](101)$ and $[101](10\bar{1})$ having a stepped geometry (Amiguet *et al.* (2014), their Fig. 9). Compared to glide along (001) in other phyllosilicates, the stepped geometry of the slip systems in antigorite might require critical resolved shear stresses greater than those in muscovite and biotite. Dislocation glide, observed in experimentally deformed serpentinite (Amiguet *et al.*, 2014) and subgrain formation, observed in naturally deformed, relatively coarser grained antigorite exhumed from slightly higher metamorphic grades (1.6-1.9 GPa and 680-710 °C; Padrón-Navarta *et al.*, 2012) may contribute to deformation at higher deviatoric stresses.

Such transitions from pressure-solution creep to dislocation creep with increasing strain rate have been previously suggested for rocks deforming at variable strain rates (Bos and Spiers, 2002; Niemeijer, 2018; Rutter, 1976). Increasing grain size, or changes to the kinetics of dissolution and precipitation may also drive a change in the dominant deformation mechanism. While these examples show that dislocation creep occurs in antigorite under some conditions, we emphasise that our microstructural observations and inference of low differential stress, and high fluid pressure conditions in the NMR, analogous to subduction zone, mantle wedge environments, suggest deformation by pressure solution creep and grain boundary sliding. We infer that the rheology of

antigorite in the NMR contains a linear-viscous component (pressure solution) and a frictional component (grain boundary sliding), and that the strength of antigorite is proportional to strain rate (related to the deviatoric stress), and inversely proportional to temperature, grain size, and fluid pressure.

Antigorite deformed in experiments at $>\sim 300$ °C and confining pressures > 200 MPa generally shows sharp transitions in fabric type between foliated and non-foliated fabrics (Chernak and Hirth, 2010; French *et al.*, 2019; Gasc *et al.*, 2017; Hirauchi *et al.*, 2020; Proctor and Hirth, 2016), contrary to the gradual transitions typically preserved in naturally deformed antigorite (Fig. 3a; Hermann *et al.*, 2000; Hirauchi *et al.*, 2010; Wassmann *et al.*, 2011; Williams, 1979). French *et al.* (2019) infer that, in antigorite deforming at laboratory strain rates, incipient strain drives shear microcracking and kinking, locally increasing the surface area exposed to pressurised fluids without substantially reducing fluid pressure. This process reduces the effective normal stress, which results in localised frictional shear failure acting to align the mechanically weak basal planes. At natural strain rates, pressure solution would act to maintain or increase the area of grain-to-grain contact during deformation, and thereby suppress this localised brittle deformation. This may explain why the naturally deformed serpentinite we describe here generally shows dominantly gradual transitions in fabric type, compared to the abrupt transitions in experimentally deformed serpentinite.

6.10 Viscosity contrast between ocean plate and mantle lithologies

Chapters 5 and 4 have shown that hydrated oceanic crust and subducted sediments in the NMR deformed by dissolution-precipitation creep of non-phyllosilicates (albite, quartz, amphibole), coupled to sliding along muscovite and chlorite foliations. This allowed frictional-viscous flow in these rocks, at low differential stresses (Section 5.6), as also interpreted in other shear zones shown to be weak in nature (Imber *et al.*, 2001; Wallis *et al.*, 2015; Wintsch and Yeh, 2013) and experiment (Bos and Spiers, 2002; den Hartog and Spiers, 2014; Niemeijer and Spiers, 2005). Lenses of antigorite within metamorphosed oceanic stratigraphy, and foliation in the oceanic stratigraphy wrapping serpentinite lenses implies that antigorite is more viscous than ocean plate stratigra-

phy, at least at the mantle wedge conditions preserved in the NMR. Decoupling between the slab and the mantle, as suggested by thermomechanical models (e.g., Wada *et al.*, 2008), requires a mechanically weak layer separating the subducting plate and overriding anhydrous mantle. Our results imply that serpentinite, commonly inferred to facilitate decoupling between the oceanic plate and the mantle (Gerya *et al.*, 2002; Hilairet and Reynard, 2009) may, at least under some conditions achieved in natural subduction zones, be more viscous than juxtaposed ocean plate lithologies that deform by dissolution-precipitation creep and sliding along muscovite and chlorite foliations. Plate interface strain may therefore be preferentially localised in ocean crust lithologies, rather than in the mantle wedge.

6.11 Conclusion

The NMR records plate boundary deformation in subducted sediment, hydrated oceanic crust, and serpentinite. Serpentinite preserves microstructural evidence for deformation predominantly by dissolution-precipitation creep, which we infer accommodated strain-rate and grain-size dependent deformation coupled to grain boundary sliding. Development of the serpentinite foliation was accompanied by non-coaxial strain, and viscosity decreased with increasing strain, as a result of increased foliation intensity and grain size reduction. Poorly foliated antigorite forms relatively competent lenses within a less competent, intensely foliated matrix, resulting in amplification of matrix stresses within the lenses. Local stress amplifications or externally imposed strain rate or pore fluid pressure variations may cause local, brittle failure within the otherwise ductility deforming serpentinite. Finally, outcrop observations imply that at some natural plate boundary conditions, antigorite may be more viscous than hydrated and metamorphosed ocean plate stratigraphy.

Chapter 7

General discussion

Chapters 4, 5 and 6 have presented work from three exposures of exhumed Late Cretaceous shear zones on Kyushu, SW Japan. These shear zone exposures show structures consistent with shearing along the convergent eastern Eurasian margin in the Late Cretaceous, and largely retain a prograde metamorphic mineral assemblage (Chapters 3 and 4). On Kyushu, from east to west the exposures increase in metamorphic grade, from the prehnite-pumpellyite to greenschist facies transition, to the greenschist-amphibolite facies transition. Together, the exposures reflect a transect down-dip along the subduction plate interface at temperatures where mixed slip styles are inferred to occur along active margins (Chapter 2). A combination of outcrop and thin-section observations, isotope analysis, and thermodynamic modelling, has given insight into the rheology of the plate boundary shear zone, and it's constituent lithologies. The overall aim of this work was to investigate the geology and geodynamics of subduction plate boundaries at conditions where slow slip and tremor occur down-dip of the seismogenic zone, in particular addressing the following questions:

Q1: What types of structural fabrics (i.e. fractures, foliations) are present, what are their orientations, and how are they distributed between lithologies and metamorphic grades?

Q2: What lithologies occur within the plate boundary shear zone, and how is strain distributed between these lithologies?

Q3: What is the state of stress within the plate boundary shear zone across the base of the seismogenic zone?

Q4: What are the dominant grain-scale deformation mechanisms within the plate boundary, what is the likely mechanical behaviour of the shear zone, and how does it vary with depth?

Q5: How do hydrous fluids influence deformation style?

Q6: How, and where, might frictional instabilities arise down-dip of the base of the seismogenic zone?

The intention of this Chapter is to bring together the findings of Chapters 4, 5 and 6 to address the questions above, and outline the implications for active margins. This will be followed by conclusions in Chapter 8, summarising the main findings and their implications, and some suggestions for further work.

Q1: What types of structural fabrics (i.e. fractures, foliations) are present, what are their orientations, and how are they distributed between lithologies and metamorphic grades?

If quartz veins reflect discontinuous brittle fracturing events, and foliation develops during continuous ductile shear, then the distribution of these features between the studied shear zone exposures should reflect the distribution of slip style over the range in P and T conditions from which the exposures were exhumed. All of the studied exposures show penetrative foliations in hydrated oceanic crust, metasediment, and, for the amphibolite facies example, serpentinite (Figs. 4.4, 4.5, 4.6, 6.2). In the Makimine mélange, where ocean plate stratigraphy and lithological layering are generally preserved (Fig. 3.4), penetrative foliations are generally subparallel to lithological layering (Figs. 3.4, 4.2). In the NMR, ocean plate stratigraphy is not preserved, (Fig. 3.5) and the anastomosing foliation wraps around more competent lithologies.

Quartz veins, interpreted to have formed during the final stages of subduction-related deformation, locally overprint the inferred subduction-related foliation in coastal Makimine mélange (Fig 4.1) and in the NMR (Fig. 4.3). In coastal Makimine mélange, extension veins, distinguished by vein-normal opening vectors, occur in two sets; parallel and oblique to the foliation, while hybrid tensile-shear veins occur at a low angle to the foliation. Exposures of the inland Makimine mélange also show veins, but here, the veins are boudinaged (Fig. 4.2) and dismembered (Fig. 4.5) along the foliation, indicating that vein

formation was pervasively overprinted by a later episode of ductile deformation.

In metasediments and metabasalts from the NMR, veins either cut obliquely across the foliation, or lie subparallel to the foliation. Foliation-orthogonal veins show small degrees of ductile deformation consistent with the bulk shear sense (Fig. 4.3d). In serpentinite from the NMR, fractures and carbonate veins locally cross-cut the foliation (Fig. 6.1), but are also ductilely deflected along the foliation (Fig. 6.3), suggesting that, like in the oceanic lithologies, fracturing was followed by ductile shear. In shear zone exposures that show veins formed late in the subduction history, veins occur in all of the exposed lithologies, but are unevenly distributed between and within lithologies. In coastal Makimine melange, veins are intensely clustered within an area of the metasediment mélange unit (Fig. 3.4), while in the NMR, veins are more common along contacts between lithologies (Fig. 4.3). Overall, foliations are ubiquitous in all of the studied exposures, and quartz veins formed late in the subduction history are present in shear zone exposures exhumed from the base of the greenschist facies (coastal Makimine mélange) and the base of the amphibolite facies.

Q2: What lithologies occur within the plate boundary shear zone, and how is strain distributed between these lithologies?

The nature of the deforming material is a first-order control on shear zone strength and rheology. An important question is therefore: What are the rocks and minerals that constitute the plate boundary? Makimine mélange exposures show pelitic and psammitic metasediment, and hydrated oceanic crust. There is no exposure of the hanging-wall continental crust in the Makimine mélange. Exposures of the NMR also show pelitic and psammitic metasediment, and hydrated oceanic crust, as well as km-scale serpentinite lenses, interpreted as fragments of hydrated continental fore-arc mantle incorporated into the plate boundary shear zone.

Metasediments from all of the studied shear zones are dominantly composed of quartz, feldspar, muscovite and chlorite. Metabasalts from coastal Makimine mélange are dominated by albite, chlorite, and epidote (Fig. 4.4) Metabasalts from inland Makimine mélange are dominated by pyroxene, albite, chlorite, muscovite, actinolite, and epidote (Fig. 4.5), reflecting partial

equilibration of oceanic crust under fluid saturated prograde metamorphic conditions (section 4.7). Amphibolite from the NMR contains albite, hornblende, epidote, muscovite and chlorite (Figure 4.6). Serpentinite, present in the NMR, is dominantly antigorite serpentine (Fig. 6.4), and no anhydrous mantle minerals (e.g. olivines, pyroxenes) are present. Comparison between mineral assemblages preserved in the shear zones, and a P-T psuedosection for an inland Makimine mélange metabasalt composition (section 4.7, Fig. 4.7) suggests that the preserved mineral assemblages in metabasalt generally reflect equilibration or partial equilibration of oceanic crust to a hydrous, phyllosilicate-rich assemblage under fluid-saturated conditions during subduction.

Coastal and Inland exposures of the Makimine mélange, deformed at $\sim 328 \pm 30$ and $\sim 371 \pm 30$ (Ujiie *et al.* 2018; Ujiie *et al.* 2021) show hydrated metabasalt as boudains or layers showing pinch-and-swell geometry (Figures 4.1, 4.2). Boudinage or pinch-and-swell of metabasalt layers indicates that metabasalt was more viscous than metasediment. However, the low amplitude, long wavelength pinch and swell of metabasalt layers, especially in inland Makimine mélange (Figure 4.2), indicates the viscosity contrast between metabasalt and metasediment in Makimine mélange was subtle. In the NMR, metasediments and metabasalts are deformed together, and there is no pinch and swell or boudinage structure to indicate a viscosity contrast. This suggests that the viscosity contrast between hydrated oceanic crust and metasediment decreases with increasing metamorphic grade.

These observations imply that over the range of conditions represented by the studied shear zones, hydrated oceanic crust and metasediment have a similar viscosity, but, particularly towards lower metamorphic grades, metasediment is less viscous than metabasalt. In Chapter 5, a recrystallised grain size piezometer for quartz Cross *et al.* (2017) was applied to quartz veins deformed within the shear zones. Shear stress within metabasalt was estimated to be approximately 50-108 MPa in coastal Makimine mélange, and <12-35 MPa in the NMR. Fig. 5.6 shows that these strengths are far weaker than laboratory flow laws for 'fresh', unaltered oceanic crust (Mackwell *et al.*, 1998), and closer to strengths predicated by flow laws for micaceous sediments (Shea and Kronenberg, 1992). The primary conclusion of Chapter 5 is that the low strength of hydrous metabasalts, afforded by pressure solution creep and sliding along mechanically weak phyllosilicate foliations, allows hydrated oceanic

crust to accommodate a substantial proportion of plate-interface strain. The implication is that, particularly along sediment-starved margins (e.g., Mariania, Chile, Izu-Bonin; Clift and Vannucchi, 2004), the hydration state of the oceanic crust might have a strong influence on subduction thrust rheology in the viscous regime at the base of the seismogenic zone.

Chapter 6 pointed out that serpentinite lenses within NMR metasediment (mapped by Nishiyama (1989), Fig. 3.5a), and amphibolite (Fig. 3.5b), and observations of foliation in amphibolite wrapping around serpentinite, imply that NMR serpentinite has a greater viscosity than the adjacent metamorphosed ocean plate stratigraphy. The implication is that serpentinite, commonly inferred to facilitate decoupling between the oceanic plate and the mantle (e.g., Gerya *et al.*, 2002; Hilairet and Reynard, 2009; Wada *et al.*, 2008), and host tremor and slow slip (French and Zhu, 2017; Okazaki and Katayama, 2015), may, at least under some conditions achieved in natural subduction zones, be more viscous than juxtaposed ocean plate lithologies. Plate interface strain below the fore-arc mantle may therefore be preferentially localised in ocean crust lithologies, rather than in the mantle wedge.

Q3: What is the state of stress within the plate boundary shear zone across the base of the seismogenic zone?

As discussed in Section 2, and shown in Figs. 2.3 and 2.7, the state of stress within the plate interface shear zone is a critical control on the dominant deformation mechanism. Under low differential stresses and high confining pressures, fracturing and frictional sliding are suppressed in favour of thermally-activated viscous creep mechanisms. The presence of veins, themselves deformed by ductile thrust-sense shear, implies that the failure criteria for extension and extension-shear fracture were met, at least locally and temporarily. Extension veins require $(\sigma_1 - \sigma_3) < 4T_0$, while extension-shear veins form under differential stress conditions $> 4T_0$, within a small $(\sigma_1 - \sigma_3)$ range dependent on T_0. Assuming typical values for T_0 and μ, Fig. 4.10 (following Cox, 2010; Sibson, 1998) suggests that $(\sigma_1 - \sigma_3)$ and the effective vertical stress, during fracture opening, should be in the order of 10s of MPa. Chapter 5 suggested that quartz in inland Makimine mélange metasediment deformed at differentials stresses < 200 MPa and quartz in NMR amphibolite deformed at differential stresses < 60 MPa (Fig. 5.6b). In inland Makimine

mélange, boudinage of quartz veins within metasediment, and boudinage of metabasalt within metasediment in inland Makimine melange, suggests that the stress constraint $\sigma_1 - \sigma_3 < 200$ MPa approximately reflects the strength of metabasalt, and that differential stresses in metasediment should be lower. Quartz veins boudinaged within amphibolite in the NMR suggest that the quartz-based stress constraint $\sigma_1 - \sigma_3 < 60$ MPa is likely an overestimate of the strength of metabasalt, and the lack of indications of viscosity contrast between metasediment and metabasalt in the NMR suggests this may also be an overestimate of the maximum differential stress in metasediment. Particularly in the NMR, where the final stages of subduction-related strain are inferred to be accommodated by mixed brittle-ductile behaviour, these ambient differential stress estimates are consistent with the low differential stresses required to form extension and hybrid extension-shear fractures. Mutually crosscutting foliation-subparallel and foliation-oblique extension veins in coastal Makimine mélange suggest local and temporary rotation of the stress field between compressional and extensional regimes (Ujiie *et al.*, 2018). Crosscutting extension veins in the NMR (Fig. 4.3d) might reflect similar temporary rotations of the stress field, however, owing to ductile overprint, it is difficult to assess the initial orientation of the foliation-parallel veins.

Q4: What are the dominant grain-scale deformation mechanisms within the plate boundary, what is the likely mechanical behaviour of the shear zone, and how does it vary with depth?

At a given strain rate, temperature and pressure, the strength of a shear zone is dependent on the mineralogy, and also the dominant deformation mechanism (Knipe, 1989). Foliations in all of the lithologies in all of the studied shear zones are interpreted to develop by a composite mechanism involving (a) coaxial shortening orthogonal to σ_1 by pressure solution, and (b) sliding along phyllosilicate foliations. For a given material, the rate of pressure solution is principally dependent on temperature and grain size (Section 2.5.2). Sliding along grain boundaries should follow Eq. 2.11, and occur at a rate controlled by the frictional properties of the grain surface, and the effective normal stress. Sliding along mechanically weak phyllosilicate foliations, coupled to pressure solution creep of non-phyllosilicates, is commonly inferred to operate in subducted sediments and hydrated oceanic crust (e.g., Behr and Platt, 2013;

Fagereng and den Hartog, 2017; Palazzin *et al.*, 2016; Schwarz and Stöckhert, 1996; Wassmann and Stöckhert, 2013). A limited number of outcrop-based studies of antigorite serpentinite (Auzende *et al.*, 2006; Liu *et al.*, 2020; Wassmann *et al.*, 2011) have presented evidence for pressure solution creep, and Chapter 6 also provides further evidence for the likely importance of this deformation mechanism in antigorite at natural strain rates. The overall rheology is therefore a frictional-viscous rheology containing an approximately linear-viscous component relating to the pressure solution mechanism, and a frictional component relating to grain boundary sliding.

Experimental studies deforming mixtures of phyllosilicates and soluble interstitial grains (e.g. halite, quartz), (Bos *et al.*, 2000; Niemeijer, 2018; Niemeijer and Spiers, 2005) produce microstructures similar to those in Figs. 4.4, 4.5, and 4.6. In these experiments, strengths are strongly dependent on strain rate, and the frictional strength of the phyllosilicate phase. Microphysical models developed for frictional-viscous flow (e.g., Bos and Spiers, 2002; den Hartog and Spiers, 2014; Niemeijer and Spiers, 2005) allow extrapolation of this laboratory behaviour to natural strain rates, provided that constraints on frictional strengths and dissolution-precipitation kinetics exist. Extrapolation to natural strain rates in subduction contexts (e.g., Fagereng and den Hartog, 2017) shows that frictional-viscous flow in lithologies comparable to metasediments in the studied shear zones can accommodate typical plate convergence rates of a few cm per year at shear stresses of a few tens of MPa, when shear is distributed over a meters to hundreds of meters thick shear zone. These results are in good agreement with the low differential stresses suggested by the extension and extension-shear veins preserved in coastal Makimine mélange and the NMR. Most laboratory investigation of frictional-viscous flow has been focussed on metasediments, which are commonly assumed to control the strength and rheology of the plate interface (Behr and Becker, 2018; Shreve and Cloos, 1986; Sobolev and Brown, 2019). However, Sections 4.9 and 5.5, and 6.7 show that a frictional-viscous flow mechanism also operates in hydrated oceanic crust and antigorite serpentinite. However, a lack of constraints on pressure solution kinetics has restricted the development of microphysical models for frictional-viscous flow in these lithologies.

Overall, the dominant grain-scale deformation mechanism in all lithologies, in all of the studied shear zones, is a mechanism involving pressure

solution creep and sliding along grain boundaries. Laboratory studies (e.g., Bos *et al.*, 2000; Niemeijer, 2018), microphysical models (e.g., Bos and Spiers, 2002; Niemeijer and Spiers, 2005), and equations for pressure solution creep and frictional sliding (Section 2.5.2 and Eqs. 2.8 and 2.11) suggest that this mechanism accommodates displacement at strain rate sensitive to the driving stress, grain size and temperature.

Q5: What is the role of fluids?

In Chapter 4, dehydration reactions in oceanic crust were inferred to influence the location (in P-T space) of embrittlement and quartz vein formation. For a specific dehydration reaction, the volume of fluid released per unit volume of crust will vary depending upon the mineral assemblage. If the subducting crust is relatively dry, the volume of fluid release will be low, and the rate of release per change in P or T will be slow. Conversely, if the crust is fully equilibrated under hydrous conditions, then the volume of fluid release will be greater, and fluid will be released at a greater rate. For a given permeability and local pressure gradient, the degree of fluid pressurisation depends on the rate of fluid release. Therefore, greater rates of fluid production are potentially more effective at generating fluid pressurisation.

Section 4.11 suggested, based on thermodynamic constraints (Fig. 4.7), stable isotope data (Fig. 4.8) and noble gas isotope ratios published by Nishiyama *et al.* (2020), that the veins in coastal Makimine mélange formed from a silica-bearing aqueous fluid largely sourced from dehydration reactions occurring at deeper levels, with a volumetrically minor contribution resulting from dehydration of oceanic-crust. If local dehydration reactions contribute only a minor volume of fluid to the total fluid within the shear zone, then it seems likely that the ambient fluid pressure away from the location of dehydration reactions (e.g. at inland Makimine mélange conditions) is not substantially lower than where dehydration reactions are ongoing. In this model (summarised in Fig. 7.1), the ambient fluid pressure within the subduction thrust may be close to the critical pressure for brittle failure, and small reductions to effective stress arising due to local dehydration reactions, or small local shear stress amplifications, are sufficient to switch from ductile to brittle behaviour. In an environment where the ambient effective stress is low (e.g., Fig. 7.1), Figs. 2.3 and 4.10 show that local or temporal changes in differential stress might

be an equally effective mechanism for the generation of brittle veining. The potential for brittle fracturing in the absence of fluid pressure fluctuations is consistent with recent numerical models of mixed-material shear zones (Beall *et al.*, 2019a).

Fluids also have a critical role in facilitating solute transport during pressure-solution creep. Chapter 5 demonstrated the hydrated oceanic crust deforming by pressure solution creep and sliding along grain boundaries deformed at greatly reduced shear stresses compared to unaltered, relatively dry oceanic crust. In the case of oceanic crust, the presence of fluids during alteration on the sea floor, and during subduction, contributes to the formation of phyllosilicate-bearing mineral assemblages, allowing for low strengths during frictional-viscous creep. A key conclusion of Chapter 5 is that the hydration state prior to subduction will have a strong control on strength of oceanic crust. To summarise, while localised metamorphic dehydration produces patches of low effective stress, the presence of fluids also allows (a) alteration of oceanic crust to mechanically weak mineralogies, and (b) the operation of pressure solution creep. Localised metamorphic dehydration, and points (a) and (b), contribute to a stress state where ambient effective stresses are generally low. In this state, relatively small stress perturbations of less than a few tens of MPa are needed to transition from continuous, aseismic ductile creep to discontinuous, potentially seismic brittle failure.

Q6: How, and where, might frictional instabilities arise down-dip of the nominal base of the seismogenic zone?

The crustal strength profile in Fig. 2.7 suggests the behaviour of the crust should transition from fracturing and frictional sliding to viscous creep in a discrete, narrow, transition zone. However, as shown in Section 4.4, mixed brittle-ductile behaviour occurs down-dip of regions which deformed ductilely. In Section 4.10, localised dehydration reactions were inferred to drive increased pore fluid pressures, producing patches of locally reduced effective stresses (Eq. 2.2, Eq. 2.3), which shift stress conditions closer to the critical stresses for brittle failure (Figs. 2.3 and 4.10). Similarly, Gao and Wang (2017) suggest that separation between the base of the seismogenic zone and the ETS zone (Fig. 2.14) is a result of a permeability contrast near the intersection with the mantle wedge, producing locally reduced effective stresses, driving brittle

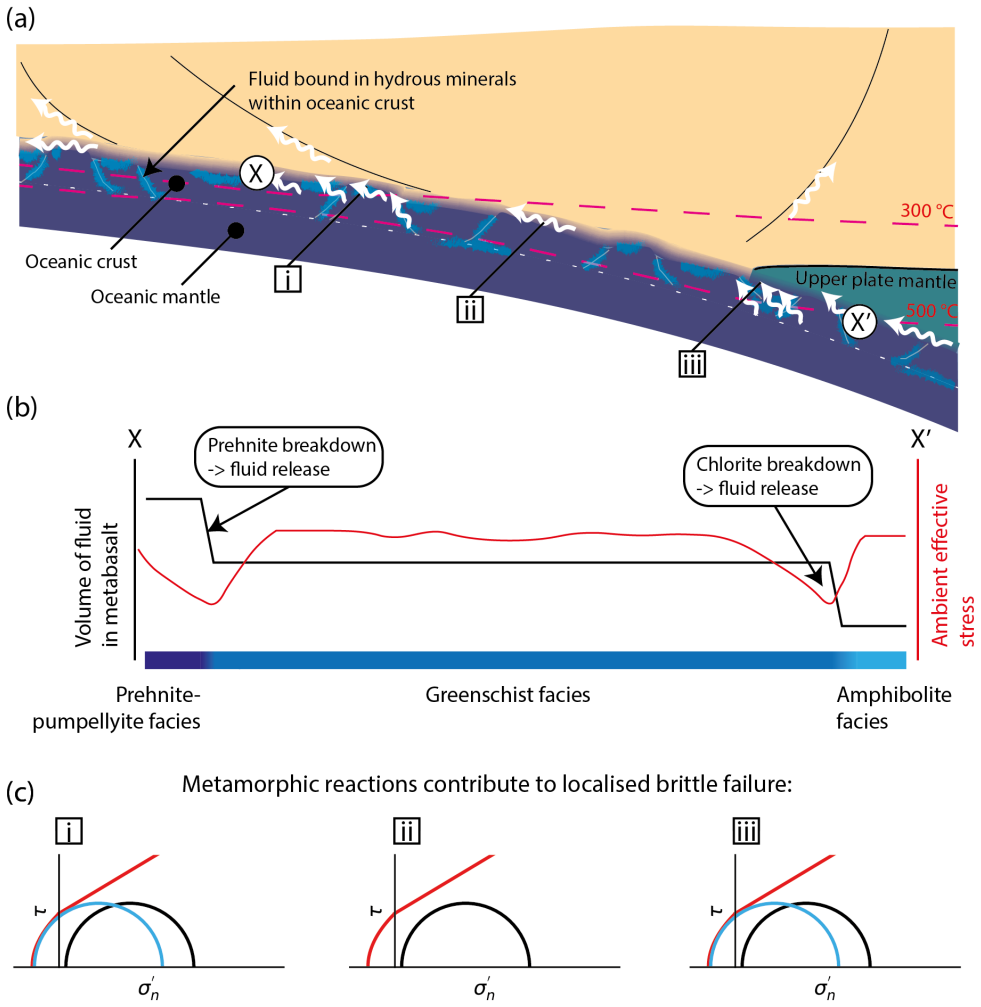

Figure 7.1: The effect of dehydration reactions on the distribution of deformation style. (a) Sketch of a subduction zone, showing a fractured and partially hydrated slab releasing fluid to the shear zone, as the slab passes through conditions of prehnite and chlorite breakdown. (b) Sketched graph showing the effect of localised dehydration reactions on the ambient effective stress within the shear zone. (c) Mohr diagrams showing interpretations of the stress conditions near (i and iii) and distal (ii) from dehydration reactions.

failure within an otherwise viscous regime.

Section 4.12 suggested that the location of specific dehydration reactions controls the distribution of patches of low effective stress, which contribute to embrittlement. In this model, the mineralogy and hydration state of the subducting oceanic plate influences the distribution of brittle behaviour. As outlined in response to Q5, subducting oceanic lithosphere with relatively dry or thin oceanic crust will release less fluid at a lower rate, than lithosphere with a thick, well hydrated crust. While metabasalt dehydration causes localised additions of fluid to the shear zone, pressurisation of the fluid is also dependent on permeability. Siliceous fluids flowing up-dip through a shear zone, guided by anisotropic permeability (e.g., Faulkner and Rutter, 2000; Huenges *et al.*, 1997; Kwon *et al.*, 2004), should precipitate silica as a result of decreasing equilibrium solubility (Fig. 4.11). Therefore, quartz precipitation causing decreased permeability and increased pressure, could drive brittle failure of a critically overpressured patch, independent of local dehydration reactions. However, as fluid pressure depends on both the fluid supply rate and the permeability, brittle failure seems more likely at conditions close to localised dehydration reactions.

In the NMR, brittlely-formed veins are more common near lithological contacts, which in section 4.10 was suggested to be the result of viscosity contrasts causing locally elevated shear stresses. In models of mixed-material viscous brittle-viscous shear zones presented in Beall *et al.* (2019a), where the pore fluid factor was set to $\lambda = 0.8$, large matrix-clast viscosity contrasts (10^3) were required to generate mixed fracturing and creep. In the NMR, the is no indication of such high viscosity contrasts. A potential explanation is that metamorphic dehydration at conditions close to the NMR resulted in pore fluid factors higher than the $\lambda = 0.8$ in the modes of Beall *et al.* (2019a), potentially reducing the difference between the ambient effective stress and brittle failure criteria.

As shown in Fig. 5.6b, laboratory-determined strengths for different oceanic plate lithologies converge within increasing temperature. This suggests that, for a mixed lithology shear zone, the effectiveness of stress amplification caused by viscosity contrasts should decrease with increasing depth along the plate interface (Fagereng and Beall, 2021; Strömgård, 1973). At condition below the fore-arc mantle, where strengths of sediments and hydrated oceanic crust con-

verge (Fig. 5.6b), the introduction of relatively viscous, passively hydrated antigorite serpentinite (Chapter 6, Section 6.10) might be a means of re-introducing viscosity heterogeneity to the plate interface. Similarly, at all depths, the inclusion of less altered basalt (e.g. as components of seamounts or horsts) to a shear zone containing well-hydrated basalt and subducted sediments, would provide additional viscosity heterogeneity. Variability in the lithologies deformed along the plate interface might be an explanation for brittle slip, such as tremor, occurring away from the P-T conditions of dehydration reactions.

Overall, frictional instabilities in the studied shear zones appear to require conditions of low effective stress, which is enabled by (a) continuous ductile deformation at low driving stresses by pressure solution creep and sliding along phyllosilicate cleavages, and (b) localised dehydration reactions causing locally elevated fluid pressure. However, outcrop observations (Section 4.4), and theoretical considerations (Section 2.3 and Fig. 4.10) show that provided effective stresses are sufficiently low, extension and extension-shear failure might also be caused by local and dynamic variations in shear stress within heterogeneous viscous shear zones frictional instabilities.

Chapter 8

Conclusion and future work

8.1 Conclusion

The overall aim of this work was to understand the geological processes that influence the style of subduction plate interface slip. To address this aim, observations from outcrops of exhumed shear zones were combined with microstructural study of shear zone rocks, thermodynamic modelling, and oxygen stable isotope measurements. The main conclusions are summarised below:

- Deformation along the Late Cretaceous Eurasian margin between the $\sim$ 300 °C and $\sim$ 500 °C isotherms occurred in a broad, km-scale shear zone containing hydrated oceanic crust, subducted sediment, and, at amphibolite facies conditions, serpentinised fore-arc mantle.

- In the Makimine melange and the NMR, foliations representing ductile deformation are ubiquitous, and ductile deformation is inferred to occur by a composite mechanism involveing sliding along phyllosilicate layers and pressure solution creep of non-phyllosilicates.

- Coastal exposures of the Makimine mélange, and the NMR, contain quartz veins which mutually overprint the ductile subduction-related foliation, indicating vein formation occurred in the final stages of subduction-related deformation. The P-T conditions inferred during the final stages of subduction-related strain correspond to conditions where localised dehydration reactions occur in oceanic crust.

- Localised dehydration of oceanic crust is inferred to cause to patches

of locally reduced effective stresses, contributing to embrittlement at prehnite-pumpellyite - greenschist facies transition, and at the greenschist facies - amphibolite facies transition. There is less evidence for embrittlement in shear zone exposures exhumed from peak P-T conditions away from these transition zones.

- Where effective stresses are sufficiently reduced by fluid pressurisation, shear stress concentrations relating to viscosity contrasts in the shear zones drive the local (meter to tens of meter) scale distribution of brittle fracturing.

- Hydrous conditions within oceanic crust allow for mechanically weak phyllosilicate-bearing mineral assemblages, and the operation of pressure-solution creep. Acting together, sliding along phyllosilicate foliations and pressure solution creep allow deformation of hydrated oceanic crust at driving stresses similar to those in subducted sediment.

- Following from the previous 3 points, the hydration state of the oceanic crust therefore has a strong influence on the distribution of fault slip styles, and in general, plate interface rheology, particularly along sediment-poor margins or where horst and graben structures expose the crust to the overriding plate.

- At mantle wedge conditions, including at natural strain rates, antigorite serpentinite is potentially more viscous than hydrated oceanic crust and subducted sediment, suggesting that plate interface strain might be preferentially concentrated in the subducting lithosphere.

- At mantle wedge conditions and natural strain rates that lead to formation of exhumed structures, the rheology of antigorite serpentinite is controlled by strain rate sensitive pressure solution creep, coupled to sliding along grain boundaries. Foliation development, assisted by non-coaxial strain, contributes to a reduction in antigorite serpentinite viscosity with increasing finite strain.

8.2 Directions for future work

The conclusions presented above raise several questions regarding subduction plate boundaries, and shear zones in general. Questions I feel have been raised by this work, and deserve attention in the future, are discussed briefly below:

- The hydration state of the incoming oceanic lithosphere is a major unknown, but is an important regulator of fluid production, and strength, where hydration allows the formation of phyllosilicate-bearing mineral assemblages. A goal for the future would be to establish better constraints on the hydration state of the oceanic crust, as Chapter 4 suggests that the crust is responsible for most fluid production in the transition between the seismogenic zone and the stably sliding, aseismic region below. A combination of measurement of geophysical properties indicating the presence of fluids or altered crust along active margins, and outcrop studies, perhaps of obducted oceanic crust, might shed light on the hydration state and mineralogy of oceanic crust pre-subduction.

- How are rocks subducted below deep (e.g. $>$ 20 km) levels of accretionary complexes, and below the fore-arc mantle, exhumed? This is a long-standing problem (e.g. Platt, 1993), but while recent numerical models (e.g. Agard *et al.*, 2009; Gerya *et al.*, 2002) and outcrop-based studies (e.g. Tewksbury-Christle *et al.*, 2021) have provided some suggestions, more work is needed to better understand this process, which might lead to greater confidence distinguishing subduction-related from exhumation-related deformation in exhumed shear zones. Numerical modelling coupled to studies of regional geology along active margins with well constrained kinematics and exhumed fault rocks might help to shed light on the exhumation process.

- The geotectonics of north-western Kyushu are still poorly understood; a preferred interpretation for the origin of the NMR is presented here although other interpretations exist (Nishiyama *et al.*, 2020). Regional geological studies dating metamorphic events and protolith formation across large areas of the NMR might help to resolve some ambiguity.

- It would be useful to extend the current range of thermodynamic models for minerals in oceanic crust and subducted sediment to lower metamor-

phic grades. Currently available models limit useful calculations to the upper prehnite-pumpellyite facies. If calculations could be reliably extended into the prehnite-pumpellyite and zeolite facies conditions, this would allow an assessment of fluid production well into the seismogenic zone, and potentially into the areas where shallow slow slip phenomena occur up-dip of the seismogenic zone. Calculations at lower metamorphic grades might also help with understanding initial hydration of the oceanic crust on the sea floor.

- Pressure solution kinetics in plagioclase, amphibole, and serpentinite are poorly constrained, yet these are dominant minerals in mafic rocks, and dissolution-precipitation creep is an important component of the deformation process. Indentation experiments (e.g. Gratier *et al.*, 2009) would be a means of investigating pressure solution kinetics in these minerals, which would provide valuable constraints on the strength of these rocks.

- Phyllosilicates show intense mechanical anisotropy, with weak strengths parallel to (001). Experiments by Kronenberg *et al.* (1990), Mares and Kronenberg (1993), Shea and Kronenberg (1992), and Mariani *et al.* (2006) produced results consistent with strain accommodated by dislocation motion, while other experiments (e.g. den Hartog *et al.*, 2013; Okamoto *et al.*, 2019; Van Diggelen *et al.*, 2010) suggest frictional slip. It is unclear which mechanism operates in natural fault rocks, so further experiments are needed to understand the conditions under which dislocation-mediated or frictional slip operate. Experiments at closer to natural strain rates might help understand the slip mechanism operating natural rocks, however long durations (e.g. weeks to months) would required to achieve strain rates substantially closer to natural ductile shear zones.

- Seamounts, which have a similar composition to oceanic crust, are commonly thought of as asperities on subducting oceanic lithosphere (e.g. Cloos, 1992). If weak phyllosilicates are stable in oceanic crust compositions at metamorphic grades within the seismogenic zone, and provided that pressure solution kinetics allow, seamounts may be less of an asperity than commonly assumed. Conversely, if pressure solution kinetics are slow, or phyllosilicates are not stable, the seamount might be relatively

rigid. Some geological investigation, perhaps in ophiolite, or drilling of seamounts along active margins might shed light on their mineralogy, and likely slip behaviour.

References

Abers, G. A. (2005). Seismic low-velocity layer at the top of subducting slabs: observations, predictions, and systematics. *Physics of the Earth and Planetary Interiors*, *149*(1-2), 7–29.

Abers, G. A., van Keken, P. E., Kneller, E. A., Ferris, A., and Stachnik, J. C. (2006). The thermal structure of subduction zones constrained by seismic imaging: Implications for slab dehydration and wedge flow. *Earth and Planetary Science Letters*, *241*(3-4), 387–397.

Abers, G. A., van Keken, P. E., and Wilson, C. R. (2020). Deep decoupling in subduction zones: Observations and temperature limits. *Geosphere*, *16*(6), 1408–1424.

Agard, P., Yamato, P., Jolivet, L., and Burov, E. (2009). Exhumation of oceanic blueschists and eclogites in subduction zones: Timing and mechanisms. *Earth-Science Reviews*, *92*(1-2), 53–79.

Aki, K. (1967). Scaling Law of Seismic Spectrum. *Journal of Geophysical Research*, *72*(4), 1217–1231.

Alt, J. C., Honnorez, J., Laverne, C., and Emmermann, R. (1986). Hydrothermal alteration of a 1 km section through the upper oceanic crust, Deep Sea Drilling Project Hole 504B: Mineralogy, chemistry and evolution of seawater-basalt interactions. *Journal of Geophysical Research*, *91*(B10), 309–335.

Amiguet, E., Van De Moortéle, B., Cordier, P., Hilairet, N., and Reynard, B. (2014). Deformation mechanisms and rheology of serpentines in experiments and in nature. *Journal of Geophysical Research: Solid Earth*, *119*, 4640–4655.

Amontons, G. (1699). De la resistance causeé dans les machines (About resistance and force in machines). *Mémoires de l'Académie royale des sciences (Paris)*, 257–282.

Anderson, E. M. (1951). *The Dynamics of Faulting and Dyke Formation with Application to Britain* (2 ed.). Edinburgh: Oliver and Boyd.

Ando, R., Takeda, N., and Yamashita, T. (2012). Propagation dynamics of seismic and aseismic slip governed by fault heterogeneity and Newtonian rheology. *Journal of Geophysical Research: Solid Earth*, *117*(B11), 1–14.

Audet, P., Bostock, M. G., Christensen, N. I., and Peacock, S. M. (2009). Seismic evidence for overpressured subducted oceanic crust and megathrust fault sealing. *Nature*, *457*, 76–78.

Audet, P. and Bürgmann, R. (2014). Possible control of subduction zone slow-earthquake periodicity by silica enrichment. *Nature*, *510*, 389–392.

Audet, P. and Kim, Y.-H. (2016). Teleseismic constraints on the geological environment of deep episodic slow earthquakes in subduction zone forearcs: A review. *Tectonophysics*, *670*, 1–15.

Audet, P. and Schaeffer, A. J. (2018). Fluid pressure and shear zone development over the locked to slow slip region in Cascadia. *Science Advances*, *4*(3), eaar2982.

Auzende, A.-L., Escartin, J., Walte, N. P., Guillot, S., Hirth, G., and Frost, D. J. (2015). Deformation mechanisms of antigorite serpentinite at subduction zone conditions determined from experimentally and naturally deformed rocks. *Earth and Planetary Science Letters*, *411*, 229–240.

Auzende, A.-L., Guillot, S., Devouard, B., and Baronnet, A. (2006). Serpentinites in an Alpine convergent setting: Effects of metamorphic grade and deformation on microstructures. *European Journal of Mineralogy*, *18*, 21–33.

Bachmann, F., Hielscher, R., and Schaeben, H. (2010). Texture Analysis with MTEX - Free and Open Source Software Toolbox. *Solid State Phenomena*, *160*, 63–68.

Bachmann, F., Hielscher, R., and Schaeben, H. (2011). Grain detection from 2d and 3d EBSD data-Specification of the MTEX algorithm. *Ultramicroscopy*, *111*(12), 1720–1733.

Barnes, P. M., Wallace, L. M., Saffer, D. M., Bell, R. E., Underwood, M. B., Fagereng, Å., Meneghini, F., Savage, H. M., Rabinowitz, H. S., Morgan, J. K., Kitajima, H., Kutterolf, S., Hashimoto, Y., Engelmann de Oliveira, C. H., Noda, A., Crundwell, M. P., Shepherd, C. L., Woodhouse, A. D., Harris, R. N., Wang, M., Henrys, S., Barker, D. H. N., Petronotis, K. E., Bourlange, S. M., Clennell, M. B., Cook, A. E., Dugan, B. E., Elger, J., Fulton, P. M., Gamboa, D., Greve, A., Han, S., Hüpers, A., Ikari, M. J., Ito, Y., Kim, G. Y., Koge, H., Lee, H., Li, X., Luo, M., Malie, P. R., Moore, G. F., Mountjoy, J. J., McNamara, D. D., Paganoni, M., Screaton, E. J., Shankar, U., Shreedharan, S., Solomon, E. A., Wang, X., Wu, H., Pecher, I. A., and LeVay, L. J. (2020). Slow slip source characterized by lithological and geometric heterogeneity. *Science Advances*, *6*(eaay3314), 1–10.

Bartlow, N. M., Wallace, L. M., Beavan, R. J., Bannister, S., and Segall, P. (2014). Time-dependent modeling of slow slip events and associated seismicity and tremor at the Hikurangi subduction zone, New Zealand. *Journal of Geophysical Research: Solid Earth*, *119*(1), 734–753.

Basu, S., Zhou, A., and Barsoum, M. W. (2009). On spherical nanoindentations, kinking nonlinear elasticity of mica single crystals and their geological implications. *Journal of Structural Geology*, *31*, 791–801.

Beall, A., Fagereng, Å., and Ellis, S. (2019a). Fracture and Weakening of Jammed Subduction Shear Zones, Leading to the Generation of Slow Slip Events. *Geochemistry, Geophysics, Geosystems*, *20*(11), 4869–4884.

Beall, A., Fagereng, Å., and Ellis, S. (2019b). Strength of Strained Two-Phase Mixtures: Application to Rapid Creep and Stress Amplification in Subduction Zone Mélange. *Geophysical Research Letters*, *46*, 169–178.

Bebout, G. E. (1991). Field-Based Evidence for Devolatilization in Subduction Zones: Implications for Arc Magmatism. *Science*, *251*(4992), 413–416.

Behr, M. M., Kotowski, A. J., and Ashley, K. T. (2018). Dehydration-induced

rheological heterogeneity and the deep tremor source in warm subduction zones. *Geology*, *46*(5), 475–478.

Behr, W. M. and Becker, T. W. (2018). Sediment control on subduction plate speeds. *Earth and Planetary Science Letters*, *502*, 166–173.

Behr, W. M. and Bürgmann, R. (2021). What's down there? The structures, materials and environment of deep-seated slow slip and tremor. *Philosophical Transactions of the Royal Society A: Mathematical, Physical and Engineering Sciences*, *379*(2193), 20200218.

Behr, W. M. and Platt, J. P. (2013). Rheological evolution of a Mediterranean subduction complex. *Journal of Structural Geology*, *54*, 136–155.

Behr, W. M. and Platt, J. P. (2014). Brittle faults are weak, yet the ductile middle crust is strong: Implications for lithospheric mechanics. *Geophysical Research Letters*, *41*(22), 8067–8075.

Bernaudin, M. and Gueydan, F. (2018). Episodic Tremor and Slip Explained by Fluid-Enhanced Microfracturing and Sealing. *Geophysical Research Letters*, *45*(8), 3471–3480.

Bilek, S. L. and Lay, T. (2002). Tsunami earthquakes possibly widespread manifestations of frictional conditional stability. *Geophysical Research Letters*, *29*(14), 1–4.

Bletery, Q. and Nocquet, J.-M. (2020). Slip bursts during coalescence of slow slip events in Cascadia. *Nature Communications*, *11*(1), 2159.

Bons, P. D., Elburg, M. A., and Gomez-Rivas, E. (2012). A review of the formation of tectonic veins and their microstructures. *Journal of Structural Geology*, *43*, 33–62.

Bos, B., Peach, C. J., and Spiers, C. J. (2000). Frictional-viscous flow of simulated fault gouge caused by the combined effects of phyllosilicates and pressure solution. *Tectonophysics*, *327*(3-4), 173–194.

Bos, B. and Spiers, C. J. (2002). Frictional-viscous flow of phyllosilicate-bearing fault rock: Microphysical model and implications for crustal strength profiles. *Journal of Geophysical Research*, *107*(B2), 1–13.

Boudier, F., Baronnet, A., and Mainprice, D. (2010). Serpentine Mineral Replacements of Natural Olivine and their Seismic Implications: Oceanic Lizardite versus Subduction-Related Antigorite. *Journal of Petrology*, *51*(1-2), 495–512.

Brace, W. F. and Kohlstedt, D. L. (1980). Limits on lithospheric stress imposed by laboratory experiments. *Journal of Geophysical Research: Solid Earth*, *85*(B11), 6248–6252.

Brown, J. R., Beroza, G. C., Ide, S., Ohta, K., Shelly, D. R., Schwartz, S. Y., Rabbel, W., Thorwart, M., and Kao, H. (2009). Deep low-frequency earthquakes in tremor localize to the plate interface in multiple subduction zones. *Geophysical Research Letters*, *36*, 1–5.

Bukovská, Z., Jeřábek, P., and Morales, L. F. G. (2016). Major softening at brittle-ductile transition due to interplay between chemical and deformation processes: An insight from evolution of shear bands in the South Armorican Shear Zone. *Journal of Geophysical Research: Solid Earth*, *121*(2), 1158–1182.

Bürgmann, R. (2018). The geophysics, geology and mechanics of slow fault slip. *Earth and Planetary Science Letters*, *495*, 112–134.

Bürgmann, R. and Dresen, G. (2008). Rheology of the Lower Crust and Upper Mantle: Evidence from Rock Mechanics, Geodesy, and Field Observations. *Annual Review of Earth and Planetary Sciences*, *36*(1), 531–567.

Burlini, L., Di Toro, G., and Meredith, P. (2009). Seismic tremor in subduction zones: Rock physics evidence. *Geophysical Research Letters*, *36*, 1–5.

Byerlee, J. (1978). Friction of rocks. *Pure and Applied Geophysics*, *116*(4-5), 615–626.

Byerlee, J. D. (1968). Brittle-ductile transition in rocks. *Journal of Geophysical Research*, *73*(14), 4741–4750.

Chernak, L. J. and Hirth, G. (2010). Deformation of antigorite serpentinite at high temperature and pressure. *Earth and Planetary Science Letters*, *296*, 23–33.

Chestler, S. R. and Creager, K. C. (2017). A Model for Low-Frequency Earthquake Slip. *Geochemistry, Geophysics, Geosystems*, *18*(12), 4690–4708.

Clift, P. and Vannucchi, P. (2004). Controls on tectonic accretion versus erosion in subduction zones: Implications for the origin and recycling of the continental crust. *Reviews of Geophysics*, *42*(2), RG2001.

Cloos, M. (1992). Thrust-type subduction-zone earthquakes and seamount asperities: A physical model for seismic rupture. *Geology*, *20*(7), 601.

Collettini, C., Niemeijer, A., Viti, C., and Marone, C. (2009). Fault zone fabric and fault weakness. *Nature*, *462*, 907–910.

Collettini, C., Tesei, T., Scuderi, M. M., Carpenter, B. M., and Viti, C. (2019). Beyond Byerlee friction, weak faults and implications for slip behavior. *Earth and Planetary Science Letters*, *519*, 245–263.

Condit, C. B., Guevara, V. E., Delph, J. R., and French, M. E. (2020). Slab dehydration in warm subduction zones at depths of episodic slip and tremor. *Earth and Planetary Science Letters*, *552*, 1–11.

Condit, C. B. and Mahan, K. H. (2018). Fracturing, fluid flow and shear zone development: Relationships between chemical and mechanical processes in Proterozoic mafic dykes from southwestern Montana, USA. *Journal of Metamorphic Geology*, *36*(2), 195–223.

Coulomb, C. A. (1821). *Theorie des machines simple (Theory of simple machines)*. Paris: Bachelier.

Cox, S. F. (2010). The application of failure mode diagrams for exploring the roles of fluid pressure and stress states in controlling styles of fracture-controlled permeability enhancement in faults and shear zones. *Geofluids*, *10*(1-2), 217–233.

Cross, A. J., Prior, D. J., Stipp, M., and Kidder, S. (2017). The recrystallized grain size piezometer for quartz: An EBSD-based calibration. *Geophysical Research Letters*, *44*(13), 6667–6674.

Currie, C. A., Cassidy, J. F., Hyndman, R. D., and Bostock, M. G. (2004). Shear wave anisotropy beneath the Cascadia subduction zone and western North American craton. *Geophysical Journal International*, *157*, 341–353.

David, E. C., Brantut, N., Hansen, L. N., and Mitchell, T. M. (2018). Absence of Stress-Induced Anisotropy During Brittle Deformation in Antigorite Serpentinite. *Journal of Geophysical Research: Solid Earth*, *123*, 10616–10644.

De Bresser, J., Ter Heege, J., and Spiers, C. J. (2001). Grain size reduction by dynamic recrystallization: can it result in major rheological weakening? *International Journal of Earth Sciences*, *90*(1), 28–45.

De Bresser, J. H. P. and Spiers, C. (1997). Strength characteristics of the r, f, and c slip systems in calcite. *Tectonophysics*, *272*(1), 1–23.

Dempsey, E. D., Prior, D. J., Mariani, E., Toy, V. G., and Tatham, D. J. (2011). Mica-controlled anisotropy within mid-to-upper crustal mylonites: An EBSD study of mica fabrics in the Alpine fault zone, New Zealand. *Geological Society Special Publication*, *360*(1), 33–47.

den Hartog, S. A. M., Niemeijer, A. R., and Spiers, C. J. (2013). Friction on subduction megathrust faults: Beyond the illite-muscovite transition. *Earth and Planetary Science Letters*, *373*, 8–19.

den Hartog, S. A. M. and Spiers, C. J. (2014). A microphysical model for fault gouge friction applied to subduction megathrusts. *Journal of Geophysical Research: Solid Earth*, *119*, 1510–1529.

Dieterich, J. H. (1979). Modeling of rock friction: 1. Experimental results and constitutive equations. *Journal of Geophysical Research*, *84*(B5), 2161.

Douglas, A., Beavan, J., Wallace, L. M., and Townend, J. (2005). Slow slip on the northern Hikurangi subduction interface, New Zealand. *Geophysical Research Letters*, *32*(16), L16305.

Dragert, H., Wang, K., and James, T. S. (2001). A Silent Slip Event on the Deeper Cascadia Subduction Interface. *Science*, *292*(5521), 1525–1528.

Durney, D. W. (1976). A Discussion on natural strain and geological structure - Pressure-solution and crystallization deformation. *Philosophical Transactions of the Royal Society of London. Series A, Mathematical and Physical Sciences*, *283*(1312), 229–240.

Ellis, S., Fagereng, Å., Barker, D., Henrys, S., Saffer, D., Wallace, L., Williams, C., and Harris, R. (2015). Fluid budgets along the northern Hikurangi subduction margin, New Zealand: the effect of a subducting seamount on fluid pressure. *Geophysical Journal International*, *202*(1), 277–297.

Escartín, J., Hirth, G., and Evans, B. (1997). Nondilatant brittle deformation of serpentinites: Implications for Mohr-Coulomb theory and the strength of faults. *Journal of Geophysical Research: Solid Earth*, *102*(B2), 2897–2913.

Escher, A. and Watterson, J. (1974). Stretching fabrics, folds and crustal shortening. *Tectonophysics*, *22*, 223–231.

Etheridge, M. A. (1983). Differential stress magnitudes during regional deformation and metamorphism: Upper bound imposed by tensile fracturing. *Geology*, *11*(4), 231.

Fagereng, Å. (2013). On stress and strain in a continuous-discontinuous shear zone undergoing simple shear and volume loss. *Journal of Structural Geology*, *50*, 44–53.

Fagereng, Å. and Beall, A. (2021). Is complex fault zone behaviour a reflection of rheological heterogeneity? *Philosophical Transactions of the Royal Society A: Mathematical, Physical and Engineering Sciences*, *379*, 1–23.

Fagereng, Å. and Biggs, J. (2019). New perspectives on 'geological strain rates' calculated from both naturally deformed and actively deforming rocks. *Journal of Structural Geology*, *125*, 100–110.

Fagereng, Å. and den Hartog, S. A. M. (2017). Subduction megathrust creep governed by pressure solution and frictional-viscous flow. *Nature Geoscience*, *10*, 51–57.

Fagereng, Å. and Diener, J. F. A. (2011). Non-volcanic tremor and discontinuous slab dehydration. *Geophysical Research Letters*, *38*, 1–5.

Fagereng, Å., Diener, J. F. A., Ellis, S., and Remitti, F. (2018). Fluid-related deformation processes at the up- and downdip limits of the subduction thrust seismogenic zone: What do the rocks tell us? In *Geology and Tectonics of Subduction Zones: A Tribute to Gaku Kimura*, Volume 534, 187–215. Geological Society of America.

Fagereng, Å., Diener, J. F. A., Meneghini, F., Harris, C., and Kvadsheim, A. (2018). Quartz vein formation by local dehydration embrittlement along the deep, tremorgenic subduction thrust interface. *Geology*, *46*(1), 67–70.

Fagereng, Å. and Ellis, S. (2009). On factors controlling the depth of interseismic coupling on the Hikurangi subduction interface, New Zealand. *Earth and Planetary Science Letters*, *278*(1-2), 120–130.

Fagereng, Å., Hillary, G. W. B., and Diener, J. F. A. (2014). Brittle-viscous deformation, slow slip, and tremor. *Geophysical Research Letters*, *41*(12), 4159–4167.

Fagereng, Å. and Sibson, R. H. (2010). Mélange rheology and seismic style. *Geology*, *38*(8), 751–754.

Faulkner, D. R. and Rutter, E. H. (2000). Comparisons of water and argon permeability in natural clay-bearing fault gouge under high pressure at 20 °C. *Journal of Geophysical Research: Solid Earth*, *105*(B7), 16415–16426.

Faure, M., Fabbri, O., and Monie, P. (1988). The Miocene bending of Southwest Japan: new $^{39}Ar/^{40}Ar$ and microtectonic constraints from the Nagasaki schists (western Kyushu), an extension of the Sanbagawa high-pressure belt. *Earth and Planetary Science Letters*, *91*(1-2), 105–116.

Fisher, D. M. and Brantley, S. L. (2014). The role of silica redistribution in the evolution of slip instabilities along subduction interfaces: Constraints from the Kodiak accretionary complex, Alaska. *Journal of Structural Geology*, *69*, 395–414.

Fisher, D. M., Brantley, S. L., Everett, M., and Dzvonik, J. (1995). Cyclic fluid flow through a regionally extensive fracture network within the Kodiak accretionary prism. *Journal of Geophysical Research: Solid Earth*, *100*(B7), 12881–12894.

Frank, F. C. and Read, W. T. (1950). Multiplication Processes for Slow Moving Dislocations. *Physical Review*, *79*(4), 722–723.

Frank, W. B., Shapiro, N. M., Husker, A. L., Kostoglodov, V., Romanenko, A., and Campillo, M. (2014). Using systematically characterized low-frequency

earthquakes as a fault probe in Guerrero, Mexico. *Journal of Geophysical Research: Solid Earth*, *119*, 7686–7700.

French, M. E., Hirth, G., and Okazaki, K. (2019). Fracture-induced pore fluid pressure weakening and dehydration of serpentinite. *Tectonophysics*, *767*, 228168.

French, M. E. and Zhu, W. (2017). Slow fault propagation in serpentinite under conditions of high pore fluid pressure. *Earth and Planetary Science Letters*, *473*, 131–140.

Fu, Y. and Freymueller, J. T. (2013). Repeated large Slow Slip Events at the southcentral Alaska subduction zone. *Earth and Planetary Science Letters*, *375*, 303–311.

Fukuda, J.-i. and Shimizu, I. (2017). Theoretical derivation of flow laws for quartz dislocation creep: Comparisons with experimental creep data and extrapolation to natural conditions using water fugacity corrections. *Journal of Geophysical Research: Solid Earth*, *122*(8), 5956–5971.

Gao, X. and Wang, K. (2017). Rheological separation of the megathrust seismogenic zone and episodic tremor and slip. *Nature*, *543*, 416–419.

Gardner, R., Piazolo, S., Evans, L., and Daczko, N. (2017). Patterns of strain localization in heterogeneous, polycrystalline rocks - a numerical perspective. *Earth and Planetary Science Letters*, *463*, 253–265.

Gardner, R. L., Piazolo, S., and Daczko, N. R. (2016). Shape of pinch and swell structures as a viscosity indicator: Application to lower crustal polyphase rocks. *Journal of Structural Geology*, *88*, 32–45.

Gasc, J., Hilairet, N., Yu, T., Ferrand, T., Schubnel, A., and Wang, Y. (2017). Faulting of natural serpentinite: Implications for intermediate-depth seismicity. *Earth and Planetary Science Letters*, *474*, 138–147.

Gerya, T. V., Stöckhert, B., and Perchuk, A. L. (2002). Exhumation of high-pressure metamorphic rocks in a subduction channel: A numerical simulation. *Tectonics*, *21*(6), 1–15.

Gholami, R. and Rasouli, V. (2014). Mechanical and Elastic Properties of Transversely Isotropic Slate. *Rock Mechanics and Rock Engineering*, *47*(5), 1763–1773.

Goddard, R. M., Hansen, L. N., Wallis, D., Stipp, M., Holyoke, C. W., Kumamoto, K. M., and Kohlstedt, D. L. (2020). A Subgrain-Size Piezometer Calibrated for EBSD. *Geophysical Research Letters*, *47*(23).

Gomberg, J., Agnew, D. C., and Schwartz, S. Y. (2016). Alternative source models of very low frequency events. *Journal of Geophysical Research: Solid Earth*, *121*(9), 6722–6740.

Gomberg, J., Wech, A., Creager, K., Obara, K., and Agnew, D. (2016). Reconsidering earthquake scaling. *Geophysical Research Letters*, *43*(12), 6243–6251.

Gosselin, J. M., Audet, P., Estéve, C., McLellan, M., Mosher, S. G., and Schaeffer, A. J. (2020). Seismic evidence for megathrust fault-valve behavior during episodic tremor and slip. *Science Advances*, *6*, 1–6.

Gratier, J. P. (1987). Pressure solution-deposition creep and associated tectonic differentiation in sedimentary rocks. *Geological Society, London, Special Publications*, *29*(1), 25–38.

Gratier, J.-P., Dysthe, D. K., and Renard, F. (2013). *The Role of Pressure Solution Creep in the Ductility of the Earth's Upper Crust*, Volume 54. Elsevier Inc.

Gratier, J.-P., Guiguet, R., Renard, F., Jenatton, L., and Bernard, D. (2009). A pressure solution creep law for quartz from indentation experiments. *Journal of Geophysical Research*, *114*(B3), B03403.

Gratier, J.-P., Noiriel, C., and Renard, F. (2015). Experimental evidence for rock layering development by pressure solution. *Geology*, *43*(10), 871–874.

Gratier, J.-P., Renard, F., and Labaume, P. (1999). How pressure solution creep and fracturing processes interact in the upper crust to make it behave in both a brittle and viscous manner. *Journal of Structural Geology*, *21*, 1189–1197.

Green, E. C. R., White, R. W., Diener, J. F. A., Powell, R., Holland, T. J. B., and Palin, R. M. (2016). Activity-composition relations for the calculation of partial melting equilibria in metabasic rocks. *Journal of Metamorphic Geology*, *34*(9), 845–869.

Greene, G. W., Kristiansen, K., Meyer, E. E., Boles, J. R., and Israelachvili, J. N. (2009). Role of electrochemical reactions in pressure solution. *Geochimica et Cosmochimica Acta*, *73*(10), 2862–2874.

Griffith, A. A. (1924). Theory of rupture. In C. B. Biezeno and J. M. Burgers (Eds.), *Proceedings of the First International Congress on Applied Mechanics*, Delft, 55–63. J Waltman.

Gundersen, E., Renard, F., Dysthe, D. K., Bjørlykke, K., and Jamtveit, B. (2002). Coupling between pressure solution creep and diffusive mass transport in porous rocks. *Journal of Geophysical Research: Solid Earth*, *107*(B11).

Gutenberg, B. and Richter, C. F. (1944). Frequency of Earthquakes in California. *Bulletin of the Seismological Society of America*, *34*(4), 185–188.

Hacker, B. R. (2008). H_2O subduction beyond arcs. *Geochemistry, Geophysics, Geosystems*, *9*(3), 1–24.

Hacker, B. R. and Christie, J. M. (1990). Brittle/ductile and plastic/cataclastic transitions in experimentally deformed and metamorphosed amphibolite. In A. G. Duba, W. B. Durham, J. W. Handin, and H. F. Wang (Eds.), *The brittle-ductile transition in rocks*, Volume 56, 127–147. American Geophysical Union.

Haines, S. H., Kaproth, B., Marone, C., Saffer, D., and van der Pluijm, B. (2013). Shear zones in clay-rich fault gouge: A laboratory study of fabric development and evolution. *Journal of Structural Geology*, *51*, 206–225.

Handy, M. R. (1990). The solid-state flow of polymineralic rocks. *Journal of Geophysical Research*, *95*(B6), 8647.

Hanks, T. C. and Kanamori, H. (1979). A moment magnitude scale. *Journal of Geophysical Research*, *84*(B5), 2348.

Hansen, L. N., David, E. C., Brantut, N., and Wallis, D. (2020). Insight into the microphysics of antigorite deformation from spherical nanoindentation. *Philosophical Transactions of the Royal Society A: Mathematical, Physical and Engineering Sciences*, *378*, 1–21.

Hansen, R. T. J., Bostock, M. G., and Christensen, N. I. (2012). Nature of the low velocity zone in Cascadia from receiver function waveform inversion. *Earth and Planetary Science Letters*, *337-338*, 25–38.

Hara, H. and Kimura, K. (2008). Metamorphic and cooling history of the Shimanto accretionary complex, Kyushu, Southwest Japan: Implications for the timing of out-of-sequence thrusting. *Island Arc*, *17*(4), 546–559.

Hardebeck, J. L. and Loveless, J. P. (2018). Creeping subduction zones are weaker than locked subduction zones. *Nature Geoscience*, *11*(1), 60–64.

Harris, C. and Vogeli, J. (2010). Oxygen isotope composition of garnet in the peninsula granite Cape granite suite South Africa: constraints on melting and emplacement mechanisms. *South African Journal of Geology*, *113*(4), 401–412.

Hattori, H. and Shibata, K. (1982). Radiometric dating of pre-Neogene granitic and metamorphic rocks in northwest Kyushu, Japan-with emphasis on geotectonics of the Nishisonogi zone. *Bull Geol Surv Jpn*, *33*, 57–84.

Hayman, N. W. and Lavier, L. L. (2014). The geologic record of deep episodic tremor and slip. *Geology*, *42*(3), 195–198.

He, C., Wang, Z., and Yao, W. (2007). Frictional sliding of gabbro gouge under hydrothermal conditions. *Tectonophysics*, *445*(3-4), 353–362.

Hermann, J., Müntener, O., and Scambelluri, M. (2000). The importance of serpentinite mylonites for subduction and exhumation of oceanic crust. *Tectonophysics*, *327*, 225–238.

Hilairet, N. and Reynard, B. (2009). Stability and dynamics of serpentinite layer in subduction zone. *Tectonophysics*, *465*, 24–29.

Hilairet, N., Reynard, B., Wang, Y., Daniel, I., Merkel, S., Nishiyama, N., and Petitgirard, S. (2007). High-Pressure Creep of Serpentine, Interseismic Deformation, and Initiation of Subduction. *Science*, *318*(5858), 1910–1913.

Hirauchi, K, i., Michibayashi, K., Ueda, H., and Katayama, I. (2010). Spatial variations in antigorite fabric across a serpentinite subduction channel: Insights from the Ohmachi Seamount, Izu-Bonin frontal arc. *Earth and Planetary Science Letters*, *299*, 196–206.

Hirauchi, K.-i., Katayama, I., and Kouketsu, Y. (2020). Semi-brittle deformation of antigorite serpentinite under forearc mantle wedge conditions. *Journal of Structural Geology*, *140*, 1–10.

Hirose, H., Hirahara, K., Kimata, F., Fujii, N., and Miyazaki, S. (1999). A slow thrust slip event following the two 1996 Hyuganada Earthquakes beneath the Bungo Channel, southwest Japan. *Geophysical Research Letters*, *26*(21), 3237–3240.

Hirth, G., Teyssier, C., and Dunlap, J. W. (2001). An evaluation of quartzite flow laws based on comparisons between experimentally and naturally deformed rocks. *International Journal of Earth Sciences*, *90*(1), 77–87.

Holland, T. J. B. and Powell, R. (1991). A Compensated-Redlich-Kwong (CORK) equation for volumes and fugacities of CO2 and H2O in the range 1 bar to 50 kbar and 100-1600 °C. *Contributions to Mineralogy and Petrology*, *109*(2), 265–273.

Holland, T. J. B. and Powell, R. (2011). An improved and extended internally consistent thermodynamic dataset for phases of petrological interest, involving a new equation of state for solids. *Journal of Metamorphic Geology*, *29*(3), 333–383.

Holyoke, C. W. and Tullis, J. (2006). Mechanisms of weak phase interconnection and the effects of phase strength contrast on fabric development. *Journal of Structural Geology*, *28*(4), 621–640.

Houston, H. (2015). Low friction and fault weakening revealed by rising sensitivity of tremor to tidal stress. *Nature Geoscience*, *8*(5), 409–415.

Huenges, E., Erzinger, J., Kück, J., Engeser, B., and Kessels, W. (1997). The permeable crust: Geohydraulic properties down to 9101 m depth. *Journal of Geophysical Research: Solid Earth*, *102*(B8), 18255–18265.

Huntington, K. W. and Klepeis, K. A. (2018). Challenges and opportunities for research in tectonics: Understanding deformation and the processes that link Earth systems, from geologic time to human time. Technical report.

Hyndman, R. D., McCrory, P. A., Wech, A., Kao, H., and Ague, J. (2015). Cascadia subducting plate fluids channelled to fore-arc mantle corner: ETS and silica deposition. *Journal of Geophysical Research: Solid Earth*, *120*(6), 4344–4358.

Hyndman, R. D. and Peacock, S. M. (2003). Serpentinization of the forearc mantle. *Earth and Planetary Science Letters*, *212*, 417–432.

Hyndman, R. D., Yamano, M., and Oleskevich, D. A. (1997). The seismogenic zone of subduction thrust faults. *The Island Arc*, *6*(3), 244–260.

Ide, S., Baltay, A., and Beroza, G. C. (2011). Shallow Dynamic Overshoot and Energetic Deep Rupture in the 2011 Mw 9.0 Tohoku-Oki Earthquake. *Science*, *332*(6036), 1426–1429.

Ide, S., Beroza, G. C., Shelly, D. R., and Uchide, T. (2007). A scaling law for slow earthquakes. *Nature*, *447*(7140), 76–79.

Ide, S., Shelly, D. R., and Beroza, G. C. (2007). Mechanism of deep low frequency earthquakes: Further evidence that deep non-volcanic tremor is generated by shear slip on the plate interface. *Geophysical Research Letters*, *34*(3), L03308.

Ide, S. and Tanaka, Y. (2014). Controls on plate motion by oscillating tidal stress: Evidence from deep tremors in western Japan. *Geophysical Research Letters*, *41*(11), 3842–3850.

Idrissi, H., Samaee, V., Lumbeeck, G., Werf, T., Pardoen, T., Schryvers, D., and Cordier, P. (2020). In Situ Quantitative Tensile Testing of Antigorite in a Transmission Electron Microscope. *Journal of Geophysical Research: Solid Earth*, *125*, 1–12.

Igarashi, T., Matsuzawa, T., and Hasegawa, A. (2003). Repeating earthquakes and interplate aseismic slip in the northeastern Japan subduction zone. *Journal of Geophysical Research: Solid Earth*, *108*(B5), 1–9.

Ikari, M. J. (2019). Laboratory slow slip events in natural geological materials. *Geophysical Journal International*, *218*(1), 354–387.

Ikari, M. J., Ito, Y., Ujiie, K., and Kopf, A. J. (2015). Spectrum of slip behaviour in Tohoku fault zone samples at plate tectonic slip rates. *Nature Geoscience*, *8*(11), 870–874.

Ikari, M. J., Niemeijer, A. R., and Marone, C. (2011). The role of fault zone fabric and lithification state on frictional strength, constitutive behavior, and deformation microstructure. *Journal of Geophysical Research*, *116*(B8), B08404.

Ikesawa, E., Sakaguchi, A., and Kimura, G. (2003). Pseudotachylyte from an ancient accretionary complex: Evidence for melt generation during seismic slip along a master décollement? *Geology*, *31*(7), 637.

Im, K., Saffer, D., Marone, C., and Avouac, J.-P. (2020). Slip-rate-dependent friction as a universal mechanism for slow slip events. *Nature Geoscience*, *13*(10), 705–710.

Imber, J., Holdsworth, R. E., Butler, C. A., and Strachan, R. A. (2001). A reappraisal of the Sibson-Scholz fault zone model: The nature of the frictional to viscous ("brittle-ductile") transition along a long-lived, crustal-scale fault, Outer Hebrides, Scotland. *Tectonics*, *20*(5), 601–624.

Ioannidi, P. I., Angiboust, S., Oncken, O., Agard, P., Glodny, J., and Sudo, M. (2020). Deformation along the roof of a fossil subduction interface in the transition zone below seismogenic coupling: The Austroalpine case and new insights from the Malenco Massif (Central Alps). *Geosphere*, *16*(2), 510–532.

Isozaki, Y., Aoki, K., Nakama, T., and Yanai, S. (2010). New insight into a subduction-related orogen: A reappraisal of the geotectonic framework and evolution of the Japanese Islands. *Gondwana Research*, *18*(1), 82–105.

Ito, Y., Asano, Y., and Obara, K. (2009). Very-low-frequency earthquakes indicate a transpressional stress regime in the Nankai accretionary prism. *Geophysical Research Letters*, *36*(20), L20309.

Jager, J. C., Cook, N. G. W., and Zimmerman, R. (2007). *Fundamentals of Rock Mechanics* (4 ed.). Blackwell.

Jambon, A. and Zimmermann, J. L. (1990). Water in oceanic basalts: evidence for dehydration of recycled crust. *Earth and Planetary Science Letters*, *101*, 323–331.

Jiang, Y., Wdowinski, S., Dixon, T. H., Hackl, M., Protti, M., and Gonzalez, V. (2012). Slow slip events in Costa Rica detected by continuous GPS observations, 2002-2011. *Geochemistry, Geophysics, Geosystems*, *13*(1), 1–18.

Kamiya, S. and Kobayashi, Y. (2000). Seismological evidence for the existence of serpentinized wedge mantle. *Geophysical Research Letters*, *27*(6), 819–822.

Kanamori, H. and Anderson, D. L. (1975). Theoretical basis of some empirical relations in seismology. *Bulletin of the Geological Society of America*, *65*(5), 1073–1095.

Kao, H., Wang, K., Dragert, H., Kao, J. Y., and Rogers, G. (2010). Estimating seismic moment magnitude (Mw) of tremor bursts in northern Cascadia: Implications for the "seismic efficiency" of episodic tremor and slip. *Geophysical Research Letters*, *37*(19), 1–6.

Katayama, I., Hirauchi, K.-I., Michibayashi, K., and Ando, J.-i. (2009). Trench-parallel anisotropy produced by serpentine deformation in the hydrated mantle wedge. *Nature*, *461*, 1114–1118.

Katsumata, A. and Kamaya, N. (2003). Low-frequency continuous tremor around the Moho discontinuity away from volcanoes in the southwest Japan. *Geophysical Research Letters*, *30*(1), 20–1–20–4.

Kenis, I., Urai, J., Vanderzee, W., Hilgers, C., and Sintubin, M. (2005). Rheology of fine-grained siliciclastic rocks in the middle crust - evidence from structural and numerical analysis. *Earth and Planetary Science Letters*, *233*(3-4), 351–360.

Kerrick, D. M. and Connolly, J. A. D. (2001). Metamorphic devolatilization of subducted oceanic metabasalts: implications for seismicity, arc magmatism and volatile recycling. *Earth and Planetary Science Letters*, *189*, 19–29.

Kilian, R., Heilbronner, R., and Stünitz, H. (2011). Quartz grain size reduction in a granitoid rock and the transition from dislocation to diffusion creep. *Journal of Structural Geology*, *33*(8), 1265–1284.

Kimura, G. (1997). Cretaceous episodic growth of the Japanese Islands. *The Island Arc*, *6*(1), 52–68.

King, R. L., Kohn, M. J., and Eiler, J. M. (2003). Constraints on the petrologic structure of the subduction zone slab-mantle interface from Franciscan Complex exotic ultramafic blocks. *Geological Society of America Bulletin*, *115*(9), 1097–1109.

Kirkpatrick, J. D., Fagereng, Å., and Shelly, D. R. (2021). Geological constraints on the mechanisms of slow earthquakes. *Nature Reviews Earth & Environment*, *2*(4), 285–301.

Klein, E., Duputel, Z., Zigone, D., Vigny, C., Boy, J.-P., Doubre, C., and Meneses, G. (2018). Deep Transient Slow Slip Detected by Survey GPS in the Region of Atacama, Chile. *Geophysical Research Letters*, *45*(22), 12,263–12,273.

Knipe, R. J. (1989). Deformation mechanisms - recognition from natural tectonites. *Journal of Structural Geology*, *11*(1-2), 127–146.

Kotowski, A. J. and Behr, W. M. (2019). Length scales and types of heterogeneities along the deep subduction interface: Insights from exhumed rocks on Syros Island, Greece. *Geosphere*, *15*(4), 1038–1065.

Kouchi, Y., Orihashi, Y., Obara, H., Miyata, K., Shimojo, M., Otoh, S., Aoyama, M., Akahori, Y., and Yanai, S. (2011). Discovery of Shimanto High-P/T Metamorphic Rocks from the Western Margin of Kyushu, Japan. *Journal of Geography (Chigaku Zasshi)*, *120*(1), 30–39.

Kronenberg, A. K., Kirby, S. H., and Pinkston, J. (1990). Basal slip and mechanical anisotropy of biotite. *Journal of Geophysical Research*, *95*(B12), 19257–19278.

Kwon, O., Kronenberg, A. K., Gangi, A. F., Johnson, B., and Herbert, B. E. (2004). Permeability of illite-bearing shale: 1. Anisotropy and effects of clay content and loading. *Journal of Geophysical Research: Solid Earth*, *109*(B10), 1–19.

Larson, K. M., Lowry, A. R., Kostoglodov, V., Hutton, W., Sánchez, O., Hudnut, K., and Suárez, G. (2004). Crustal deformation measurements in Guerrero, Mexico. *Journal of Geophysical Research: Solid Earth*, *109*(B4), 1–19.

Leeman, J. R., Saffer, D. M., Scuderi, M. M., and Marone, C. (2016). Laboratory observations of slow earthquakes and the spectrum of tectonic fault slip modes. *Nature Communications*, *7*(1), 11104.

Li, J. C. M. (1962). Possibility of Subgrain Rotation during Recrystallization. *Journal of Applied Physics*, *33*(10), 2958–2965.

Li, S., Wang, K., Wang, Y., Jiang, Y., and Dosso, S. E. (2018). Geodetically Inferred Locking State of the Cascadia Megathrust Based on a Viscoelastic Earth Model. *Journal of Geophysical Research: Solid Earth*, *123*(9), 8056–8072.

Linde, A. T., Gladwin, M. T., Johnston, M. J. S., Gwyther, R. L., and Bilham, R. G. (1996). A slow earthquake sequence on the San Andreas fault. *Nature*, *383*(6595), 65–68.

Liu, W., Zhang, J., Cao, Y., and Jin, Z. (2020). Geneses of Two Contrasting Antigorite Crystal Preferred Orientations and Their Implications for Seismic Anisotropy in the Forearc Mantle. *Journal of Geophysical Research: Solid Earth*, *125*(9), 1–24.

Liu, Y. and Rice, J. R. (2005). Aseismic slip transients emerge spontaneously in three-dimensional rate and state modeling of subduction earthquake sequences. *Journal of Geophysical Research*, *110*(B8), B08307.

Liu, Y. and Rice, J. R. (2007). Spontaneous and triggered aseismic deformation transients in a subduction fault model. *Journal of Geophysical Research*, *112*(B9), B09404.

Lloyd, G. E., Ferguson, C. C., and Reading, K. (1982). A stress-transfer model for the development of extension fracture boudinage. *Journal of Structural Geology*, *4*(3), 355–372.

Lockner, D. A. (1995). Rock Failure. In Ahrens, T. J. (Ed.), *Rock Physics and Phase Relations, A Handbook of Physical Constants*, 127–147. Washington D.C: American Geophysical Union.

Lowry, A. R., Larson, K. M., Kostoglodov, V., and Bilham, R. G. (2001). Transient fault slip in Guerrero, southern Mexico. *Geophysical Research Letters*, *28*(19), 3753–3756.

Mackenzie, J. S., Needham, D. T., and Agar, S. M. (1987). Progressive deformation in an accretionary complex: An example from the Shimanto belt of eastern Kyushu, southwest Japan. *Geology*, *15*(4), 353.

Mackwell, S. J., Zimmerman, M. E., and Kohlstedt, D. L. (1998). High-temperature deformation of dry diabase with application to tectonics on Venus. *Journal of Geophysical Research: Solid Earth*, *103*(B1), 975–984.

Maltman, A. J. (1978). Serpentinite textures in Anglesey, North Wales, United Kingdom. *Geological Society of America Bulletin*, *89*(7), 972.

Manning, C. E. (1994). The solubility of quartz in H_2O in the lower crust and upper mantle. *Geochimica et Cosmochimica Acta*, *58*(22), 4831–4839.

Mares, V. M. and Kronenberg, A. K. (1993). Experimental deformation of muscovite. *Journal of Structural Geology*, *15*(9-10), 1061–1075.

Mariani, E., Brodie, K. H., and Rutter, E. H. (2006). Experimental deformation of muscovite shear zones at high temperatures under hydrothermal conditions and the strength of phyllosilicate-bearing faults in nature. *Journal of Structural Geology*, *28*(9), 1569–1587.

Marone, C. (1998). Laboratory-derived friction laws and their application to seismic faulting. *Annual Review of Earth and Planetary Sciences*, *26*(1), 643–696.

Masuda, K., Arai, T., and Takahashi, M. (2019). Effects of frictional properties of quartz and feldspar in the crust on the depth extent of the seismogenic zone. *Progress in Earth and Planetary Science*, *6*(50), 1–8.

Masuda, T. and Ando, S. (1988). Viscous flow around a rigid spherical body: a hydrodynamical approach. *Tectonophysics*, *148*(3-4), 337–346.

Matsubara, M., Obara, K., and Kasahara, K. (2009). High-VP/VS zone accompanying non-volcanic tremors and slow-slip events beneath southwestern Japan. *Tectonophysics*, *472*, 6–17.

Matsuhisa, Y., Goldsmith, J. R., and Clayton, R. N. (1979). Oxygen isotopic fractionation in the system quartz-albite-anorthite-water. *Geochimica et Cosmochimica Acta*, *43*(7), 1131–1140.

Mattey, D., Lowry, D., and Macpherson, C. (1994). Oxygen isotope composition of mantle peridotite. *Earth and Planetary Science Letters*, *128*(3-4), 231–241.

Mazzotti, S. and Adams, J. (2004). Variability of Near-Term Probability for the Next Great Earthquake on the Cascadia Subduction Zone. *Bulletin of the Seismological Society of America*, *94*(5), 1954–1959.

McCrory, P. A., Hyndman, R. D., and Blair, J. L. (2014). Relationship between the Cascadia fore-arc mantle wedge, nonvolcanic tremor, and the downdip limit of seismogenic rupture. *Geochemistry, Geophysics, Geosystems*, *15*, 1071–1095.

Meneghini, F. and Moore, J. C. (2007). Deformation and hydrofracture in a subduction thrust at seismogenic depths: The Rodeo Cove thrust zone, Marin Headlands, California. *Geological Society of America Bulletin*, *119*(1-2), 174–183.

Michel, S., Gualandi, A., and Avouac, J.-P. (2019). Similar scaling laws for earthquakes and Cascadia slow-slip events. *Nature*, *574*(7779), 522–526.

Miller, M. M. (2002). Periodic Slow Earthquakes from the Cascadia Subduction Zone. *Science*, *295*(5564), 2423–2423.

Miyazaki, K., Ozaki, M., Saito, M., and Toshimitsu, S. (2016). The Kyushu-Ryukyu Arc. In T. Moreno, S. Wallis, T. Kojima, and W. Gibbons (Eds.), *The Geology of Japan*, 139–174. Geological Society London.

Moore, J. C. and Vrolijk, P. (1992). Fluids in accretionary prisms. *Reviews of Geophysics*, *30*(2), 113.

Morales, L. F. G., Mainprice, D., and Kern, H. (2018). Olivine-antigorite orientation relationships: Microstructures, phase boundary misorientations and the effect of cracks in the seismic properties of serpentinites. *Tectonophysics*, *724-725*, 93–115.

Mori, Y., Shigeno, M., Miyazaki, K., and Nishiyama, T. (2019). Peak metamorphic temperature of the Nishisonogi unit of the Nagasaki Metamorphic Rocks, western Kyushu, Japan. *Journal of Mineralogical and Petrological Sciences*, *114*(4), 170–177.

Mori, Y., Shigeno, M., and Nishiyama, T. (2014). Fluid-metapelite interaction in an ultramafic mélange: implications for mass transfer along the slab-mantle interface in subduction zones. *Earth, Planets and Space*, *66*(47), 1–8.

Muehlenbachs, K. (1986). Chapter 12. Alteration of the oceanic crust and the 18O history of seawater. In J. W. Valley, H. P. Taylor, and J. R. O'Neil (Eds.), *Stable Isotopes in High Temperature Geological Processes*, 425–444. Berlin, Boston: De Gruyter.

Muller, R. D., Sdrolias, M., Gaina, C., Steinberger, B., and Heine, C. (2008). Long-Term Sea-Level Fluctuations Driven by Ocean Basin Dynamics. *Science*, *319*(5868), 1357–1362.

Muñoz-Montecinos, J., Angiboust, S., Cambeses, A., and García-Casco, A. (2020). Multiple veining in a paleo-accretionary wedge: The metamorphic rock record of prograde dehydration and transient high pore-fluid pressures along the subduction interface (Western Series, central Chile). *Geosphere*, *16*(3), 765–786.

Murata, A. (1997). Geological map of Miyazaki prefecture, 1: 200,000. *Miyazaki Prefectural Government*.

Murr, L. E. (1975). Some observations of grain boundary ledges and ledges as dislocation sources in metals and alloys. *Metallurgical Transactions A*, *6*(3), 505–513.

Nabarro, F. R. N. (1997). Fifty-year study of the Peierls-Nabarro stress. *Materials Science and Engineering: A*, *234-236*, 67–76.

Nagaya, T. and Wallis, S. R. (2018). Grain boundary sliding as an antigorite CPO formation mechanism and implications for the slab-mantle boundary rheology: Example of antigorite schist from the Sanbagawa belt, SW Japan. In *American Geophysical Union, Fall Meeting*, abstract #T31G–0393.

Nagaya, T., Wallis, S. R., Seto, Y., Miyake, A., Soda, Y., Uehara, S., and Matsumoto, M. (2017). Minimizing and quantifying mis-indexing in electron backscatter diffraction (EBSD) determinations of antigorite crystal directions. *Journal of Structural Geology*, *95*, 127–141.

Nakata, R., Suda, N., and Tsuruoka, H. (2008). Non-volcanic tremor resulting from the combined effect of Earth tides and slow slip events. *Nature Geoscience*, *1*(10), 676–678.

Nichols, A. R. L., Carroll, M. R., and Höskuldsson, Á. (2002). Is the Iceland hot spot also wet? Evidence from the water contents of undegassed submarine and subglacial pillow basalts. *Earth and Planetary Science Letters*, *202*, 77–87.

Niemeijer, A. R. (2018). Velocity-dependent slip weakening by the combined operation of pressure solution and foliation development. *Scientific Reports*, *8*, 1–10.

Niemeijer, A. R. and Spiers, C. J. (2005). Influence of phyllosilicates on fault strength in the brittle-ductile transition: insights from rock analogue experiments. *Geological Society, London, Special Publications*, *245*, 303–327.

Niemeijer, A. R., Spiers, C. J., and Bos, B. (2002). Compaction creep of quartz sand at 400-600 °C: experimental evidence for dissolution-controlled pressure solution. *Earth and Planetary Science Letters*, *195*(3-4), 261–275.

Nishiyama, T. (1989). Petrological study of the Nagasaki metamorphic rocks in the Nishisonogi Peninsula - with special reference to the greenstone complex and the reaction-enhanced ductility. *Memoirs of Geological Society of Japan*, *33*, 237–257.

Nishiyama, T., Mori, Y., and Shigeno, M. (2017). Jadeitites and associated metasomatic rocks from serpentinite mélanges in the Nishisonogi unit, Nagasaki Metamorphic Complex, western Kyushu, Japan: a review. *Journal of Mineralogical and Petrological Sciences*, *112*(5), 197–216.

Nishiyama, T., Ohfuji, H., Fukuba, K., Terauchi, M., Nishi, U., Harada, K., Unoki, K., Moribe, Y., Yoshiasa, A., Ishimaru, S., Mori, Y., Shigeno, M., and Arai, S. (2020). Microdiamond in a low-grade metapelite from a Cretaceous subduction complex, western Kyushu, Japan. *Scientific Reports*, *10*(1), 1–11.

Obara, K. (2002). Nonvolcanic Deep Tremor Associated with Subduction in Southwest Japan. *Science*, *296*(5573), 1679–1681.

Obara, K., Hirose, H., Yamamizu, F., and Kasahara, K. (2004). Episodic slow slip events accompanied by non-volcanic tremors in southwest Japan subduction zone. *Geophysical Research Letters*, *31*(23), 1–4.

Obara, K. and Ito, Y. (2005). Very low frequency earthquakes excited by the 2004 off the Kii peninsula earthquakes: A dynamic deformation process in the large accretionary prism. *Earth, Planets and Space*, *57*(4), 321–326.

Obara, K. and Kato, A. (2016). Connecting slow earthquakes to huge earthquakes. *Science*, *353*(6296), 253–257.

Obara, K., Tanaka, S., Maeda, T., and Matsuzawa, T. (2010). Depth-dependent activity of non-volcanic tremor in southwest Japan. *Geophysical Research Letters*, *37*(13), 1–5.

O'Hanley, D. S. (1991). Fault-Related Phenomena Associated with Hydration and Serpentine Recrystallization during Serpentinization. *Canadian Mineralogist*, *29*, 21–35.

Ohta, Y., Freymueller, J. T., Hreinsdotter, S., and Suito, H. (2006). A large slow slip event and the depth of the seismogenic zone in the south central Alaska subduction zone. *Earth and Planetary Science Letters*, *247*(1-2), 108–116.

Okamoto, A. S., Verberne, B. A., Niemeijer, A. R., Takahashi, M., Shimizu, I., Ueda, T., and Spiers, C. J. (2019). Frictional Properties of Simulated Chlorite Gouge at Hydrothermal Conditions: Implications for Subduction Megathrusts. *Journal of Geophysical Research: Solid Earth*, *124*(5), 4545–4565.

Okazaki, K. and Katayama, I. (2015). Slow stick slip of antigorite serpentinite under hydrothermal conditions as a possible mechanism for slow earthquakes. *Geophysical Research Letters*, *42*, 1099–1104.

Oliver, N. H. S. and Bons, P. D. (2001). Mechanisms of fluid flow and fluid-rock interaction in fossil metamorphic hydrothermal systems inferred from vein-wallrock patterns, geometry and microstructure. *Geofluids*, *1*, 137–162.

Orowan, E. (1940). Problems of plastic gliding. *Proceedings of the Physical Society*, *52*(1), 8–22.

Outerbridge, K. C., Dixon, T. H., Schwartz, S. Y., Walter, J. I., Protti, M., Gonzalez, V., Biggs, J., Thorwart, M., and Rabbel, W. (2010). A tremor and slip event on the Cocos-Caribbean subduction zone as measured by a global positioning system (GPS) and seismic network on the Nicoya Peninsula, Costa Rica. *Journal of Geophysical Research*, *115*(B10), B10408.

Pacheco, J. F., Sykes, L. R., and Scholz, C. H. (1993). Nature of seismic coupling along simple plate boundaries of the subduction type. *Journal of Geophysical Research: Solid Earth*, *98*(B8), 14133–14159.

Padrón-Navarta, J. A., Tommasi, A., Garrido, C. J., and L. S.-V., V. (2012). Plastic deformation and development of antigorite crystal preferred orientation in high-pressure serpentinites. *Earth and Planetary Science Letters*, *349-350*, 75–86.

Palazzin, G., Raimbourg, H., Famin, V., Jolivet, L., Kusaba, Y., and Yamaguchi, A. (2016). Deformation processes at the down-dip limit of the seismogenic zone: The example of Shimanto accretionary complex. *Tectonophysics*, *687*, 28–43.

Paterson, M. S. (1973). Nonhydrostatic thermodynamics and its geologic applications. *Reviews of Geophysics*, *11*(2), 355.

Paterson, M. S. and Wong, T. (2005). *Experimental rock deformation-the brittle field*. Springer Science & Business Media.

Peacock, S. M. (1990). Fluid Processes in Subduction Zones. *Science*, *248*(4953), 329–337.

Peacock, S. M. (1993). Large-scale hydration of the lithosphere above subducting slabs. *Chemical Geology*, *108*(1-4), 49–59.

Peacock, S. M. (2009). Thermal and metamorphic environment of subduction zone episodic tremor and slip. *Journal of Geophysical Research*, *114*(8), B00A07.

Peacock, S. M., Christensen, N. I., Bostock, M. G., and Audet, P. (2011). High pore pressures and porosity at 35 km depth in the Cascadia subduction zone. *Geology*, *39*(5), 471–474.

Peng, Z. and Gomberg, J. (2010). An integrated perspective of the continuum between earthquakes and slow-slip phenomena. *Nature Geoscience*, *3*(9), 599–607.

Petriglieri, J. R., Salvioli-Mariani, E., Mantovani, L., Tribaudino, M., Lottici, P. P., Laporte-Magoni, C., and Bersani, D. (2015). Micro-Raman mapping of the polymorphs of serpentine. *Journal of Raman Spectroscopy*, *46*(10), 953–958.

Phillips, N. J., Rowe, C. D., and Ujiie, K. (2019). For how long are pseudotachylytes strong? Rapid alteration of basalt-hosted pseudotachylytes from a shallow subduction complex. *Earth and Planetary Science Letters*, *518*, 108–115.

Plafker, G. (1965). Tectonic Deformation Associated with the 1964 Alaska Earthquake: The earthquake of 27 March 1964 resulted in observable crustal deformation of unprecedented areal extent. *Science*, *148*(3678), 1675–1687.

Plank, T. and Langmuir, C. H. (1998). The chemical composition of subducting sediment and its consequences for the crust and mantle. *Chemical Geology*, *145*(3-4), 325–394.

Platt, J. P. (1993). Exhumation of high-pressure rocks: a review of concepts and processes. *Terra Nova*, *5*(2), 119–133.

Platt, J. P., Xia, H., and Schmidt, W. L. (2018). Rheology and stress in subduction zones around the aseismic/seismic transition. *Progress in Earth and Planetary Science*, *5*(1), 24.

Poirier, J.-P. (1985). *Creep of Crystals*. Cambridge: Cambridge University Press.

Proctor, B. and Hirth, G. (2016). Ductile to brittle transition in thermally stable antigorite gouge at mantle pressures. *Journal of Geophysical Research: Solid Earth*, *121*, 1652–1663.

Raj, R. (1982). Creep in polycrystalline aggregates by matter transport through a liquid phase. *Journal of Geophysical Research: Solid Earth*, *87*(B6), 4731–4739.

Raj, R. and Ashby, M. F. (1971). On grain boundary sliding and diffusional creep. *Metallurgical Transactions*, *2*, 1113–1127.

Raleigh, C. B. and Paterson, M. S. (1965). Experimental deformation of serpentinite and its tectonic implications. *Journal of Geophysical Research*, *70*(16), 3965–3985.

Ramberg, H. (1955). Natural and Experimental Boudinage and Pinch-and-Swell Structures. *The Journal of Geology*, *63*(6), 512–526.

Ramsay, J. G. (1967). *Folding and Fracturing of Rocks*. McGraw-Hill.

Ramsay, J. G. (1980). Shear zone geometry: A review. *Journal of Structural Geology*, *2*(1-2), 83–99.

Ranero, C. R., Phipps Morgan, J., McIntosh, K., and Reichert, C. (2003). Bending-related faulting and mantle serpentinization at the Middle America trench. *Nature*, *425*(6956), 367–373.

Rebay, G., Powell, R., and Diener, J. F. A. (2010). Calculated phase equilibria for a MORB composition in a P-T range, 450-650 °C and 18-28 kbar: the stability of eclogite. *Journal of Metamorphic Geology*, *28*(6), 635–645.

Reber, J. E., Lavier, L. L., and Hayman, N. W. (2015). Experimental demonstration of a semi-brittle origin for crustal strain transients. *Nature Geoscience*, *8*(9), 712–715.

Reinen, L. A., Weeks, J. D., and Tullis, T. E. (1991). The frictional behavior of serpentinite: Implications for aseismic creep on shallow crustal faults. *Geophysical Research Letters*, *18*(10), 1921–1924.

Renard, F., Ortoleva, P., and Gratier, J.-P. (1997). Pressure solution in sandstones: influence of clays and dependence on temperature and stress. *Tectonophysics*, *280*(3-4), 257–266.

Robertson, E. C. (1955). Experimental study of the strength of rocks. *Bulletin of the Geological Society of America*, *66*, 1275–1314.

Rogers, G. and Dragert, H. (2003). Episodic Tremor and Slip on the Cascadia Subduction Zone: The Chatter of Silent Slip. *Science*, *300*(5627), 1942–1943.

Rooney, J. S., Tarling, M. S., Smith, S. A., and Gordon, K. C. (2018). Submicron Raman spectroscopy mapping of serpentinite fault rocks. *Journal of Raman Spectroscopy*, *49*, 279–286.

Rouméjon, S., Andreani, M., and Früh-Green, G. L. (2019). Antigorite crystallization during oceanic retrograde serpentinization of abyssal peridotites. *Contributions to Mineralogy and Petrology*, *174*(60), 1–25.

Rowe, C. D., Meneghini, F., and Moore, J. C. (2011). Textural record of the seismic cycle: strain-rate variation in an ancient subduction thrust. *Geological Society, London, Special Publications*, *359*(1), 77–95.

Rowe, C. D., Moore, J. C., Meneghini, F., and McKeirnan, A. W. (2005). Large-scale pseudotachylytes and fluidized cataclasites from an ancient subduction thrust fault. *Geology*, *33*(12), 937.

Rowe, C. D., Moore, J. C., and Remitti, F. (2013). The thickness of subduction plate boundary faults from the seafloor into the seismogenic zone. *Geology*, *41*(9), 991–994.

Royer, A. A. and Bostock, M. G. (2014). A comparative study of low frequency earthquake templates in northern Cascadia. *Earth and Planetary Science Letters*, *402*, 247–256.

Royer, A. A., Thomas, A. M., and Bostock, M. G. (2015). Tidal modulation and triggering of low-frequency earthquakes in northern Cascadia. *Journal of Geophysical Research: Solid Earth*, *120*, 384–405.

Rubinstein, J. L., La Rocca, M., Vidale, J. E., Creager, K. C., and Wech, A. G. (2008). Tidal Modulation of Nonvolcanic Tremor. *Science*, *319*(5860), 186–189.

Ruina, A. (1983). Slip instability and state variable friction laws. *Journal of Geophysical Research: Solid Earth*, *88*(B12), 10359–10370.

Ruiz, S., Metois, M., Fuenzalida, A., Ruiz, J., Leyton, F., Grandin, R., Vigny, C., Madariaga, R., and Campos, J. (2014). Intense foreshocks and a slow slip event preceded the 2014 Iquique Mw 8.1 earthquake. *Science*, *345*(6201), 1165–1169.

Rutter, E. H. (1976). The Kinetics of Rock Deformation by Pressure Solution. *Philosophical Transactions of the Royal Society of London. Series A: Mathematical and Physical Sciences*, *283*(1312), 203–219.

Rutter, E. H. (1983). Pressure solution in nature, theory and experiment. *Journal of the Geological Society*, *140*, 725–740.

Rybacki, E. and Dresen, G. (2004). Deformation mechanism maps for feldspar rocks. *Tectonophysics*, *382*(3-4), 173–187.

Saffer, D. M. and Tobin, H. J. (2011). Hydrogeology and Mechanics of Subduction Zone Forearcs: Fluid Flow and Pore Pressure. *Annual Review of Earth and Planetary Sciences*, *39*(1), 157–186.

Savage, J. C., Byerlee, J. D., and Lockner, D. A. (1996). Is internal friction friction? *Geophysical Research Letters*, *23*(5), 487–490.

Savin, S. M. and Epstein, S. (1970). The oxygen and hydrogen isotope geochemistry of clay minerals. *Geochimica et Cosmochimica Acta*, *34*(1), 43–63.

Schmid, E. (1928). Zn-normal stress law. In *Proc. Int. Congr. on Applied Mechanics*, Delft.

Schmid, E. and Boas, W. (1935). *Plasticity of crystals with special reference to metals*. London: F. A. Hughes & Co., Limited.

Schmid, S. M. and Casey, M. (1986). Complete fabric analysis of some commonly observed quartz C-axis patterns. In *Mineral and Rock Deformation*, 263–286. American Geophysical Union.

Scholz, C. H. (1998). Earthquakes and friction laws. *Nature*, *391*, 37–42.

Scholz, C. H. and Campos, J. (2012). The seismic coupling of subduction zones revisited. *Journal of Geophysical Research: Solid Earth*, *117*(B5).

Schwartz, S. Y. and Rokosky, J. M. (2007). Slow slip events and seismic tremor at circum-Pacific subduction zones. *Reviews of Geophysics*, *45*, 1–32.

Schwarz, S. and Stöckhert, B. (1996). Pressure solution in siliciclastic HP-LT metamorphic rocks - Constraints on the state of stress in deep levels of accretionary complexes. *Tectonophysics*, *255*, 203–209.

Scuderi, M. M., Tinti, E., Cocco, M., and Collettini, C. (2020). The Role of Shear Fabric in Controlling Breakdown Processes During Laboratory Slow-Slip Events. *Journal of Geophysical Research: Solid Earth*, *125*(11).

Seno, T. and Yamasaki, T. (2003). Low-frequency tremors, intraslab and interplate earthquakes in Southwest Japan-from a viewpoint of slab dehydration. *Geophysical Research Letters*, *30*(22), 1–4.

Shea, W. T. and Kronenberg, A. K. (1992). Rheology and deformation mechanisms of an isotropic mica schist. *Journal of Geophysical Research*, *97*(B11), 15201.

Shelly, D. R., Beroza, G. C., Ide, S., and Nakamula, S. (2006). Low-frequency earthquakes in Shikoku, Japan, and their relationship to episodic tremor and slip. *Nature*, *442*(7099), 188–191.

Shibazaki, B. and Iio, Y. (2003). On the physical mechanism of silent slip events along the deeper part of the seismogenic zone. *Geophysical Research Letters*, *30*(9), 1489.

Shillington, D. J., Bécel, A., Nedimović, M. R., Kuehn, H., Webb, S. C., Abers, G. A., Keranen, K. M., Li, J., Delescluse, M., and Mattei-Salicrup, G. A. (2015). Link between plate fabric, hydration and subduction zone seismicity in Alaska. *Nature Geoscience*, *8*(12), 961–964.

Shinevar, W. J., Behn, M. D., and Hirth, G. (2015). Compositional dependence of lower crustal viscosity. *Geophysical Research Letters*, *42*(20), 8333–8340.

Shreve, R. L. and Cloos, M. (1986). Dynamics of sediment subduction, melange formation, and prism accretion. *Journal of Geophysical Research*, *91*(B10), 10229.

Sibson, R. H. (1975). Generation of Pseudotachylyte by Ancient Seismic Faulting. *Geophysical Journal International*, *43*(3), 775–794.

Sibson, R. H. (1977). Fault rocks and fault mechanisms. *Journal of the Geological Society*, *133*(3), 191–213.

Sibson, R. H. (1980). Transient discontinuities in ductile shear zones. *Journal of Structural Geology*, *2*(1-2), 165–171.

Sibson, R. H. (1984). Roughness at the base of the seismogenic zone: Contributing factors. *Journal of Geophysical Research: Solid Earth*, *89*(B7), 5791–5799.

Sibson, R. H. (1996). Structural permeability of fluid-driven fault-fracture meshes. *Journal of Structural Geology*, *18*(8), 1031–1042.

Sibson, R. H. (1998). Brittle failure mode plots for compressional and extensional tectonic regimes. *Journal of Structural Geology*, *20*(5), 655–660.

Sibson, R. H. (2017). Tensile overpressure compartments on low-angle thrust faults. *Earth, Planets and Space*, *69*(1), 113.

Skarbek, R. M., Rempel, A. W., and Schmidt, D. A. (2012). Geologic heterogeneity can produce aseismic slip transients. *Geophysical Research Letters*, *39*(21), 1–5.

Sobolev, S. V. and Brown, M. (2019). Surface erosion events controlled the evolution of plate tectonics on Earth. *Nature*, *570*(7759), 52–57.

Stakes, D. S. and Taylor, H. P. (1992). The Northern Samail Ophiolite: An Oxygen isotope, microprobe, and field study. *Journal of Geophysical Research*, *97*(B5), 7043–7080.

Stenvall, C. A., Fagereng, Å., and Diener, J. F. A. (2019). Weaker Than Weakest: On the Strength of Shear Zones. *Geophysical Research Letters*, *46*(13), 7404–7413.

Stipp, M., Stünitz, H., Heilbronner, R., and Schmid, S. M. (2002). The eastern Tonale fault zone: a natural laboratory for crystal plastic deformation of quartz over a temperature range from 250 to 700 °C. *Journal of Structural Geology*, *24*(12), 1861–1884.

Strömgård, K. E. (1973). Stress distribution during formation of boudinage and pressure shadows. *Tectonophysics*, *16*, 215–248.

Suenaga, N., Yoshioka, S., and Matsumoto, T. (2016). Relationships among temperature, dehydration of the subducting Philippine Sea plate, and the occurrence of a megathrust earthquake, low-frequency earthquakes, and a slow slip event in the Tokai district, central Japan. *Physics of the Earth and Planetary Interiors*, *260*, 44–52.

Sun, T., Ellis, S., and Saffer, D. (2020). Coupled Evolution of Deformation, Pore Fluid Pressure, and Fluid Flow in Shallow Subduction Forearcs. *Journal of Geophysical Research: Solid Earth*, *125*(3), 1–26.

Syracuse, E. M., van Keken, P. E., and Abers, G. A. (2010). The global range of subduction zone thermal models. *Physics of the Earth and Planetary Interiors*, *183*, 73–90.

Taira, A., Okada, H., Whitaker, J. H., and Smith, A. J. (1982). The Shimanto Belt of Japan: Cretaceous-lower Miocene active-margin sedimentation. *Geological Society, London, Special Publications*, *10*(1), 5–26.

Tarling, M. S., Smith, S. A. F., and Scott, J. M. (2019). Fluid overpressure from chemical reactions in serpentinite within the source region of deep episodic tremor. *Nature Geoscience*, *12*(12), 1034–1042.

Tarling, M. S., Smith, S. A. F., Scott, J. M., Rooney, J. S., Viti, C., and Gordon, K. C. (2019). The internal structure and composition of a plate-boundary-scale serpentinite shear zone: the Livingstone Fault, New Zealand. *Solid Earth*, *10*(4), 1025–1047.

Tewksbury-Christle, C. M., Behr, W. M., and Helper, M. A. (2021). Tracking Deep Sediment Underplating in a Fossil Subduction Margin: Implications for Interface Rheology and Mass and Volatile Recycling. *Geochemistry, Geophysics, Geosystems*, *22*(3), 1–23.

Thomas, T. W., Vidale, J. E., Houston, H., Creager, K. C., Sweet, J. R., and Ghosh, A. (2013). Evidence for tidal triggering of high-amplitude rapid tremor reversals and tremor streaks in northern Cascadia. *Geophysical Research Letters*, *40*, 4254–4259.

Tichelaar, B. W. and Ruff, L. J. (1993). Depth of seismic coupling along subduction zones. *Journal of Geophysical Research: Solid Earth*, *98*(B2), 2017–2037.

Tulley, C. J., Fagereng, Å., and Ujiie, K. (2020). Hydrous oceanic crust hosts megathrust creep at low shear stresses. *Science Advances*, *6*(22), 1–9.

Twiss, R. J. (1977). Theory and applicability of a recrystallized grain size paleopiezometer. *Pure and Applied Geophysics*, *115*(1-2), 227–244.

Uchida, N., Iinuma, T., Nadeau, R. M., Burgmann, R., and Hino, R. (2016). Periodic slow slip triggers megathrust zone earthquakes in northeastern Japan. *Science*, *351*(6272), 488–492.

Uchida, N., Nakajima, J., Wang, K., Takagi, R., Yoshida, K., Nakayama, T., Hino, R., Okada, T., and Asano, Y. (2020). Stagnant forearc mantle wedge inferred from mapping of shear-wave anisotropy using S-net seafloor seismometers. *Nature Communications*, *11*(5676).

Ujiie, K., Noro, K., Shigematsu, N., Fagereng, Å., Nishiyama, N., Masuyama, H., Tulley, C. J., Mori, Y., and Kagi, H. (2021). Localized megathrust shear controlled by chemical reactions in subduction mélanges. *Submitted*.

Ujiie, K., Saishu, H., Fagereng, Å., Nishiyama, N., Otsubo, M., Masuyama, H., and Kagi, H. (2018). An Explanation of Episodic Tremor and Slow Slip Constrained by Crack-Seal Veins and Viscous Shear in Subduction Mélange. *Geophysical Research Letters*, *45*(11), 5371–5379.

Ulmer, P. and Trommsdorff, V. (1995). Serpentine Stability to Mantle Depths and Subduction-Related Magmatism. *Science*, *268*(5212), 858–861.

Van de Moortéle, B., Bezacier, L., Trullenque, G., and Reynard, B. (2010). Electron back-scattering diffraction (EBSD) measurements of antigorite lattice-preferred orientations (LPO). *Journal of Microscopy*, *239*(3), 245–248.

Van Diggelen, E. W. E., De Bresser, J. H. P., Peach, C. J., and Spiers, C. J. (2010). High shear strain behaviour of synthetic muscovite fault gouges under hydrothermal conditions. *Journal of Structural Geology*, *32*(11), 1685–1700.

van Keken, P. E. (2003). The structure and dynamics of the mantle wedge. *Earth and Planetary Science Letters*, *215*, 323–338.

von Mises, R. (1928). Mechanics of the ductile form changes of crystals. *Zeitschrift für Angewandte Mathematik und Mechanik*, *8*(3), 161–185.

Wada, I. and Wang, K. (2009). Common depth of slab-mantle decoupling: Reconciling diversity and uniformity of subduction zones. *Geochemistry, Geophysics, Geosystems*, *10*(10).

Wada, I., Wang, K., He, J., and Hyndman, R. D. (2008). Weakening of the subduction interface and its effects on surface heat flow, slab dehydration, and mantle wedge serpentinization. *Journal of Geophysical Research*, *113*(B4), 1–15.

Wallace, L. M. (2004). Subduction zone coupling and tectonic block rotations in the North Island, New Zealand. *Journal of Geophysical Research*, *109*(B12), B12406.

Wallace, L. M. (2020). Slow Slip Events in New Zealand. *Annual Review of Earth and Planetary Sciences*, *48*(1), 175–203.

Wallace, L. M. and Beavan, R. J. (2006). A large slow slip event on the central Hikurangi subduction interface beneath the Manawatu region, North Island, New Zealand. *Geophysical Research Letters*, *33*(11), 2006GL026009.

Wallace, L. M., Reyners, M., Cochran, U., Bannister, S., Barnes, P. M., Berryman, K., Downes, G., Eberhart-Phillips, D., Fagereng, Å., Ellis, S., Nicol, A., McCaffrey, R., Beavan, R. J., Henrys, S., Sutherland, R., Barker, D. H. N., Litchfield, N., Townend, J., Robinson, R., Bell, R., Wilson, K., and Power, W. (2009). Characterizing the seismogenic zone of a major plate boundary subduction thrust: Hikurangi Margin, New Zealand. *Geochemistry, Geophysics, Geosystems*, *10*(10), 1–32.

Wallace, L. M., Webb, S. C., Ito, Y., Mochizuki, K., Hino, R., Henrys, S., Schwartz, S. Y., and Sheehan, A. F. (2016). Slow slip near the trench at the Hikurangi subduction zone, New Zealand. *Science*, *352*(6286), 701–704.

Wallis, D., Lloyd, G. E., Phillips, R. J., Parsons, A. J., and Walshaw, R. D. (2015). Low effective fault strength due to frictional-viscous flow in phyllonites, Karakoram Fault Zone, NW India. *Journal of Structural Geology*, *77*, 45–61.

Wallis, S. R., Yamaoka, K., Mori, H., Ishiwatari, A., Miyazaki, K., and Ueda, H. (2020). The basement geology of Japan from A to Z. *Island Arc*, *29*(1).

Wang, K. and Bilek, S. L. (2011). Do subducting seamounts generate or stop large earthquakes? *Geology*, *39*(9), 819–822.

Warren-Smith, E., Fry, B., Wallace, L., Chon, E., Henrys, S., Sheehan, A., Mochizuki, K., Schwartz, S., Webb, S., and Lebedev, S. (2019). Episodic stress and fluid pressure cycling in subducting oceanic crust during slow slip. *Nature Geoscience*, *12*, 475–481.

Wassmann, S. and Stöckhert, B. (2013). Rheology of the plate interface - Dissolution precipitation creep in high pressure metamorphic rocks. *Tectonophysics*, *608*, 1–29.

Wassmann, S., Stöckhert, B., and Trepmann, C. A. (2011). Dissolution precipitation creep versus crystalline plasticity in high-pressure metamorphic serpentinites. *Geological Society, London, Special Publications*, *360*(1), 129–149.

Wech, A. G. and Creager, K. C. (2011). A continuum of stress, strength and slip in the Cascadia subduction zone. *Nature Geoscience*, *4*(9), 624–628.

Wenk, H.-R. and Christie, J. (1991). Comments on the interpretation of deformation textures in rocks. *Journal of Structural Geology*, *13*(10), 1091–1110.

Weyl, P. K. (1959). Pressure solution and the force of crystallization: a phenomenological theory. *Journal of Geophysical Research*, *64*(11), 2001–2025.

Wheeler, J. (1992). Importance of Pressure Solution and Coble Creep in the Deformation of Polymineralic Rocks. *Journal of Geophysical Research*, *97*(B4), 4579–4586.

Whittaker, J. M., Muller, R. D., Leitchenkov, G., Stagg, H., Sdrolias, M., Gaina, C., and Goncharov, A. (2007). Major Australian-Antarctic Plate Reorganization at Hawaiian-Emperor Bend Time. *Science*, *318*(5847), 83–86.

Wicks, F. J. and Whittaker, E. J. W. (1977). Serpentine textures and serpentinization. *Canadian Mineralogist*, *15*, 459–488.

Williams, A. J. (1979). Foliation development in serpentinites, Glenrock, New South Wales. *Tectonophysics*, *58*, 81–95.

Wilson, C. J. L., Evans, L., and Delle Piane, C. (2009). Modelling of porphyroclasts in simple shear and the role of stress variations at grain boundaries. *Journal of Structural Geology*, *31*(11), 1350–1364.

Wintsch, R. P. and Yeh, M.-W. (2013). Oscillating brittle and viscous behavior through the earthquake cycle in the Red River Shear Zone: Monitoring flips between reaction and textural softening and hardening. *Tectonophysics*, *587*, 46–62.

Zhao, P. and Ji, S. (1997). Refinements of shear-lag model and its applications. *Tectonophysics*, *279*, 37–53.

Zhu, W., Allison, K. L., Dunham, E. M., and Yang, Y. (2020). Fault valving and pore pressure evolution in simulations of earthquake sequences and aseismic slip. *Nature Communications*, *11*(1), 4833.

Appendix A

Python script for vein fluid volume calculations.

Qtz_solublity_calc

April 15, 2021

```
g the volume of H2O required to form a quartz vein from a
SiO2-bearing fluid assuming precipitation is triggered
 in fluid pressure.

equation of Manning (1994b) for the equilibroum solubility
n H2O, and the Holland and Powell (1991) equation of state
o calc water density.  HP-EOS adapted from Fagereng and Ellis 2009.

y as np
```

```
############### Constants ######################

10**-3 # gas constant (kJ / K / mol)
648    # density of quartz (kg/m3)

 for water density (Holland and Powell, 1991)

17
e-3
8e-5
91
2e-4
e-7

0e-2
e-5

650e-2
144e-6
7554e-3
221e-6


 for quartz solubility (Manning, 1994b)

;
6;
```

```
D = -2.2869e8;
E = 2.8454;
F = -1006.9;
G = 3.5689e5;
```

[3]:
```
# Calcuate at T = 330 and T = 500 celcius (approx peak temps from Raman
# spectra thermometry; Ujiie et al., 2018; Ujiie et al., 2021 (submitted).

T = 500 +273 # convert T to kelvin

g = 15 # thermal gradient, celcius per km (to calc P at T)

# Calcuate lithostatic and hydrostatic pressures at depth = T(oC) / g(oC/km)
# Assumes a water density of 1000 kg.m3 and rock density of 2650 kg.m3
P_lith  = round(((2650*9.81*(((T-273)/g)*1000))/1e8),2) # kbar
P_hydr  = round(((1000*9.81*(((T-273)/g)*1000))/1e8),2) # kbar

print('Lithostatic P =',P_lith,'kbar')
print('Hydrostatic P =',P_hydr,'kbar')
```

```
Lithostatic P = 8.67 kbar
Hydrostatic P = 3.27 kbar
```

[4]:
```
########## Calcuate the solubility of SiO2 in H2O #################

# Do the calcuation at each temperature, for P = P_lith and P = P_hydr
# Magnitude of P drop for coastal Makimine  = 3.53 Kbar

# input confining pressure (P)
P = P_lith-3.53


# Water density from Holland and Powell (1991)
if T < 695:
    P_sat = -13.627e-3 + 7.29395e-7*T**2 - 2.34622e-9*T**3 + 4.83607e-15*T**5
else:
    P_sat = 0

if T < 673:
    if P > P_sat:
        a = a0 + a1*(673-T) + a2*(673-T)**2 + a3*(673-T)**3
    else:
        a = a0 + a7*(673-T) + a8*(673-T)**2 + a9*(673-T)**3
else:
    a = a0 + a4*(T-673) + a5*(T-673)**2 + a6*(T-673)**3

b = b0
```

```
*T
*T


)
/np.sqrt(T)) + R*T*b + b**2*P)
* T**(-0.5));
 p_2, p_3, p_4]

ts(p)




P_sat:
vv[0] == 0:
 V_MRK = v[0]
e:
 if vv[1] == 0:
     V_MRK = v[1]
 else:
     if vv[2] == 0:
         V_MRK = v[2]

vv[2] == 0:
 V_MRK = v[2]
e:
 if vv[1] == 0:
     V_MRK = v[1]
 else:
     if vv[0] == 0:
         V_MRK = v[0]

] == 0:
RK = v[2]

vv[1] == 0:
 V_MRK = v[1]
e:
 if vv[0] == 0:
     V_MRK = v[0]


 V_MRK + c*np.sqrt(P-P0) + d*(P-P0)

 V_MRK # molar volume kJ/Kbar
```

```
# kJ/kbar to cm3
v_h2o = 10*v_h2o

# molar mass / molar volume = density (g.cm3)
rho_h2o = 18.01528/v_h2o

# Solubility (molarity) of SiO2 in H2O from Manning (1994b)
log_m_qtz = A + B/T + C/(T**2) + D/(T**3) + (E+F/T + G/(T**2)) * np.log(rho_h2o)
m_qtz = 10**log_m_qtz

# convert molarity to grams of Sio2 per liter of h2O
# (g SiO2/mol SiO2 * mol SiO2/LH2o = g SiO2/l H2O)
g_pL = 60.08*m_qtz

# convert to grams of Sio2 per m3 of water (ppm)
g_pcm = round(g_pL*1000)

print('SiO2 concentration in H2O = ',"%.0f"%g_pcm,'ppm')
```

```
SiO2 concentration in H2O =  6028 ppm
```

[5]:
```
# The volume of fluid needed to form a quartz vein depends on the ammount of␣
 ↪SiO2 that
# is unstable in the fluid (ignoring reaction kinetics). In this model, the␣
 ↪ammount of
# unstable SiO2 depends on the magnitude of the pressure-drop. The maximim ␣
 ↪pressure
# drop will give the minimum volume of fluid required to fill the vein. Smaller␣
 ↪drops
# in pressure would result in fluids with lesser ammounts of SiO2 able to␣
 ↪precipitate,
# requiring larger fluid volumes to form the vein.

# The maximum ammount of supersaturation is therefore  calcuated as the␣
 ↪equilibrium
# solubility at lithostatic pressure minus the equilibrium solubility at
# hydrostatic pressure:

# Calcuation results; ppm SiO2 in H2O at the vein-forming temperature at the␣
 ↪expected
# lithostatic and hydrostatic fluid pressures:

# Coastal Makimine 1878 - 888 ppm
# NMR: 10487 - 3538 ppm
# NMR, p drop same magnitude as makimine: 10487 - 6028 ppm

# round SiO2 supersaturation to nearest multiple of 500.
```

```
487 - 6028
und(ppm_ss/500)
m_ss*500

 of supersaturated SiO2 per m3 of H2O (equivalent to g/m3)
_ss # g/m3
d would contain ~',g_pcm,'ppm of supersaturated SiO2')
g_pcm/10000),'% SiO2)')

/m3 to kg/m3
pcm/1000  # kg/m3
valent to',kg_pcm,' kg of supersaturated SiO2 / m3 H2O')
```

```
contain ~ 4500 ppm of supersaturated SiO2
2)
o 4.5  kg of supersaturated SiO2 / m3 H2O
```

```
SiO2 is required to fill a typical sized vein?

 typical vein (calc as an elipse x long, y wide, z thick)
m
m
m
p.pi*x*y*z # m3
,3) # m3
 would contain',V,'m3 of quartz')

iO2 required to fill vein (kg) = kg/m3 * m3
o_qtz*V
und(m_sio2)
n would weigh',m_sio2,'kg')
```

```
ontain 0.126 m3 of quartz
weigh 334 kg
```

```
 h2o required (m3h2o) =  kgSiO2 / kgSiO2/m3h2o
sio2/kg_pcm)
uired volume to nearest 10 m3
nd(v_h2o/10)
2o*10
 requires at least',v_h2o,'m3 of H2O')
```

```
s at least 70 m3 of H2O
```

```


akimine (T=328): 330 m3 H2O
```

```
# NMR (T=500): 50 m3 H2O
# NMR (T=500), assuming same magnitude P drop as coastal Makimine : 70 m3 H2O
```